Interactions of Transition Metals with Silicon (100): The Ni-Si, Co-Si and Au/Si(100) Systems

by

Steven Naftel

Graduate Program

in

Chemistry

Submitted in partial fulfilment

of the requirements for the degree of

Doctor of Philosophy

Faculty of Graduate Studies

The University of Western Ontario

London, Ontario

July, 1999

© Steven J. Naftel 1999

The author has granted a non-exclusive licence allowing the National Library of Canada to reproduce, loan, distribute or sell copies of this thesis in microform, paper or electronic formats.

The author retains ownership of the copyright in this thesis. Neither the thesis nor substantial extracts from it may be printed or otherwise reproduced without the author's permission.

L'auteur a accordé une licence non exclusive permettant à la Bibliothèque nationale du Canada de reproduire, prêter, distribuer ou vendre des copies de cette thèse sous la forme de microfiche/film, de reproduction sur papier ou sur format électronique.

L'auteur conserve la propriété du droit d'auteur qui protège cette thèse. Ni la thèse ni des extraits substantiels de celle-ci ne doivent être imprimés ou autrement reproduits sans son autorisation.

0-612-42546-0

Canadä

ABSTRACT

This thesis encompasses studies of the electronic and physical structure of three transition metal interfaces with Si(100) substrates.

The first case concerns a high resolution photoemission (PES) study of the initial stages (0 to ~25 ML) of the formation of the Au/Si(100) interface at room temperature. The interface was studied using Si 2p and Au 4f core-level PES, using synchrotron radiation. It was found that the Au and Si react immediately upon deposition to form a Au-Si phase. This initial Au-Si phase is seen to change to a second Au-Si phase by 3.6 ML (1 ML = 6.78×10^{14} atoms/cm^2) of Au coverage. As the coverage is increased a layer of the second Au-Si phase remains on the surface while pure Au layers form underneath it.

Second we report a Si $L_{3,2}$-, Si K-, Co $L_{3,2}$- and Co K-edge X-ray absorption near-edge structures (XANES) study of a series of cobalt and cobalt silicide thin films prepared by thermally annealing deposited Co layers on Si(100) substrates. By collecting both Total Electron Yield (TEY) and Fluorescence Yield (FLY) XANES at the above edges we monitored the electronic and physical structural differences between films annealed under different conditions. It was found that the as deposited Co film exhibits noticeable intermixing at the Co-Si interface. The annealed films consisted of CoSi$_2$; however, both SiO$_2$ and metallic Co were found in the near surface region of these films. The origin of the metallic Co remains undetermined.

Thirdly, we report a Si $L_{3,2}$-, Si K-, Ni $L_{3,2}$- and Ni K-edge, TEY and FLY XANES study of a series of nickel and nickel silicide thin films prepared by thermally annealing deposited Ni layers on Si(100) substrates. The unannealed films again showed noticeable intermixing at the Ni-Si interface. The annealed Ni films produced primarily NiSi and NiSi$_2$ films depending on the final annealing temperature. Using the XANES spectra from the Ni-Si blanket films as a reference we determined that Ni-Si sub-micron lines formed on Si(100) were predominantly NiSi; however, the conversion of the Ni/Si system to a pure NiSi phase appeared to be affected by the line thickness, with the conversion becoming less complete as the lines become narrower.

Keywords: X-ray Absorption Near-Edge Structure, XANES, Photoemission Spectroscopy, PES, Silicide Thin Films, Electronic Structure, Physical Structure, Au/Si(100), Nickel Silicide, Cobalt Silicide, Total Electron Yield, Fluorescence Yield.

iii

CO-AUTHORSHIP

The following thesis contains material based on previously published manuscripts co-authored by Steven Naftel, T. K. Sham, Ian Coulthard, YongFeng Hu, Martin Zinke-Allmang, D.-X. Xu, Suhit Das and L. Erickson. The experimental work and WIEN calculations presented in this thesis were preformed by Steven Naftel, except as follows:

Some of the photoemission data on clean silicon (100) and the fitting of the clean silicon spectra presented in the introduction of Chapter 3 were preformed by Dr. Detong Jiang and were part of unpublished work done in collaboration with Dr. Peter Norton.

M. Zinke-Allmang provided one of the cobalt thin film samples examined in Chapter 4. Jim Garret from the Materials Preparation Group at McMaster University provided the bulk $CoSi_2$ sample analysed in Chapter 4. The remaining cobalt silicide samples were provided by M. Saran of Northern Telecom. Some of the Si K-edge data of Chapter 4 was taken by YongFeng Hu, while, some of the Co K-edge data were taken by Ian Coulthard and T. K. Sham

Dr. Suhit Das, D.-X. Xu and L Erickson provided the nickel silicide thin film and line samples analysed in Chapter 5. Some of the Ni K-edge data in Chapter 5 were taken by Ian Coulthard and T. K. Sham.

For copyright releases see the Appendix.

iv

To Connie

v

ACKNOWLEDGEMENTS

First I would like to thank my supervisors Professor T. K. Sham and Professor P. R. Norton without whose patience, encouragement and direction this work would not have been possible. Their optimism and vision have halped me through some difficult times. My gratitude for the commitment of their time and resources to this project can not be overstated.

I want to acknowledge the people that helped me with some of the technical and experimental aspects of this work: Dr. Detong Jiang, Dr. Ian Coulthard, Dr. Kim Tan, Dr. YongFeng Hu, Dr. D.-X. Xu, Dr. S. R. Das, Dr. J. Garret, Dr. Keith Griffiths, Dr. John Tse, Dr. Dennis Krug, Dr. Martin Zinke-Allmang and M. Saran.

I would also like to thank my lab mates: Dr. Mark Kuhn, Dr. Arthur Bzowski, Dr. Jian-Zhang Xiong, Dr. Ramaswami Sammynaiken. Thanks also to my friends who made student life bearable: Len Luyt, Jonathan Rochleau, Greg Canning, Marina Suominen-Fuller, Mike Scaini, Glenn Munro, Joy Munro, Claire Brown, Al Brown, Christine Brown, Nicki Curtis, Robin Martin, Alison Paprica and Paul Wiseman.

Special thanks to my parents and brother for their patience, support and understanding in dealing with the eternal student.

A very special thanks to Connie whose entrance into my life has encouraged and inspired me to do my best.

vi

TABLE OF CONTENTS

ix

LIST OF TABLES

x

LIST OF FIGURES

xii

CHAPTER 1: INTRODUCTION

Metal silicides were studied for many years before the advent of silicon based solid state electronics. The growing dependence of our society on silicon based electronic devices has made the properties of silicon compounds of prominent importance to our present and future.

Metal silicides first attracted attention at the turn of the century after the development of the electric furnace by H. Moissan [1]. The development of the furnace allowed various silicides to be systematically prepared at about this time. The early studies of silicides generally focused on understanding the physical properties of silicides in terms of their electronic and crystal structures. Other studies were stimulated by the high temperature stability of many refractory silicides [2]. In the 1960's, M. P. Lepselter [3] at Bell Laboratories pioneered the use of silicides as Schottky barriers. Silicide studies since have focused on the use of metal silicides in integrated circuit technology. See [2][4][5][6][7][8][9] for reviews. Such a focused effort has produced large volumes of information on the thermodynamic, kinetic, physical, and electrical properties of most of the silicides. Although the majority of studies have been centered on the device characteristics and usefulness of metal silicides, silicides have also been studied as model systems for binary alloy formation in thin films [10] and interfacial reactions [11].

Perhaps no other industry drives itself to improve its products as fast as the semiconductor industry. Since Gordon Moore's famous talk at the International Electron Devices Meeting (IEDM) in 1975, the industry has met or bettered his predicted growth rate in chip complexity (and decreased minimum feature size)[12]. Moore predicted a growth in chip complexity by a factor of two every year, now called Moore's law. In

order to better define the trends in increasing complexity and identify the technological advances necessary to continue the trends, the Semiconductor Industry Association introduced the National Technology Roadmap for Semiconductors [13] in 1992 (with revised editions in 1995 and 1997). The roadmap has succeeded in driving innovations in the industry even faster, as companies compete to be the first to meet the projected guidelines for new architectures. As a result, more recent studies [14][15][16][17] of metal silicides have focused on meeting the challenges posed by the ever decreasing dimensions and complexity of ultra large scale integration (ULSI).

More than half the elements in the periodic table form compounds with silicon (see Figure 1.1). The transition metals form a large number of silicides of various compositions, with most metals forming more than three stable compounds. However, not all of the compounds seen in the bulk phase diagrams form in the thin film regime. The technically useful silicides fall into three main groups: the metal rich silicides M_xSi, the monosilicides MSi, and the disilicides MSi_2. The most important of these have been the disilicides.

Silicides have found applications in integrated circuit technology as: interconnects, ohmic contacts to source, drain and gate in CMOS (Complementary Metal Oxide Semiconductor) devices, see Figure 1.2, Schottky barrier devices, and more recently, as diffusion barriers along Al metal interconnects. In order to be useful in these applications a compound must, in general: have good conductivity, be compatible with current manufacturing techniques and be reliable [2][15][18]. These three conditions can entail: low resistivity, high temperature stability, ease of formation, ability and ease of patterning, minimal junction penetration, no reaction with other metals or silicon oxide layers, good adhesion to other layers and resistance to electromigration [2][18]. Certainly no silicide can meet all these conditions.

The wide variety of compounds, complex phase transitions and the need to satisfy such a large set of conditions to obtain good device performance, has driven the fundamental investigations into metal silicides. This has generated a large body of knowledge about the properties of metal silicides. Research has especially focused on

1	2	3	4	5	6	7	8	9	10	11	12	13	14	15	16	17	18
H																	
Li												B	C	N	O	F	
Na	Mg												Si	P		Cl	
K	Ca	Sc	Ti	V	Cr	Mn	Fe	Co	Ni	Cu				As	Se	Br	
Rb	Sr	Y	Zr	Nb	Mo		Ru	Rh	Pd						Te	I	
Cs	Ba	La **	Hf	Ta	W	Re	Os	Ir	Pt								

Ce	Pr	Nd		Sm	Eu	Gd	Tb	Dy	Ho	Er	Tm	Yb	Lu
Th		U	Np	Pu									

Figure 1.1. Periodic table showing elements that form compounds with silicon.
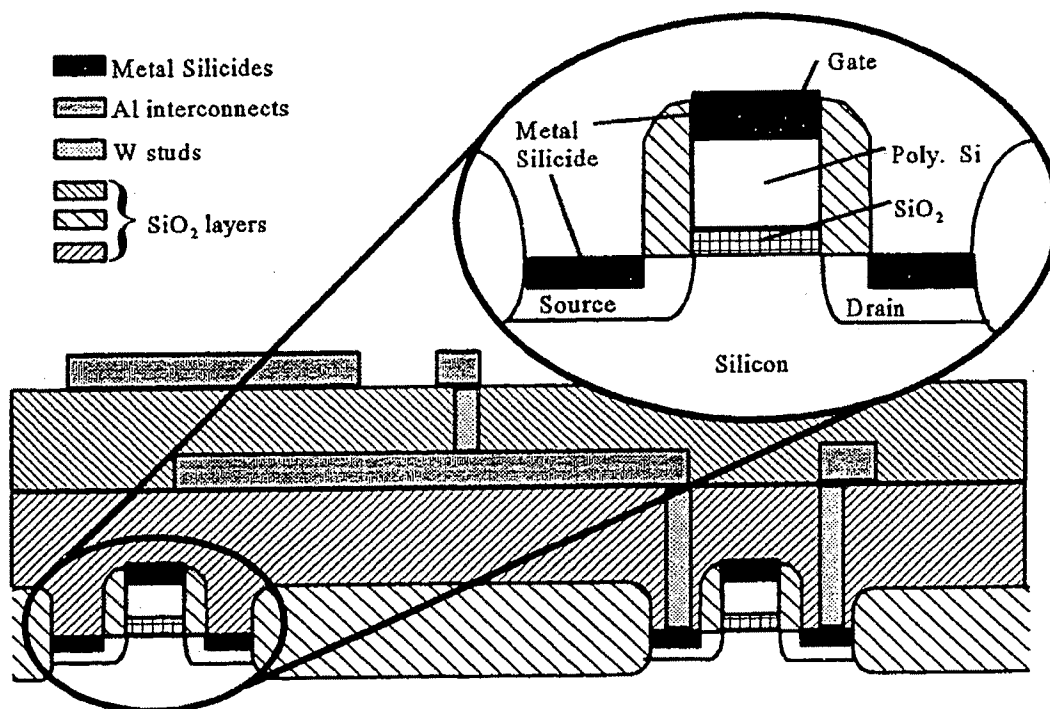
Figure 1.2. Schematic diagram of a CMOS logic device showing the use of silicides.

those metals which were found to have good compatibility with the conditions of integrated circuit (IC) manufacture, namely Pt, Pd, W, Mo, Ti, Co, Ni and Ta [18].

In general, a CMOS device, such as the one schematically represented above, has between 3 and 5 interconnect layers above the transistors. Currently such devices are produced with a minimum feature size (approximately the width of the gate) of 0.25 μm. In 0.25 μm technology the source and drain are about 60 nm deep and the gate oxide is about 4-5 nm thick [19]. The semiconductor industry plans to reach a minimum feature size of 0.18 μm by the end of 1999 and a minimum feature size of 0.07 μm by the year 2009[19].

Research on the metal silicides used in industrial processes has mainly focused on the overall device performance. However, as the minimum feature size of solid state transistors moves toward 0.1 μm, problems associated with the properties of the interconnects and contacts, such as parasitic resistance and capacitance [5][18], as well as problems associated with the control of reactions in thin films, such as junction penetration

[5][9][20], have become the most prominent challenges facing the semiconductor industry.

In order to meet the new challenges posed by decreasing device size, research has focused on new materials, device architectures and fabrication technologies. However promising these new materials and approaches may be, they sidestep the main problem. As the device size shrinks, the electrical properties of devices are beginning to be dominated by the properties of the interfaces. Therefore, the understanding and characterization of metal silicon (or any other new material) interfacial interactions at small dimensions is of vital importance to device performance. For example, the gate oxide thickness in 0.07 μm technology will only be about 1.5 nm.

One can approach the challenge of interfacial interactions from two directions:

1) In the surface science regime, a careful study of the changes in electronic structure that occur as the interface forms layer by layer under a specific set of conditions.

2) In the thin film regime, a study of the electronic and structural properties present in thin films (50 - 100 Å) formed under varying conditions.

Metal silicides are prepared by depositing a layer of pure metal onto a poly- or
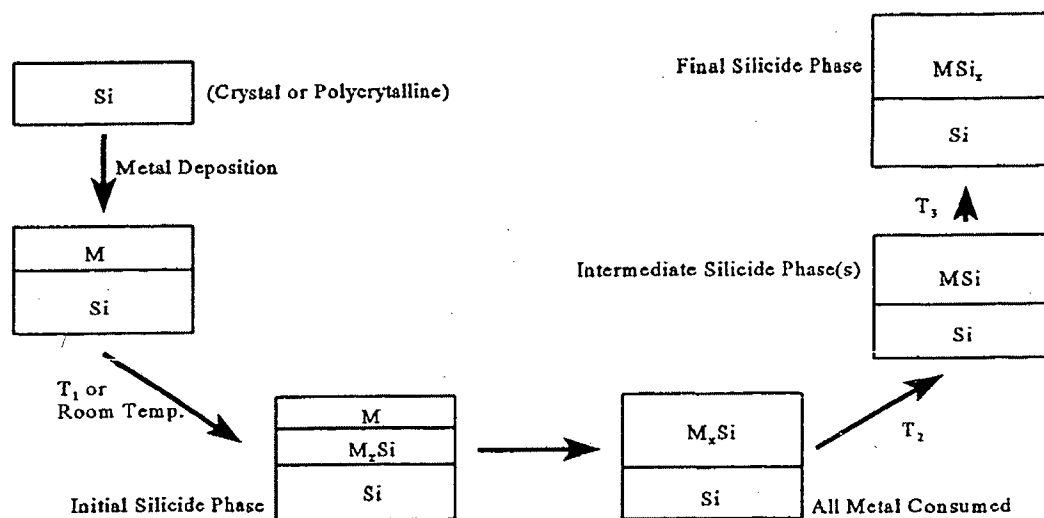
Figure 1.3. Schematic diagram illustrating heat induced synthesis of thin film transition metal silicides.

single crystal silicon surface, followed by annealing at an appropriate temperature to cause formation of the desired silicide. This process is schematically illustrated in Figure 1.3.

The metal can be deposited by any type of source, metal and silicon can be co-deposited on the surface [9][17], or metal atoms can even be buried under the surface using ion beam techniques [14]. However the metal is deposited, the deposition is followed by annealing, which can be done in a conventional furnace or by rapid thermal annealing techniques. All these variations can affect the order and prevalence of phases formed as well as the overall temperatures required.

Generally the first phase to nucleate at the interface is a metal rich silicide, M_xSi. After all the metal has been used up, the monosilicide MSi forms, followed by the most silicon rich silicide possible, usually the disilicide, MSi_2. Depending on the preparation conditions these phases can form sequentially or coexist [17]. Metal silicide formation has been found to be diffusion controlled. The main diffuser is the metal atom in the initial stages of the interaction, formation of M_xSi. After the initial compound has formed, the further reaction is controlled by Si atom diffusion [17]. The initial interaction between the transition metal and silicon to form a metal rich phase often occurs at temperatures below ~200 °C.

This thesis reports the investigation of metal silicon interactions in both the interfacial and thin film regime. We used synchrotron radiation based photoemission and X-ray absorption techniques (Chapter 2) to study the electronic and physical structures in three transition metal-silicon systems. The systems of interest were:

1) The initial stages (sub-monolayer) of the formation of the Au on Si(100) interface, studied by Photoemission Spectroscopy (PES). (Chapter 3)

2) The evolution of the structure and electronic properties of Cobalt silicides in Co thin films on Si(100), studied by X-ray Absorption Near-Edge Structure (XANES) spectroscopy. (Chapter 4)

3) The evolution of the structure and electronic properties of Nickel silicides in Ni thin films and patterned lines on Si(100), studied by (XANES). (Chapter 5)

Summary and conclusions are presented in Chapter 6.

1.1   REFERENCES

[1]   H. Moissan, *The Electric Furnace*, English translation by A. de Mouilpied (Edward Arnold, London, 1904).

[2]   S. P. Murarka, *Silicides for VLSI Applications* (Academic Press, New York, 1983).

[3]   M. P. Lepselter and J. M. Andrews, in *Ohmic Contacts to Semiconductors*, ed. B. Schwartz (Electrochemical Society, Princeton, 1969), p. 159.

[4]   K. N. Tu and J. W. Mayer, in *Thin Films: Interdiffusion and Reactions*, eds. J. M. Poate, K. N. Tu and J. W. Mayer (Wiley-Interscience, New York, 1978), p. 360.

[5]   S. P. Murarka and M. C. Peckerar, *Electronic Materials: Science and Technology* (Academic Press, Boston, 1989), Ch. 6.

[6]   See for example, Appl. Surf. Sci. **53**, (1991); the entire volume deals with metal silicides and their applications in microelectronics.

[7]   E. G. Colgan, J. P. Gambino and Q. Z. Hong, Mater. Sci. Eng. **R16**, 43 (1996).

[8]   R. T. Tung, Appl. Surf. Sci. **117/118**, 268 (1997).

[9]   J. P. Gambino and E. G. Colgan, Mater. Chem. and Phys. **52**, 99 (1998).

[10]   G. Ottaviani, J. Vac. Sci. Tech. **16**, 1112 (1979).

[11]   A. Cros and P. Muret, Mater. Sci. Rep. **8**, 271 (1992).

[12]   P. Singer, Semiconductor International, Jan., 46 (1995).

[13]   *The National Technology Roadmap for Semiconductors* (Semiconductor Industry Association, San Jose, 1994).

[14]   S. Mantl, Mater. Sci. Rep. **8**, 1 (1992).

[15]   K. Maex, Mater. Sci. Eng. **R11**, 53 (1993).

[16]   J. Chen, J.-P. Colinge, D. Flandre, R. Gillon, J. P. Raskin and D. Vanhoenacker, J. Electrochem. Soc. **144**, 2437 (1997).

[17]   V. E. Burisenko and P. J. Hesketh, *Rapid Thermal Processing of Semiconductors* (Plenum Press, New York, 1997), Ch. 5.

[18]   K. Maex and M. Van Rossum, eds., *Properties of Metal Silicides* (Inspec,

London, 1995).

[19]   L. Peters, Semiconductor International, Jan., 61 (1998).

[20]   C. M. Osburn, Q. F. Wang, M. Kellam, C. Canovai, P. L. Smith, G. E. McGuire,
Z. G. Xiao and G. A. Rozgonyi, Appl. Surf. Sci. **53**, 291 (1991).

CHAPTER 2: THEORY AND EXPERIMENTAL TECHNIQUES

2.1   INTRODUCTION

A central tenet of modern science is that the electronic structure of matter, the energy levels and physical space occupied by electrons in a material, determines the physical and chemical properties of the material. An important tool that can be used to study the electronic structure of matter is electromagnetic (EM) radiation. EM radiation covers an immense range of energies and wavelengths from radio waves ($\lambda=1$ m, $E=10^{-6}$ eV) to γ-rays ($\lambda=10^{-11}$ m, $E=10^5$ eV). Of special significance is the part of the spectrum from infrared to hard-X-rays. This region covers EM radiation with wavelengths that range from the size of a protein molecule to the length of chemical bonds. The energy in this region ranges from that necessary to cause bond vibration to that necessary to eject valence and core electrons ([1], Figure 2.1). Thus EM radiation in the appropriate energy range (soft to hard X-rays), corresponding to electron binding energies, can be used to obtain information about the electronic structure of materials by investigating the interaction of the photons with the material.

The absorption of EM radiation in the ultraviolet and X-ray range of energies usually results in the ejection of a photoelectron. Thus, there is a correlation between the study of X-ray absorption and the study of photoelectrons.
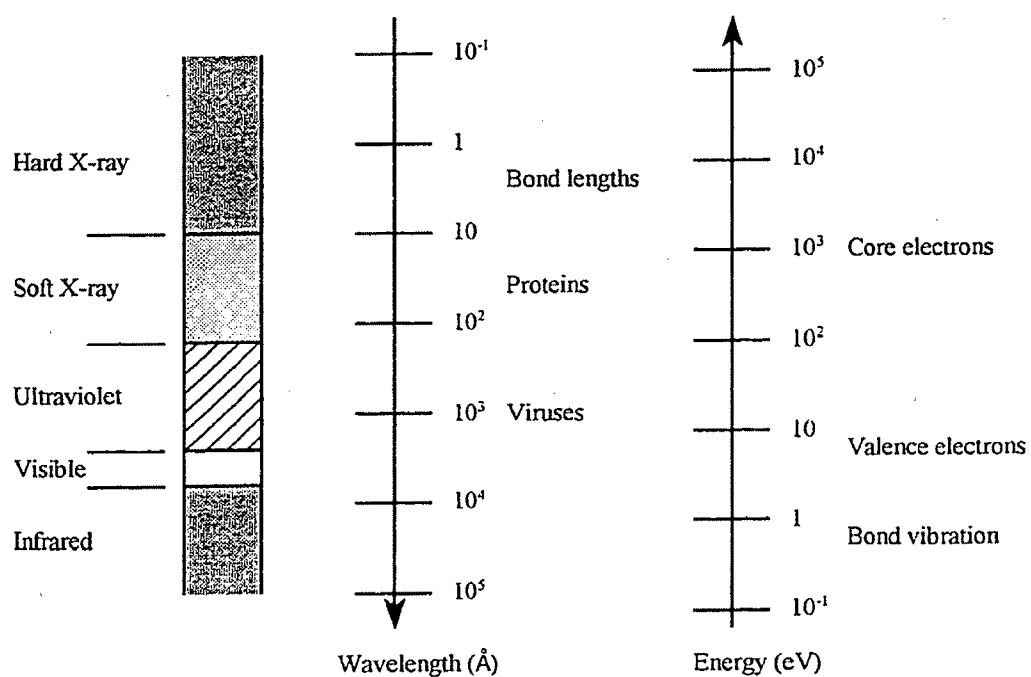
Figure 2.1. Part of the electromagnetic spectrum covered by synchrotron radiation and a few of the research interests in this range. (After G. Margaritondo [1])
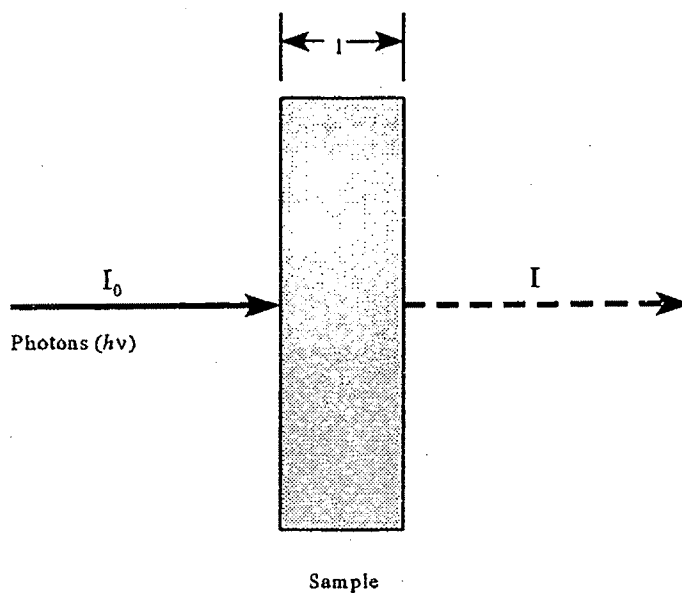
Figure 2.2. Schematic diagram of the X-ray absorption process in transmission mode.

2.2 X-RAY ABSORPTION

2.2.1 X-ray Absorption

X-ray absorption measures the variation in the absorption coefficient (μ) as a function of the photon energy ($h\nu$). This is accomplished by monitoring the intensity of the incident radiation (I_0) and the transmitted radiation (I) that has passed through the sample after interacting with it, schematically shown in Figure 2.2. Due to the absorption, the beam intensity decreases according to the exponential law:

$$I = I_0 \exp(-\mu l) \tag{2.1}$$

where μ is the absorption coefficient and l is the path length through the sample (sample thickness).

The absorption coefficient is a function of the photon energy. When light of sufficient energy, ultraviolet or X-rays, is incident on a sample the photon can be absorbed by promoting an electron from an occupied state to an unoccupied state above the Fermi level, or to the continuum. This process is schematically shown in Figure 2.3. To be ejected to the continuum the electron must have sufficient energy to overcome the difference between the Fermi level and the vacuum level. The difference between the Fermi and vacuum levels is called the work function (ϕ) and represents the work required to remove an electron from the surface of the solid.

Radiation with energies below that required to excite a particular core electron can not be absorbed by that core electron. Photons, with energies below a particular core level, are however absorbed by shallower core levels or valence states, giving rise to a background absorption signal. As the photon energy reaches that required to excite a core electron, absorption by that level becomes possible and a large jump in the absorption coefficient, above the background, occurs which is seen as a sharp edge in the spectrum, Figure 2.4. The energy at which this edge occurs is called the threshold energy and
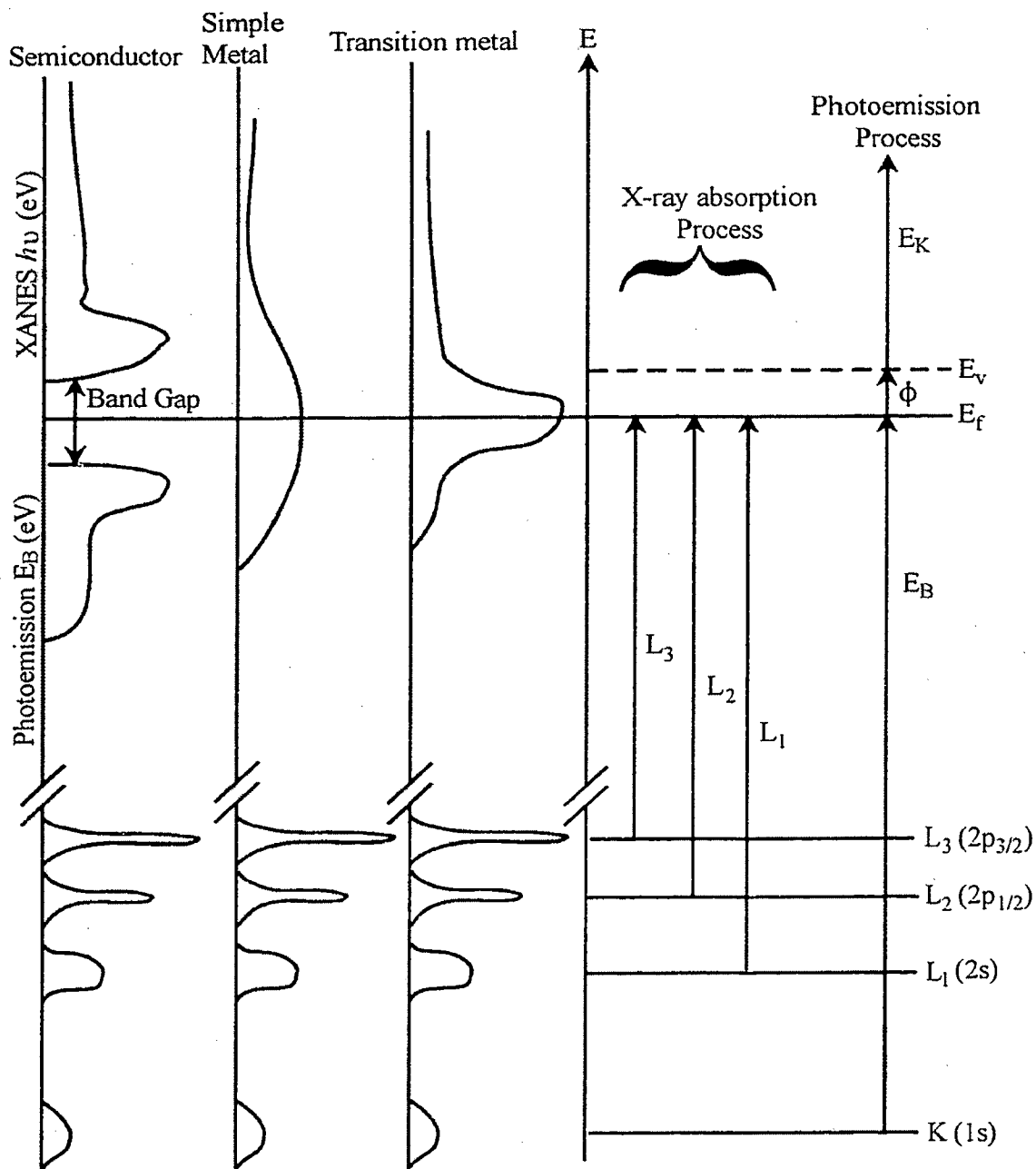
Figure 2.3. Diagram illustrating X-ray absorption and photoemission spectra in metals. E_f and E_v are the Fermi and vacuum levels respectively. The left side of the figure represents the densities of states for a semiconductor, simple metal and transition metal. (After T. K. Sham [2])
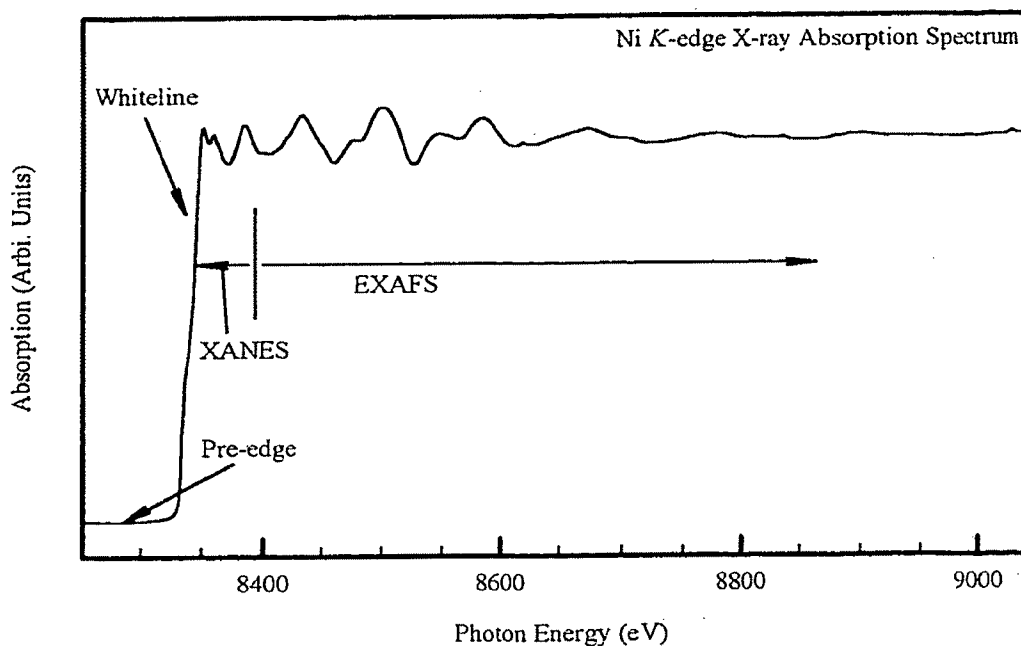
Figure 2.4. Ni K-edge X-ray absorption spectrum taken in total electron yield mode showing the pre-edge, whiteline, XANES and EXAFS regions.

corresponds to the binding energy of the core hole. Historically, the edge is also known as the whiteline, since it was first observed using photographic plates which when developed depicted the intense edge resonance as a white line on the plate.

When the excited electron originates from the $n = 1$ shell the corresponding absorption edge is called the K-edge. Electrons originating from the $n = 2$ shell give rise to the L-edges. If the excited electron is a $2s$ electron you have the L_1-edge. The L_2- and L_3-edges correspond to excited electrons from the $2p_{1/2}$ and $2p_{3/2}$ levels, respectively.

For molecules in the gas phase the energy levels (orbitals) are generally discrete. In a solid the number of occupied and unoccupied valence orbitals increases, causing the discrete levels to coalesce into bands of allowed states. The valence band, below the Fermi level, is filled while the conduction band is unoccupied above the Fermi level. The deep energy levels close to the nucleus are largely unaffected in the solid and maintain their discrete nature. As a result of the formation of bands, the absorption spectrum of a solid sample has much broader features which match the density of unoccupied states above the Fermi level. Figure 2.3 depicts the density of states for a metallic system. For a

transition metal the d-band crosses the Fermi level and in semiconductors the top of the valence band and the bottom of the conduction band are separated by the band-gap. In a metallic system, the Fermi level corresponds to the uppermost filled level (analogous to the highest occupied molecular orbital (HOMO) in molecules). For intrinsic semiconductors (no doping), the Fermi level corresponds to the mid-point of the band gap. In doped semiconductors, the Fermi level is closer to the top of the valence band or the bottom of the conduction band depending on the degree and type of doping.

A general quantum mechanical description for the process of absorption is based on Fermi's golden rule [3][4]:

$$W = \frac{2\pi}{\hbar} \; |\langle f|H'|i\rangle|^2 \; \rho(E_f) \tag{2.2}$$

where W is the transition probability per unit time for the system under perturbation H' from initial state $|i\rangle$ to final state $|f\rangle$, $\langle f|H'|i\rangle$ is the transition matrix element, and $\rho(E_f)$ is the density of final states. Here the perturbation is simply the incident photon which can be described as:

$$H' = A_0 \; \exp(i k \cdot r) \tag{2.3}$$

where A_0 is a constant.

As in most transitions, for certain combinations of initial and final state symmetries the transition matrix element becomes zero and the transition is forbidden. In the dipole approximation the transition is restricted by the selection rules, $\Delta l = \pm 1$ and $\Delta j = 0, \pm 1$. l is the orbital angular momentum quantum number and j is the total angular momentum quantum number, $j = l \pm \frac{1}{2}$.

A general absorption spectrum is shown in Figure 2.4, it consists of two regions:

1) The XANES (X-ray Absorption Near-Edge Structure), and,

2) The EXAFS (Extended X-ray Absorption Fine Structure), where the outgoing

photoelectron scatters off neighbouring atoms giving rise to sinusoidal oscillations in the absorption coefficient [5].

As described above, the absorption is measured by comparing the intensities of the incident and transmitted light. Therefore, in order to measure the absorption spectrum, enough radiation must pass through the sample to be detected. For solid samples this requires the use of powdered or very thin unsupported samples which are not suitable for the study of thin films.

After absorbing the photon, an atom in the material is left with a core hole. The presence of a core hole creates an excited state from which the atom must decay. The atom relaxes to a low energy state by having an electron from a higher level fill the core hole; see Figure 2.5. The excess energy of this electron may be removed from the system by ejecting another electron (Auger process) or by emitting a photon (fluorescence process). The Auger and fluorescence relaxation processes are competitive; heavy elements ($Z > 30$) are more likely to decay by fluorescence whereas light elements are more likely to eject an Auger electron.

Since each absorption event creates a core hole, the probability of exciting an electron from a particular core level at a given photon energy, the absorption coefficient, is equal to the probability of creating a core hole in this level. Since both Auger decay and fluorescence emission decay are proportional to the annihilation of the core hole, they are both proportional to the absorption coefficient [6]. The X-ray absorption can thus be conveniently monitored by the by-products of the absorption process, core hole relaxation, rather than by the amount of transmitted light. One can thus use, Auger electron, partial electron, total electron, fluorescence, or luminescence yields to replace the transmitted light intensity for solid state and thin film studies. This thesis makes use of Total Electron Yield (TEY) and Fluorescence Yield (FLY) techniques, which are illustrated in Figure 2.6.

2.2.2 Sampling depth of XAS

The sampling depth is an important factor in techniques used for the study

Auger Process   Fluorescence Process
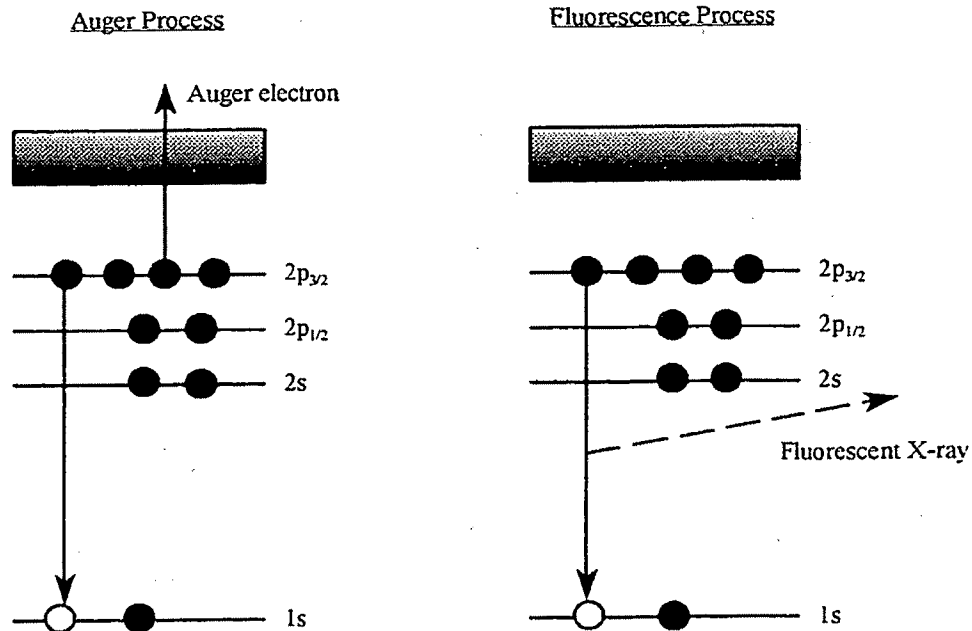
Figure 2.5. Mechanisms for the decay of a core-hole after the absorption of an X-ray photon.
(After S. M. Heald in Ref. [5])

Total Electron Yield (TEY)   Fluorescence Yield (FLY)
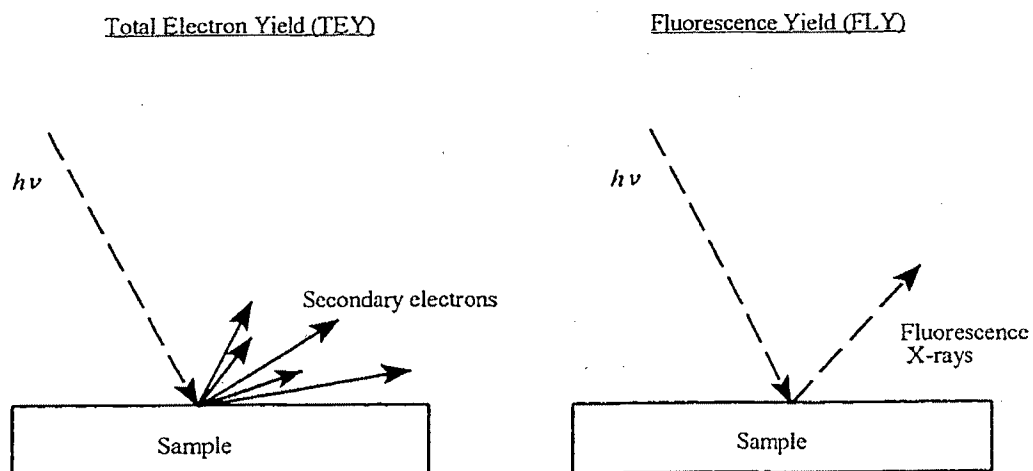
Figure 2.6. Schmatic diagram of the geometry of Total Electron Yield and Fluorescent Yield
X-ray absorption detection modes.

of surfaces and interfaces. The sampling depth of X-ray absorption from solids varies with the particular edge studied and the chosen detection method. The sampling depth of any technique can be limited by the depth of sample illuminated (penetration depth) by the incident beam and by the depth from which measured signal can reach the detector (escape depth) without loss of information. For both X-ray absorption and photoemission spectroscopies the sampling depth is limited by the escape depth of the absorption byproducts.

One simple way to gauge the relative sampling depths of different X-ray absorption edges is to look at the photon penetration depth. The photon penetration depth is often gauged with the one absorption length, which is defined as the thickness at which the photon intensity has decreased to $1/e$ of its original value. The penetration depth is given by the inverse of the linear X-ray absorption coefficient (μ, in units of cm^{-1}). Based on values of μ tabulated, in the low energy range (<1000 eV) by B. L. Henke *et al.* [7] and at higher energies by W. H. McMaster *et al.* [8], we have estimated the absorption length of photons at energies above the edges used in the thesis (Table 2.1). These values, calculated for the pure material (for example, the absorption length at the Ni L-edge is calculated for pure Ni), do not directly apply to the materials used but they do serve as a general guide. It is apparent that the Si L-edge should be extremely useful as a tool to study the near surface region of thin silicide films, up to about 50 nm. The transition metal L-edges can provide information up to about 100 nm, which is similar the film thicknesses used in this thesis.

For comparison the penetration depths have also been estimated in CoSi$_2$ and NiSi$_2$ from the elemental absorption coefficients. The results do not generally change the conclusions derived from the penetration depths in the pure elements. The variation between the two estimates depends, partly, on the density of the absorbing material. ($\rho_{Si} = 2.326$ g/cm^3, $\rho_{Co} = 8.789$ g/cm^3, $\rho_{Ni} = 8.91$ g/cm^3, $\rho_{SiO2} = 2.27$ g/cm^3, $\rho_{CoSi2} = 4.95$ g/cm^3 [9], $\rho_{NiSi2} = 4.859$ g/cm^3 [9]) Both NiSi$_2$ and CoSi$_2$ are about half the density of Ni and Co, thus, the X-rays at the metal edges are expected to penetrate further into the silicides than into the pure metals. The actual sampling depth of XAS depends on the detection

technique.

In Total Electron Yield (TEY) all electrons escaping the sample are detected. The majority of these electrons are low energy secondary electrons [6]. Studies of TEY in

Table 2.1. Photon penetration depth and X-ray absorption sampling depth estimates.

Edge	Thresh. Energy (eV)	Photon Penetration depth $(1/\mu)^a$		Primary Auger energy (keV)[b]	Est. TEY sampling depth[c] (Å)	Sampling depths[d] through SiO_2	
		Pure mat.	Silicide			TEY (nm)	FLY (nm)
Si L_3	99.2	37.4 nm	CS* - 23.6 nm NS* - 23.1 nm	0.09	Si - 14.7 CS - 6.9 NS - 7.1	5	70
Co L_3	778.1	89.6 nm	262 nm	0.73	Co - 73.2 CS - 130		
Ni L_3	852.7	95.9 nm	297 nm	0.85	Ni - 89.4 NS - 164		
Si K	1839	1.3 μm	CS - 0.79 μm NS - 0.76 μm	1.6	Si - 830 CS - 390 NS - 397	70	~100's
Co K	7709	3.0 μm	8.9 μm	6.1	Co - 1431 CS - 2540		
Ni K	8333	3.4 μm	10 μm	6.5	Ni - 1542 NS - 2828		

*The penetration and sampling depths have been calculated for CS ($CoSi_2$) and NS ($NiSi_2$) as well as the pure elements.

[a]From tables by B. L. Henke [7] and W. H. McMaster [8].

[b]KLL and LMM Auger energies are from A. Erbil [13] and T. A. Carlson [10].

[c]As calculated from the equation of L. Reimer [20].

[d]As taken from M. Kasrai [11].
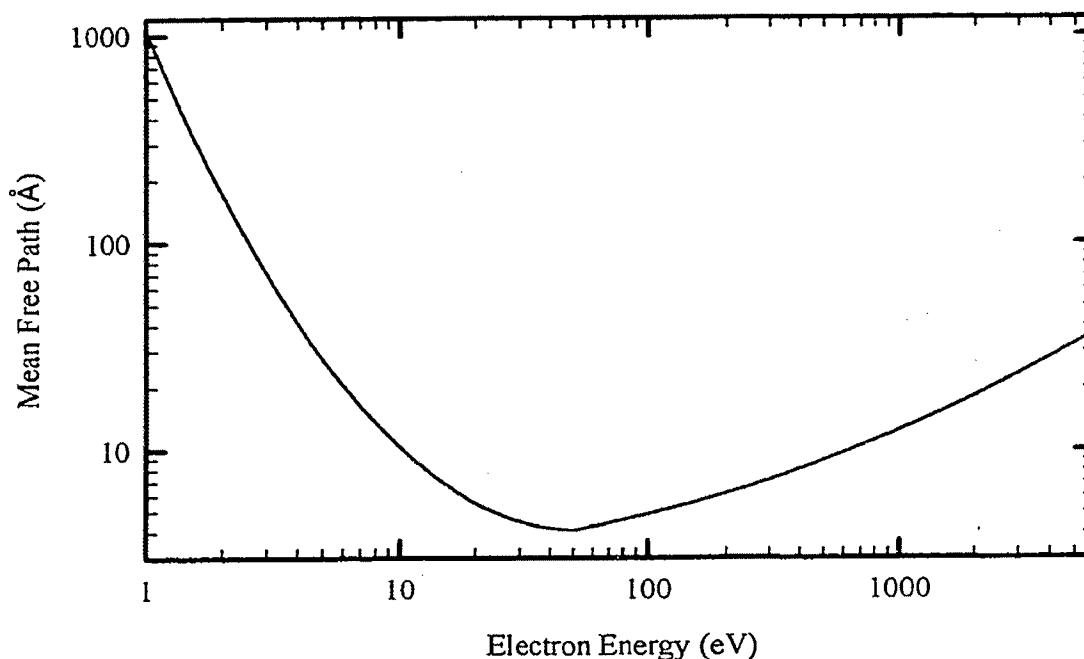
Figure 2.7. Plot of the universal curve for the mean free path of electrons in solids as a function of the kinetic energy of the electrons (E_K). (After J. Stöhr [6])

solids have demonstrated that the secondary electron signal is dominated by inelastically scattered Auger electrons. Thus, TEY is proportional to the Auger yield and the absorption [12][13][14].

On their way to the surface, the photoelectrons and Auger electrons created by the absorption process are scattered inelastically by electron-electron interactions. The mean free path (unscattered escape depth) of an electron in a solid is dependent on the energy of the electron and follows a universal curve shown in Figure. 2.7. It can be seen that the electron escape depth reaches a minimum of ~5Å (~ 2 ML) at an electron kinetic energy of about 50 eV. The universal curve represents the limit of the sampling depth if elastically scattered electrons are to be measured, as in photoemission or Auger spectroscopy.

Scattering of the primary photoelectron and Auger electron results in a cascade of secondary electrons as shown schematically in Figure 2.8. When the electrons reach the surface, only those with enough energy to overcome the surface potential barrier (work function, ϕ) will escape into the vacuum. This cascade of secondary electrons acts to

Vacuum
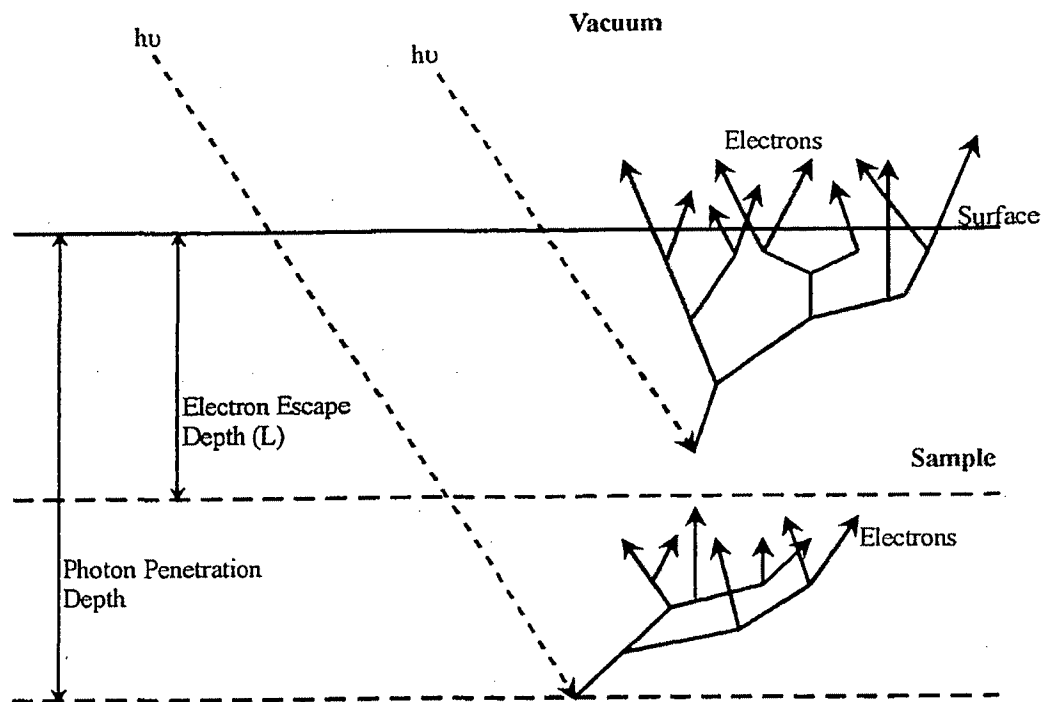
Figure 2.8. Schematic diagram of electron production in a solid after the absorption of a photon. Only electrons originating within a depth L from the surface will contribute to the TEY signal. (After J. Stöhr [6])

amplify the original high energy electron signal, thus, the secondary cascade carries the absorption information present in the primary Auger electrons (or photoelectrons). Since TEY measures mainly the secondary inelastically scattered electrons the sampling depth (L) extends to the point of the creation of the original high energy Auger electron which caused the secondary cascade (Figure 2.8) [6][12][13].

The value of the TEY sampling depth, therefore, depends on the distance over which the Auger electrons can travel and impart their energy to the surrounding electrons. Many estimates of the electron range in various solids have been made [15][16][17][18][19], however, the results differ by as much as a factor of 2 [13] for different definitions of the electron range and experimental methods. In general the electron range can be estimated by an empirical power law [15]. Making use of one such relationship (for electrons of energies from 1 - 10 keV) [13][20],

$$R \sim \frac{1000E^{1.4}}{\rho} \tag{2.4}$$

where R is the electron range in Å, E is the primary Auger electron kinetic energy in keV and ρ is the density in g/cm^3. Rough estimates for the TEY sampling depths at each edge studied have been made (Table 2.1). These estimates clearly show that the TEY sampling depth is much shorter than the photon penetration depth. In fact the sampling depth of TEY at the Si L-edge is expected to be only a few nm. It is interesting to note that since the electron range in a solid is dependent on the number of electrons present for scattering, and thus the density of the material, the TEY sampling depth in the pure metals (Co, Ni) is much shorter than for the silicides.

In fluorescence yield (FLY) the escaping fluorescence X-rays are attenuated in the same manner as the incident photons; thus the photon penetration depths serve as a reasonable estimate of the sampling depth of FLY measurements. Clearly TEY is a more surface sensitive technique than FLY X-ray absorption measurements.

Actual sampling depths for TEY have been measured experimentally for Al_2O_3 at the Al K-edge [21] and for Cu at the Cu K-edge [22]. T. Tyliszczak and A. P. Hichcock [23] have made measurements at the Cu, Mo and Mn K-edges while A. Erbil *et al.* [13] have compared the TEY, FLY and transmission detection modes for the Ge, Ni, Cu and As K-edges. For Si systems M. Kasrai *et al.* [11] have done an extensive study of the escape depths of both TEY and FLY techniques at the Si K and L-edges for the SiO_2/Si system. Their sampling depth values (Table 2.1) represent the sampling depths of TEY and FLY through SiO_2 layers at the Si absorption edges. Compared to the estimated sampling depths described above they at least have a similar magnitude.

The X-ray absorption work presented in this thesis involves silicide thin films covered by thin layers of SiO_2; thus, the sampling depth values of M. Kasrai *et al.* are used as reasonable estimates of our sampling depths at the Si K- and L-edges. Lacking any experimental data for the sampling depths at the transition metal edges, the estimates presented in Table 2.1 have been used.

2.3 PHOTOEMISSION SPECTROSCOPY

Absorption of a X-ray photon results in the ejection of a photoelectron. Photoemission spectroscopy (PES), also known as XPS and ESCA, examines the kinetic energy of the ejected electrons after the absorption of monochromatic photons. The emission of electrons under the influence of monochromatic light, termed the photoelectric effect, was first explained by Einstein [24]. Einstein used the principle of conservation of energy to relate the initial state energy (E_i) to the final state energy (E_f) of the system. This gave the simple equation now called the Einstein equation:

$$E_i + h\nu = E_f + E_K \qquad (2.5)$$

where E_K is the kinetic energy of an ejected electron and $h\nu$ in the incident photon energy.

Photoemission is inherently a many-body process; however, it can be described by a single particle approximation [25]. The many-body phenomena are seen as asymmetric lineshapes, shake down, shake up and shake off processes and where necessary can be
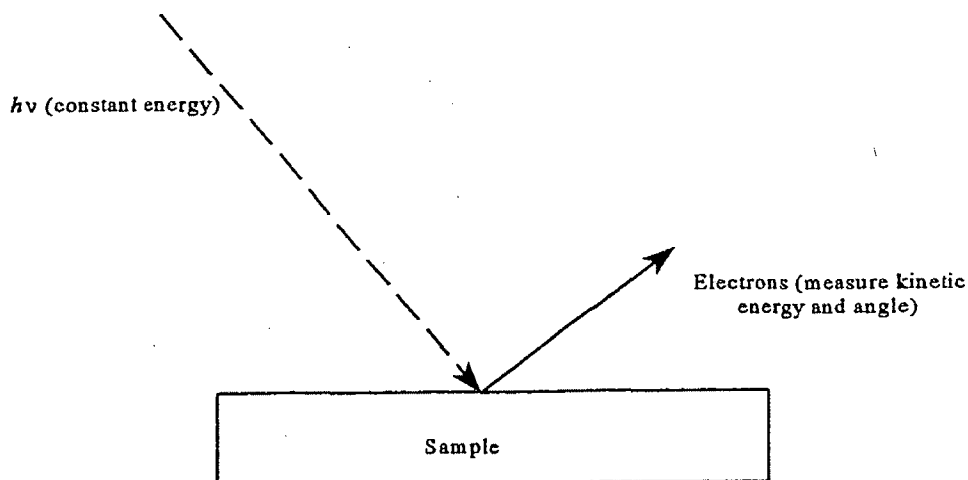
Figure 2.9. Schematic diagram illustrating the photoemission process.

dealt with as modifications to lineshape or background functions in the spectra. In the single particle approximation the above expression can be used to obtain the binding energy (E_B) of a core electron in an atom or molecule in the gas phase.

$$E_B = h\nu - E_K \tag{2.6}$$

In a solid, for an electron to be ejected, from the energy level it occupies within an atom, the incident radiation must have enough energy to overcome the binding energy of the electron as well as the work function (ϕ) of the solid. The work function is the energy separation between the Fermi level and the vacuum level and provides a barrier against the loss of electrons from the solid. Thus:

$$h\nu \geq E_B + \phi \tag{2.7}$$

By measuring the kinetic energy of the emitted photoelectron the binding energy can be calculated for elastically scattered photoelectrons,

$$E_B = h\nu - E_K - \phi \tag{2.8}$$

In a solid, after being ejected from a core level, a photoelectron must travel to the surface. Due to interactions with the surrounding atoms, some of the photoelectrons will be inelastically scattered (Figure 2.8). In photoemission, only those electrons which escape the sample without being inelastically scattered are detected. The depth from which photoelectrons can escape unscattered is governed by the mean free path, or electron escape depth, curve (Figure 2.7). The universal curve, as it is called, has a minimum of ~5Å at an electron kinetic energy of ~50 eV. Thus, a photoemission experiment carried out at a photon energy approximately 30-50 eV above the binding energy of the electron will be the most surface sensitive. It is also interesting to note that because of the shape of the universal curve the most rapid increase in the escape depth/eV

is obtained by decreasing the photon energy. One must however be careful as decreasing the kinetic energy of the photoelectrons also leads to an increase in the background.

2.4   SYNCHROTRON RADIATION

2.4.1   Introduction

Synchrotron radiation is the electromagnetic radiation emitted by electrons or positrons as they travel at relativistic velocities in large circular orbits. The description of the properties of synchrotron radiation can be traced back to the classical treatment of light emitted by accelerated charged particles by Larmor at the turn of the century [26].

Interest in this problem was revived in the 1940's with the advent of electron accelerators with closed orbits. It was found that emission of synchrotron radiation limited the energy achievable by accelerators such as the betatron [27]. Thus synchrotron radiation was labelled a technical nuisance in accelerator physics. Experimentally synchrotron radiation was first seen in 1946 at the General Electric Laboratories [28]. Finally in 1956 the potential of this nuisance as a powerful research tool for ultraviolet and soft X-ray absorption spectroscopy was realized [29]. Its usefulness for hard X-ray experiments [30] was quickly recognized as well.

In the early years, synchrotron radiation was not considered important enough to justify the building of accelerators dedicated to its production, thus, the pioneering work with synchrotron radiation was done by obtaining the light as a by-product from elementary particle accelerators. This parasitic arrangement had many negative aspects for synchrotron radiation users since the parameters for operating the accelerators were optimized for the elementary particle experiments and were not suited for efficient synchrotron radiation use. These parasitic facilities were the so-called first generation sources.

The second generation of synchrotron sources was started by the building in 1966, at the University of Wisconsin-Madison, of Tantalus. Its operation stimulated the building

of many second generation synchrotron storage rings around the world. A storage ring has the great advantage of being able to supply a source of tuneable photons. Continuous development of the accelerator machinery has improved the performance of the storage rings and given rise to a third generation of sources which have started operation in the last few years.

2.4.2 Synchrotron sources

A typical synchrotron storage ring facility is shown schematically in Figure 2.10. It consists of two main components, the storage ring and the beamlines. The storage ring keeps charged particles circulating under vacuum in a closed orbit at relativistic speeds. Whenever an electron is bent around a corner it emits electromagnetic radiation on the tangent to its path. The beamlines convey the radiation emitted to the experimental chamber and provide a means of selecting a particular photon energy from the spectrum.

The major components of the storage ring are:

1) The injection system, which generates electrons, accelerates them and injects them into the vacuum chamber. The injection system can range from a simple microtron, linear accelerator (Linac) to a small synchrotron.

2) The storage ring vacuum chamber. This is the metal tube through which the electrons circulate under ultrahigh vacuum. The vacuum is necessary to prevent loss of electrons by scattering off residual gas particles.

3) The bending magnets. Are the main magnetic elements responsible for directing the electrons around a closed orbit.

4) The radiofrequency cavity, which replenishes the energy lost by the electrons (emitted as synchrotron radiation) in a circuit of the ring. The cavity works by supplying a radio wave of the appropriate frequency so that as an electron passes through the cavity it is subjected to an electric field gradient which accelerates the electron through the cavity.

5) Other control magnets (quadrupole and sextupole), which are responsible for

SYNCHROTRON STORAGE RING

Accelerating
(RF) cavity

Straight section

Injection ring

Bending Magnets

Beamlines

Bending Magnet

Synchrotron Radiation

Quadrupole Magnets
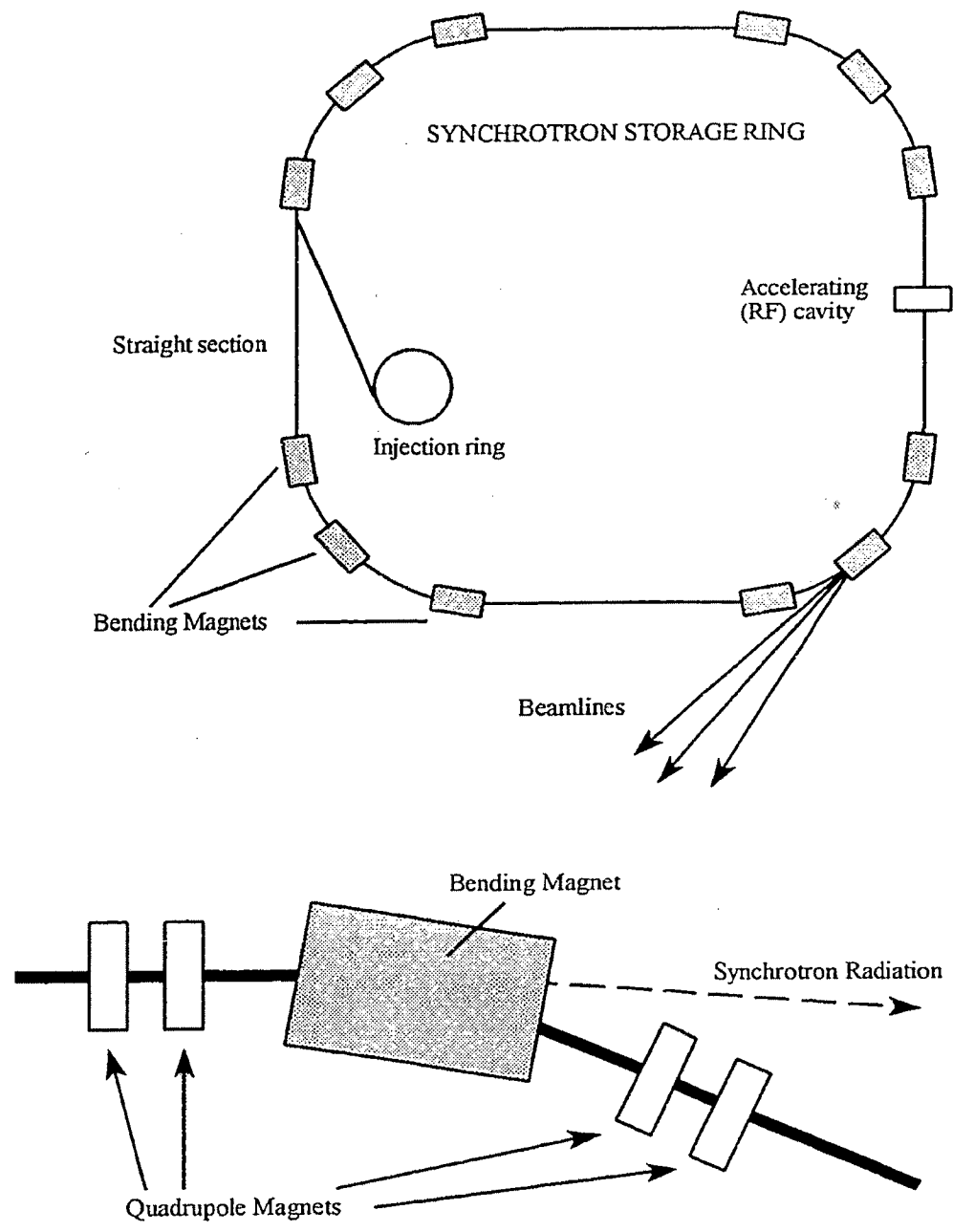
Figure 2.10 Representation of a synchrotron storage ring showing the major components.

controlling the orbit of the electrons in the ring as well as the physical size of the beam.

6) Insertion devices. Insertion devices are periodic arrays of additional magnets which produce synchrotron radiation in straight sections of the ring by causing the beam to describe a sinusoidal path along the direction of travel. These devices are most common in third generation sources.

7) The beam ports, which allow the emitted light from bending magnets or insertion devices down the beamlines.

In general, electrons (or positrons) are generated in the injection system where they are accelerated to some energy below that of the final operating energy. They are then injected into the ring in bunches (responsible for the pulsed structure of the emitted radiation) until a certain ring current in reached (20 - 500 mA). By increasing the magnetic field in the bending magnets the electron beam is accelerated to high energies (200 MeV to 10 GeV) which are characteristic of specific synchrotrons (see Table 2.2). Once the operating energy and current have been obtained the electrons can be stored in the synchrotron for many hours under the action of the RF cavity.

2.4.3 Properties [1]

X-ray absorption and photoemission experiments can be carried out using conventional sources, such as a rotating anode, and line sources of Al $K\alpha$ (1486.6 eV), Mg $K\alpha$ (1253.6 eV) or He I (21.2 eV) photons, respectively. The line sources only provide photon beams at a few energies and with only modest intensity. Experiments using these sources must thus be limited to the photon energies available and long acquisition times. The use of synchrotron radiation alleviates these problems and was one of the driving forces behind the development of synchrotron sources. A synchrotron radiation source provides electromagnetic radiation over a wide spectral range from the infrared (10^{-2} eV, $\lambda=10^6$ Å) to hard X-rays (10^5 eV, $\lambda=10^{-1}$ Å), with a high intensity over the whole range.

The power (P) radiated by an accelerated charged particle moving on a circular path is given by:

$$P = \frac{2e^2cE^4}{3\rho^2(m_0c^2)^4}$$

(2.9)

where ρ is the radius of curvature of the bending magnet and is independent of the radius of the ring. Note that the power radiated increases as the fourth power of the ring energy (E) and decreases as the fourth power of the rest mass (m_0). This effect explains why lighter elementary particles such as electrons and positrons are used to generate synchrotron radiation in storage rings even though any accelerated charged particle will generate synchrotron radiation.

The spectral distribution of a synchrotron is affected by two main criteria, the energy of the ring and the radius of curvature of the bending magnets. We can define a parameter called the critical wavelength (λ_c) at which the maximum flux of photons occurs. λ_c is also correlated to the high photon energy cut off characteristic of the spectral distribution (Figure 2.11).

$$\lambda_c = \frac{4\pi\rho}{3\gamma^3}$$

(2.10)

where $\gamma = E/m_0c^2$. For example the Aladdin storage ring, at University of Wisconsin-Madison, with an operating energy of 0.8 GeV and a radius of curvature of 2.0833 m has a critical wavelength of 22.7 Å (546 eV). Figure 2.11 shows the spectral distribution of the Aladdin storage ring operating at 0.8 GeV and 200 mA and at 1.0 GeV and 100 mA. Table 2.2 gives some ring parameters for the synchrotron storage rings used for this thesis work.

Other advantages of synchrotron radiation are:

1) Its inherent collimation; synchrotron radiation is emitted over a narrow range of angles creating a small intense beam of light which allows it to be more easily
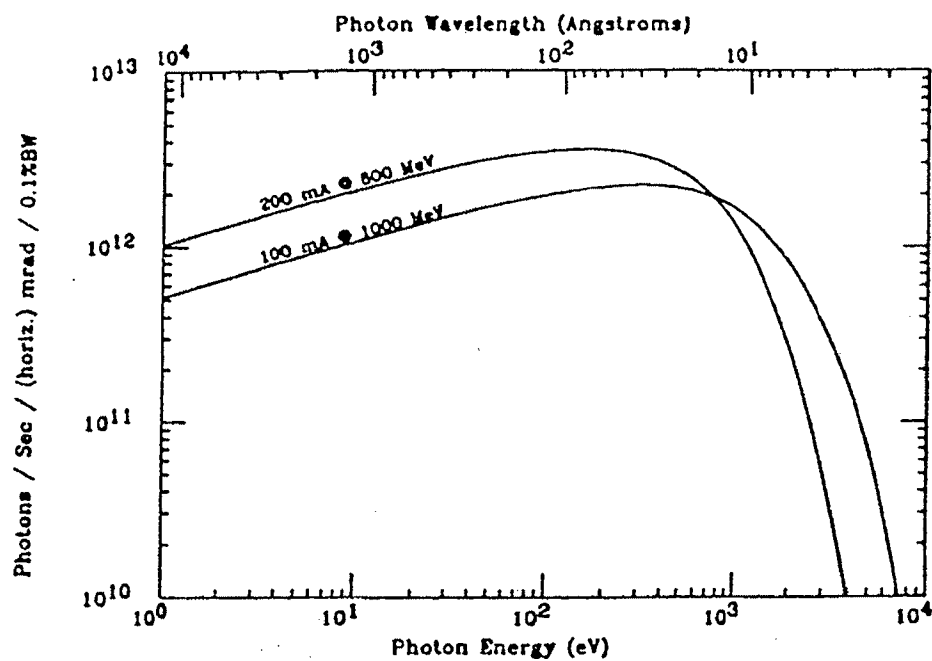
Figure 2.11. Bending magnet flux of the SRC storage ring under two typical operating conditions. (From SRC publication [31])

Table 2.2. Synchrotron radiation sources used for studies presented in this thesis.

Name	Location	Critical Energy (keV)	Electron Energy (GeV)	Typical Beam Current (mA) at injection
ALADDIN[a]	Stoughton, WI	0.55 or 1.07	0.8 or 1.0	200 or 100
NSLS (X-Ray)[b]	Brookhaven, NY	5.08	2.5	200

[a]From SRC publication [31]

[b]From NSLS publication [32]

directed and focused onto samples.

2) Its time structure; light emitted by storage rings comes as a series of short (nsec) pulses; this allows investigations into rapidly occurring kinetic processes.

3) Its polarization; the beam of light generated by a synchrotron is polarized linearly in the plane of the ring and circularly polarized above and below this plane. This property has been utilized to perform magnetic circular dichroism measurements in the X-ray region.

2.4.4 Monochromators

Once the spectrum of electromagnetic radiation has been emitted by the circulating electrons in the storage ring, it must be processed into a usable beam. The synchrotron source must therefore be complemented by a beamline which contains the shutters, apertures, mirrors and diffracting elements required to focus and filter the spectrum of X-rays to obtain a monochromatic beam of the desired size. Most of the optical elements in a beamline form a coordinated unit called the monochromator. Valves and shutters, which isolate vacuum of the beamline from that in the storage ring and experimental chamber, and refocusing mirrors, which direct the monochromatized radiation to the experiment, comprise the remainder of the elements in the beamline.

The monochromator uses diffraction to select a specific photon energy from the total distribution emitted by the synchrotron and is the central and largest part of a beamline. The monochromator consists of the diffracting elements along with coordinated mirrors and slits. A number of different types of monochromators exist and they can be grouped into two main types, grating monochromators and crystal monochromators.

In order to obtain the best resolution the spacing of the diffraction elements must be close to the wavelength of the desired light. In the UV and soft X-ray region (λ=100 - 1000 Å) mechanically produced ruled gratings are most effective, while, in the hard X-ray region (λ=10 Å or less) diffraction from the atomic planes in a crystal provides the best results.
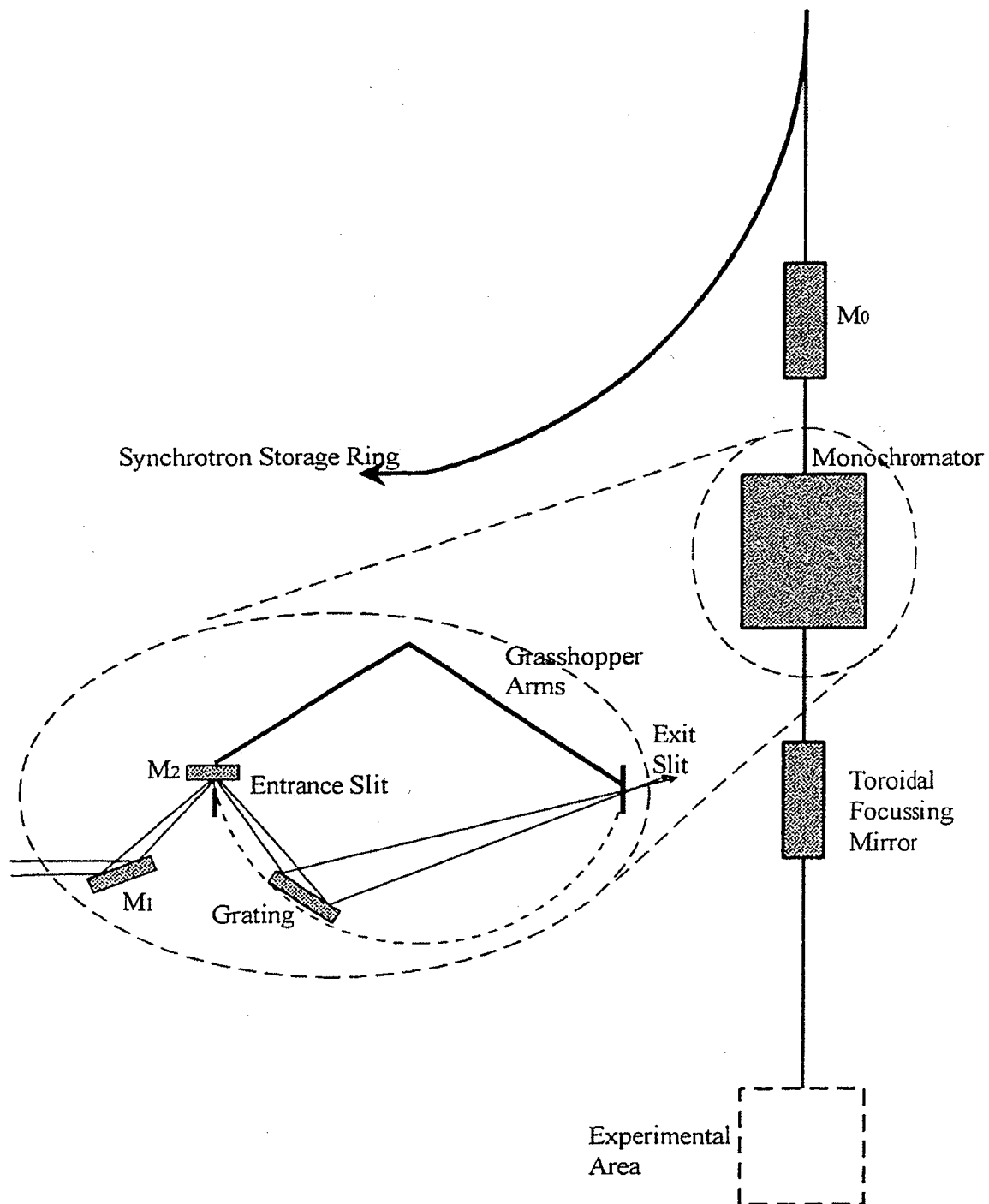
Figure 2.12. Schematic of the CSRF Grasshopper beamline located at SRC.

2.4.4.1   Grating Monochromators

The typical optical elements of a grating monochromator are illustrated in Figure 2.12. In this monochromator (Canadian Grasshopper located at the Canadian Synchrotron Radiation Facility (CSRF) at the Synchrotron Radiation Centre (SRC), University of Wisconsin-Madison) the synchrotron radiation is first reflected off a gold-coated curved mirror (M_0) which focuses the light into the monochromator. Next, the mirror (M_1) focuses the light at a grazing angle into the entrance slit and mirror M_2 which directs the beam onto the grating. The grating disperses the radiation, and light of the desired photon energy passes through the exit slit and is focused onto the experiment by a refocusing mirror. The desired photon energy is selected by the relative positions of M_1, M_2 and the grating with respect to the exit slit. The complicated, concerted linear and rotary motions required by the grating and mirrors are controlled by a single computer controlled stepping motor. The moving optical elements are kept in alignment by a physical toggle mechanism attached to two long arms (the grasshopper legs). More modern monochromator designs such as HERMON make use of stepping motors for each rotation or translation of the optical elements with the positions monitored by laser interferometry.

The motion of the elements in the monochromator could be simplified but this would lead to the position of the final focus moving in space. For soft X-rays and UV light the photon beam must be kept under vacuum. The beamline and experiment must thus be housed in vacuum chambers. The cost and difficulty in translating experimental chambers to keep the light focused on the sample is prohibitive and grating monochromators are designed to be fixed exit devices.

Grating monochromators make use of a diffraction grating which is a reflecting surface with a periodic array of lines inscribed on it. The general diffraction conditions from a grating are given by the grating equation,

$$n\lambda = d(\sin\alpha + \sin\beta) \qquad (2.11)$$

where n is the order of diffraction, d is the distance between the lines, α is the angle of incidence and β is the angle of diffraction. Gratings can be either plane, concave spherical or concave aspherical. Each type of grating shape has special characteristics of focus, resolution and optimum operating range. Specifically non-planar gratings allow simultaneous focusing and dispersion which can decrease the number of optical elements in a monochromator making these monochromators cheaper and simpler.

The grating beamlines used in this work were the Canadian Grasshopper and the High Resolution Monochromator (HERMON) located in SRC at the University of Wisconsin-Madison. The monochromators used in this work are listed in Table 2.3.

Table 2.3. Beamlines used for work presented in this thesis.

Beamline	Location	Energy Range (eV)	Type	Grating or Crystal	Approx. Spot Size (mm)[a]
Canadian Grasshopper	CSRF, SRC-Madison, WI	40 - 1000	Spherical Grating	1800 g/mm	7H × 1V
HERMON	SRC-Madison, WI	245 - 1100	Plane Grating	variable spacing	1H × 1V
Canadian DCM	CSRF, SRC-Madison, WI	1500 - 4000	DCM	InSb(111)	5H × 2V
X-11A	NSLS Brookhaven, NY	4500 - 26000	DCM	Si(111)	10H × 0.5V

[a]For the spot sizes H means horizontal and V means vertical

2.4.4.2 Crystal Monochromators

In the hard X-ray region diffraction from the crystal planes of single crystals is used to monochromatize the radiation. The most common design is the Double Crystal Monochromator which uses the sequential Bragg ($n\lambda = 2d\sin\theta$) diffraction from two
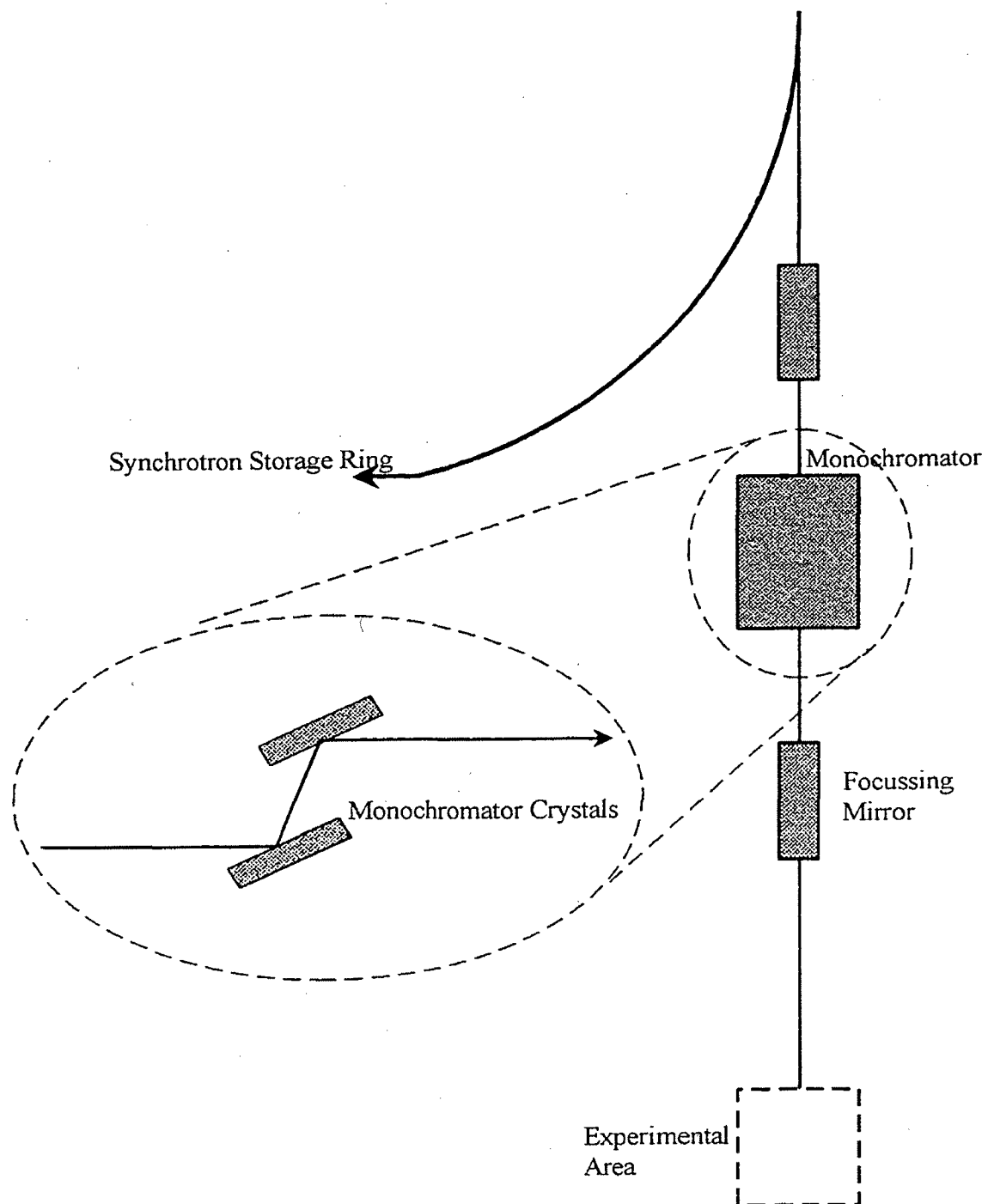
Figure 2.13. Schematic of a typical Double Crystal Monochromator beamline.

aligned crystals to achieve the dispersion of the light (Figure 2.13). The synchrotron radiation emitted by the ring is focused onto the first crystal where it is scattered onto the second crystal. Refocusing mirrors follow the monochromator to focus the light to the desired experimental station. The work presented in this thesis used the X-11A beamline located at the National Synchrotron Light Source (NSLS) at Brookhaven National Labs and the Canadian DCM located in CSRF at SRC.

2.5   CALCULATION OF DENSITY OF STATES

In this thesis X-ray absorption near edge structure (XANES) has been used to study the electronic structure of thin film samples. A mentioned previously (Sect. 2.2) the structure in a XANES spectrum represents the density of unoccupied states of allowed symmetry to which the ejected core electron can be promoted after the absorption of a photon. Theoretically calculated spectra can be used to help identify the origin of changes seen in complicated series of spectra.

Methods for calculating the electronic structure of crystalline solids have been well developed over many years. Recently new approaches and codes have been developed which, together with hardware development, allow calculations to be done quickly on workstations and PCS. This allows individual researchers to supplement their work with their own calculations.

The electrons and nuclei that compose materials comprise a strongly interacting many-body system. In principle the properties of such systems can be calculated quantum mechanically if a sufficiently accurate approximate technique can be employed. Calculations based on the Local Density Approximation (LDA) within the Density Functional Theory (DFT) have become some of the most important approximate methods used in the study of materials science. Excellent reviews exist on these methods [33][34][35][36] and the present discussion is not intended as a comprehensive review.

The program WIEN97 [37] was used to calculate the densities of states of various metal silicides from their known crystal structures. WIEN solves the Kohn-Sham

equations [38] to obtain the density of electronic states. Density functional theory [39] states that the total energy and other ground state properties of a system of interacting electrons in an external potential are given exactly as functionals of the ground state electronic density. In order to solve the Kohn-Sham equations WIEN uses the LAPW (Linear Augmented Plane Wave) basis set.
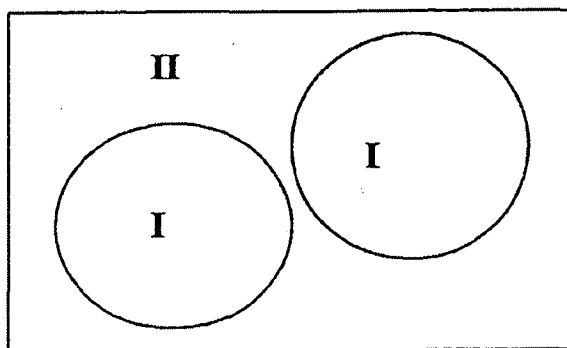
Figure 2.14 Partitioning of the unit cell into atomic spheres and an interstitial region.

In LAPW the unit cell is divided into two parts: the atomic spheres (I) and the interatomic regions between spheres (II). Inside the spheres a linear combination of radial and spherical harmonics is used as the basis set while outside the spheres (region II) plane waves are used. They are normalized to match in value and slope at the boundary between the regions. The normalized functions obtained are the LAPW basis set.

Once the electronic density has been calculated, WIEN uses the modified tetrahedron method of Blöchl et al. [40] to calculate the Densities of States (DOS). The X-ray absorption spectra are determined by using Fermi's golden rule and dipole matrix elements (between the core and conduction band states) to calculate appropriate DOS which are then broadened by a Gaussian function to simulate the absorption spectra [41].

2.6 SUMMARY

Photoemission spectroscopy (PES) and X-ray Absorption Near-Edge Structure spectroscopy (XANES) investigate different aspects of the electronic structure, which can be related to the material's physical structure.

PES maps out the occupied density of states below the Fermi level (refer to the left side of Figure 2.3). The essential information in PES is the binding energies (E_B) of the core levels. Changes in the valence charge around the absorbing atom (due to bonding) are evident in the Valence Band (VB) structure and in shifts of the core-level binding energies as compared to those of the pure compound. The core level shifts are reproducible for a specific compound and thus serve as a fingerprint of the physical structure (chemical environment of the absorbing atom) present. In VB photoemission spectra the energy levels overlap and the contributions from various elements and levels is difficult to determine exactly.

XANES maps out the unoccupied density of states above the Fermi level. Like PES, XANES is also site specific and maps the local electronic structure about the absorbing atom. The spectral features depend on the physical (crystal) structure of the compound and as in PES act as a fingerprint to the physical structure of the compound.

The threshold energy (the photon energy at which the absorption jump occurs) is a measure of the binding energy (difference between the Fermi level and the core-level) of the absorbing core-level in metallic systems. The threshold energy shifts between compounds can thus be compared to PES core-level binding energy shifts.

Unlike PES, XANES is limited by the dipole selection rules; thus it maps out only those portions of the total unoccupied density of states with the correct symmetries. Comparison of the intensity features in XANES spectra between compounds thus allows information about the types (s, p or d) and elemental origin of charges to be determined.

Using synchrotron radiation rather than conventional X-ray sources allows us to access the complete range of core-levels from 50-20000 eV with high-resolution. Choice of specific core-levels at both high and low energies is essential to allow both surface and

bulk sensitive electronic structures to be determined.

PES was used to study the evolution of the Au/Si(100) surface in the sub-monolayer regime in Chapter 3. XANES was used in Chapters 4 and 5 to study the electronic and physical structures in thin films of Co and Ni silicides with depth and elemental resolution.

2.7 REFERENCES

[1]   G. Margaritondo, *Introduction to Synchrotron Radiation* (Oxford University Press, New York, 1988).

[2]   T. K. Sham, Phys. Rev. **B31**, 1888 (1985).

[3]   P. W. Atkins, *Molecular Quantum Mechanics*, 2nd ed. (Oxford University Press, Oxford, 1983), p. 198.

[4]   A. N. Mansour, J. W. Cook, Jr. and D. E. Sayers, J. Phys. Chem. **88**, 2330 (1984).

[5]   See for example, D. C. Koningsberger and R. Prins, *X-ray Absorption: Principles, Applications, Techniques of EXAFS, SEXAFS and XANES* (Wiley-Interscience, New York, 1988).

[6]   J. Stöhr, in *X-ray Absorption: Principles, Applications, Techniques of EXAFS, SEXAFS and XANES*, eds. D. C. Koningsberger and R. Prins (Wiley-Interscience, New York, 1988), Ch. 10.

[7]   B. L. Henke, P. Lee, T. J. Tanaka, R. L. Shimabukuro and B. K. Fujikawa, Atomic Data Nucl. Data Tables **27**, 1 (1982).

[8]   W. H. McMaster, N. Kerr Del Grande, J. H. Mallett and J. H. Hubbell, *Compilation of X-Ray Cross Sections* (Lawrence Radiation Laboratory, UCRL-50174, 1967).

[9]   K. Maex and M. Van Rossum, eds., *Properties of Metal Silicides* (Inspec, London, 1995).

[10]   T. A. Carlson, *Photoelectron and Auger Spectroscopy* (Plenum, New York, 1975), Ch. 6.

[11]   M. Kasrai, W. N. Lennard, R. W. Brunner, G. M. Bancroft, J. A. Bardwell and K. H. Tan, Appl. Surf. Phys. **99**, 303 (1996).

[12]   J. Stöhr, *NEXAFS Spectroscopy*, Springer Series in Surface Science Vol. 25 (Springer, Berlin, 1992), Ch. 5.

[13]   A. Erbil, G. S. Cargill III, R. Frahm and R. F. Boehme, Phys. Rev. B **37**, 2450 (1988).

[14]   J. Stöhr, C. Noguera and T. Kendelewicz, Phys. Rev. B **30**, 5571 (1984).

[15]   L. Reimer, *Scanning Electron Microscopy*, Springer Series in Optical Sciences Vol. 45 (Springer-Verlag, Berlin, 1985), pg. 100.

[16]   J. E. Holliday and E. J. Sternglass, J. Appl. Phys. **30**, 1428 (1959).

[17]   H. Kanter, Phys. Rev. **121**, 461 (1961).

[18]   H. Kanter and E. J. Sternglass, Phys. Rev. **126**, 620 (1962).

[19]   V. E. Cosslett and R. N. Thomas, Br. J. Appl. Phys. **29**, 331 (1970).

[20]   L. Reimer, Scanning Electron Micros. **II**, 111 (1979).

[21]   R. G. Jones and D. P. Woodruff, Surface Science **114**, 38 (1982).

[22]   G. Martens, P. Rabe, G. Tolkiehn and A. Werner, Phys. Status Solidi A **55**, 105 (1979).

[23]   T. Tyliszczak and A. P. Hichcock, Physica B **158**, 335 (1989).

[24]   A. Einstein, Ann. Phys. (Leipzig) **17**, 932 (1905).

[25]   T. Koopmans, Physica **1**, 104 (1934).

[26]   J. Larmor, Phil. Mag. **44**, 503 (1897).

[27]   D. Ivanenko and J. Pomeranchuck, Phys. Rev. **65**, 343 (1944).

[28]   F. R. Elder, A. M. Gurewitsch, R. V. Langmuir and H. C. Pollock, Phys. Rev. **71**, 829 (1947).

[29]   D. H. Tamboulian and P. L. Harman, Phys. Rev. **102**, 1423 (1956).

[30]   L. G. Paratt, Rev. Sci. Instrum. **30**, 297 (1959).

[31]   *An Invitation to See the Light* (SRC publication, Stoughton, WI, 1993).

[32]   *NSLS Experimenters Handbook* (NTIS, Springfield, VA, 1988).

[33]   J. Callaway and N. H. March, Solid State Physics **38**, 135 (1984).

[34]   R. M. Dreizler and J. de Provincia, Density Functional Methods in Physics, (Plenum, New York, 1985).

[35]   R. G. Parr and W. Yang, Density-Functional Theory of Atoms and Molecules, (Oxford University Press, New York, 1989).

[36]   D. Singh, Plane Waves, Pseudopotentials and the LAPW method, (Kluwer Academic, Boston, 1994).

[37]   P. Blaha, K. Schwarz and J. Luitz, **WIEN97**, Vienna University of Technology 1997. (Improved and updated Unix version of the original copyrighted WIEN-code, which was published by P. Blaha, K. Schwarz, P. Sorantin and S. B. Trickey, Comput. Phys. Commun. **59**, 399 (1990)).

[38]   W. Kohn and L. J. Sham, Phys. Rev. **140**, A1133 (1965).

[39]   P. Hohenberg and W. Kohn, Phys. Rev. **136**, B864 (1964).

[40]   P. E. Blöchl, O. Jepsen and O. K. Anderson, Phys. Rev. B **49**, 16223 (1994).

[41]   A. Neckel, K. Schwarz, R. Eibler and P. Rastl, Microchim. Acta, Suppl. **6**, 257 (1975).

CHAPTER 3: THE GOLD ON SILICON (100) INTERFACE

3.1 INTRODUCTION

3.1.1 Introduction

Surface and interface phenomena can be considered the core of semiconductor physics. Semiconductor devices are based on metal/semiconductor and semiconductor/semiconductor junctions. The atomic structures formed at these interfaces are critical in determining the ultimate electronic properties of devices. As the lateral size of the devices continues to shrink, the thickness of the ohmic contact layers must approach a few tens of monolayers. In this ultra-thin film regime the electrical properties and morphology of the films can become dominated by interfacial effects. Relevant examples of this are the observed room temperature reactions between silicon and a few monolayers of deposited Co [1] and Ni [1][2][3], while thicker (nm) deposits only show significant reaction to form stable silicides after being annealed to a few hundred degrees Celsius. Thus, a detailed knowledge of the structure of metal/silicon interfaces is of significant value to the semiconductor industry for the continued development of semiconductor devices.

Despite the importance of interfacial phenomena, a fundamental understanding has been slow in developing. The main reason for this is the complexity of the puzzle. Surface and interfacial structures are determined by the interaction of many small effects. Elastic strain, coulomb energy, rehybridization energy, surface energy and the structure of the clean surface, to name a few, can all affect the final structure of an interface.

In studying metal/semiconductor interfaces two main approaches have been adopted, the top-down approach and the bottom-up approach. In the top-down approach the interface to be studied is formed then it is covered, either by layers of the top component of the interface or by capping layers of another substance. The properties of the interface are then investigated. The capping layers prevent further reactions from occurring at the interface and create a realistic environment similar to that in which the interface is usually found. Although the information gathered is readily applicable to a functioning device, it can be limited. The material above the interface prevents the use of many of the most powerful tools available to the surface scientist, such as Scanning Tunnelling Microscopy (STM), Atomic Force Microscopy (AFM), Low Energy Electron Diffraction (LEED) and Photoemission Spectroscopy (PES), which are sensitive only to the top few monolayers of the sample.

The bottom-up approach follows the evolution of the interface as the metal is slowly deposited onto the substrate. This approach allows the use of the common surface science tools but whether the information obtained reflects the 'true' buried interface is an open question. Pure surface effects, such as surface tension and rate of metal deposition, can affect the interface as can the absence of the normally present overlayers. Despite their limitations, both approaches have contributed to the fundamental understanding of interfaces.

In this chapter we will follow the bottom-up approach to study the formation of the Au/Si(100) interface using synchrotron based photoemission spectroscopy.

3.1.2   The Au/Si system

The noble metals (Au, Ag, Cu) on silicon are representative of the broad range of interfacial phenomena [4]. Ag forms a non-diffusive interface, Cu forms a diffusive interface with stable compound formation and Au forms a diffusive interface with no stable compound formation [4]. Of these three, Au is perhaps the most interesting, as according to the phase diagram (Figure 3.1), Au is not expected to react with silicon; the
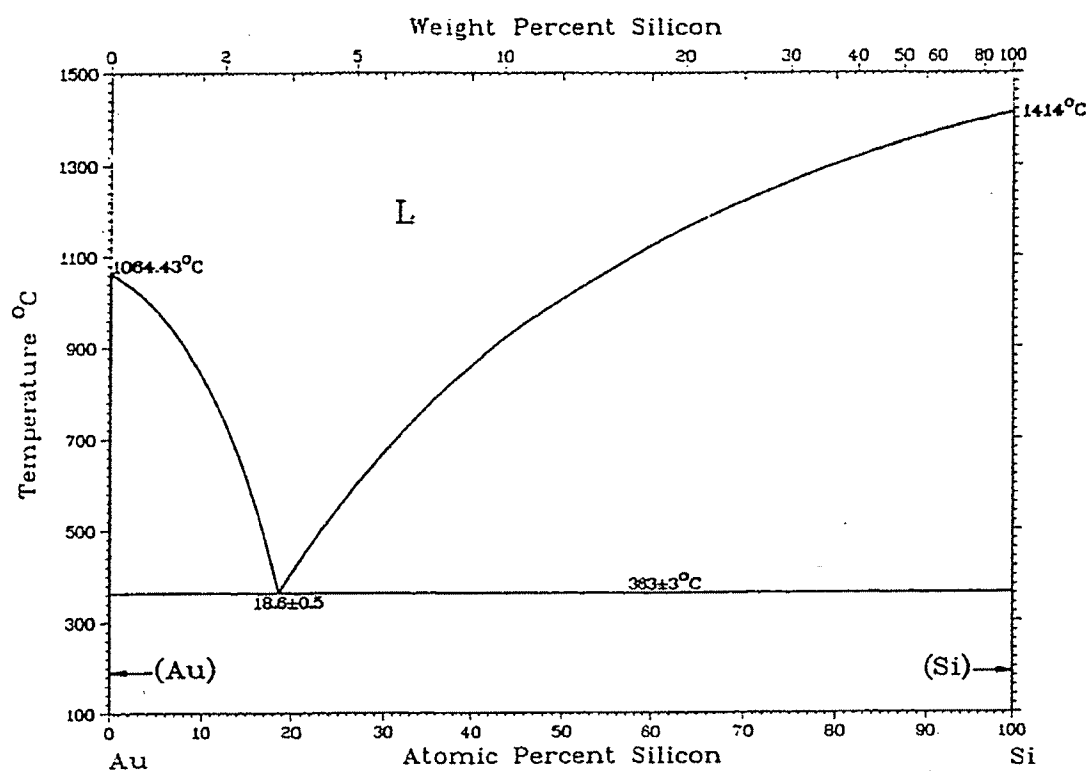
Figure 3.1. The Au-Si phase diagram. (From T. B. Massalski [5], used with permission)

two are immiscible and only form a eutectic at 300 °C. However, Au, when deposited on a silicon surface, reacts at room temperature. The uniqueness of the Au/Si system, along with Au's possible use as a metal/silicon contact in integrated circuit manufacture, have made it an extensively studied system [6].

Work on the gold-silicon system was stimulated by the observations that at room temperature, silicon can out-diffuse to the surface of Au layers several hundred angstroms thick [7], and that gold catalyzes the formation of silicon oxide on silicon surfaces [8]. Both of these observations indicated an interfacial reaction in which Au breaks the covalent Si-Si bonds, providing free Si atoms at the interface. The unique ability of Au to induce Si bond breaking is perhaps the central feature of the Au/Si interface formation.

Indeed, the presence of free Si induced by adsorbed Au has been used as a promoter of Si diffusion in the formation of Pt [9] and Ag [10] silicides. Small amounts of Au are also used to crystallize amorphous Si below 250°C [11] (well below the pure Si crystallization temperature of 550 °C). The unique properties of the Au/Si interface are also behind the process of Au-Si eutectic bonding which is used to attach a Si wafer to a ceramic support or another wafer [12].

The high reactivity of the Au/Si interface, although useful and scientifically intriguing, is highly undesirable for making contacts and interconnects in integrated circuit manufacturing. As a result, research into controlling gold's interaction with silicon has been pursued. This research usually focuses on the blocking of the Si surface states by reacting them with another atom, such as H [13][14][15][16].

The majority of the research into the Au/Si interfacial structure has been done on the Si(111) surface [6]. The first point to raise is that at room temperature the interface does not develop a Au-induced ordered structure. At higher temperatures, numerous Au-silicide metastable phases have been seen [17]. Overall, the room temperature junction develops such that three distinct regions form above the Si substrate (see Figure 3.2).

1) A diffuse alloyed zone (about 10 ML thick) develops on the Si substrate. The composition is unknown and both Au-rich and Si-rich stoichiometry have been reported. Small Au crystallites have also been found throughout this layer [4][18].

2) Next a layer of Au is found.

3) Finally a thin (1-2 ML) Au-rich alloy or compound forms on the surface. The composition of this phase is unknown but it appears to be close to Au_3Si [19].
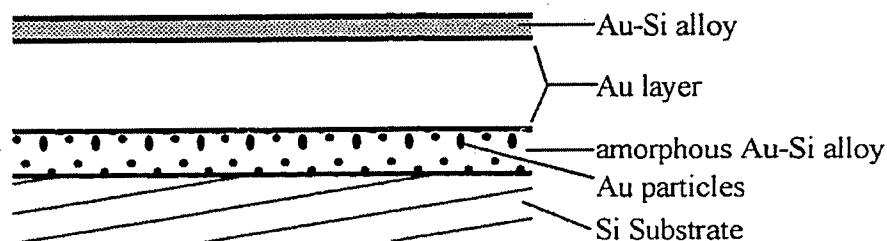
Figure 3.2. General picture of the Au/Si interfacial structure.

This picture of the Au-Si interface points to the complexity of the Au-Si interactions. A number of questions about the interface have defied solid answers. These include:

1) Whether a critical thickness of Au on the surface is required before the initial Au-Si interaction proceeds.

2) Whether there exists a minimum Au coverage before Si begins to diffuse to the surface or, as has recently been suggested [19], whether the Au layer forms between the top silicide layer and the Si substrate.

3) Whether the alloy phase formed at the Au-Si interface remains or whether the Au-Si interface becomes atomically abrupt.

4) The exact positions of the atoms in the interfacial structure.

Many of the discrepancies between experimental data concerning the interfacial structure and reactions may stem from, a) the dependance of the reactions on surface preparation and dosing rates which have not been adequately controlled, and b) the limitations in spatial and depth resolution of the experimental techniques used.

The Au/Si(100) interface, although more important technologically, has been less investigated [4][18][20][21][22][23][24][25][26][27][28][29][30][31]. The basic

properties of this interface have been found to be very similar to those of the Au/Si(111) interface. The main differences are with the thicknesses of the layers and the rate at which the interface forms.

Photoemission using synchrotron radiation has been found to provide detailed information about the structures of surfaces. The first photoemission study on the Au/Si interface was done on Si(111) by Braicovich *et al.* [32], making use of the valence band and both the Si 2p and Au 4f core-levels. In the study of the Au/Si(100) interface formation, mostly Auger electron spectroscopy has been used along with valence-band photoemission to study the surface [20][25][27][28][29].

X. F. Lin and J. Nogami [31] have investigated the Au/Si(100) interface at room temperature using Scanning Tunnelling Microscopy (STM). Their results indicate that the first monolayer of Au deposits in an ordered structure, afterwards the interface develops layer by layer in a disordered fashion.

Core-level photoemission studies on the Si(100) interface have only been done infrequently [27][28][30].

The goal of the research into the Au/Si system has been to understand the growth and resulting structures present at the interface. An understanding of the structures present at the interface, and possibly how to control them, is critical to understanding the electronic behaviour of the interface. Despite extensive effort the goal has remained elusive especially for the Si(100) surface.

This study will investigate the formation of the Au/Si(100) interface at room temperature in the sub-monolayer and monolayer regimes using high resolution photoemission spectroscopy.

3.1.3 Si(100)

In order to study the interaction of Au on the Si(100) surface we first must understand the structure of the surface and how this is seen by photoemission.

Silicon crystallizes in the diamond structure (Figure 3.3B) and like diamond is a

A) The Miller indices of three common crystal planes.

(100) plane

(110) plane

(111) plane

B)

Diamond structure (FCC)

C)

Dangling bonds

(111) plane

(100) plane
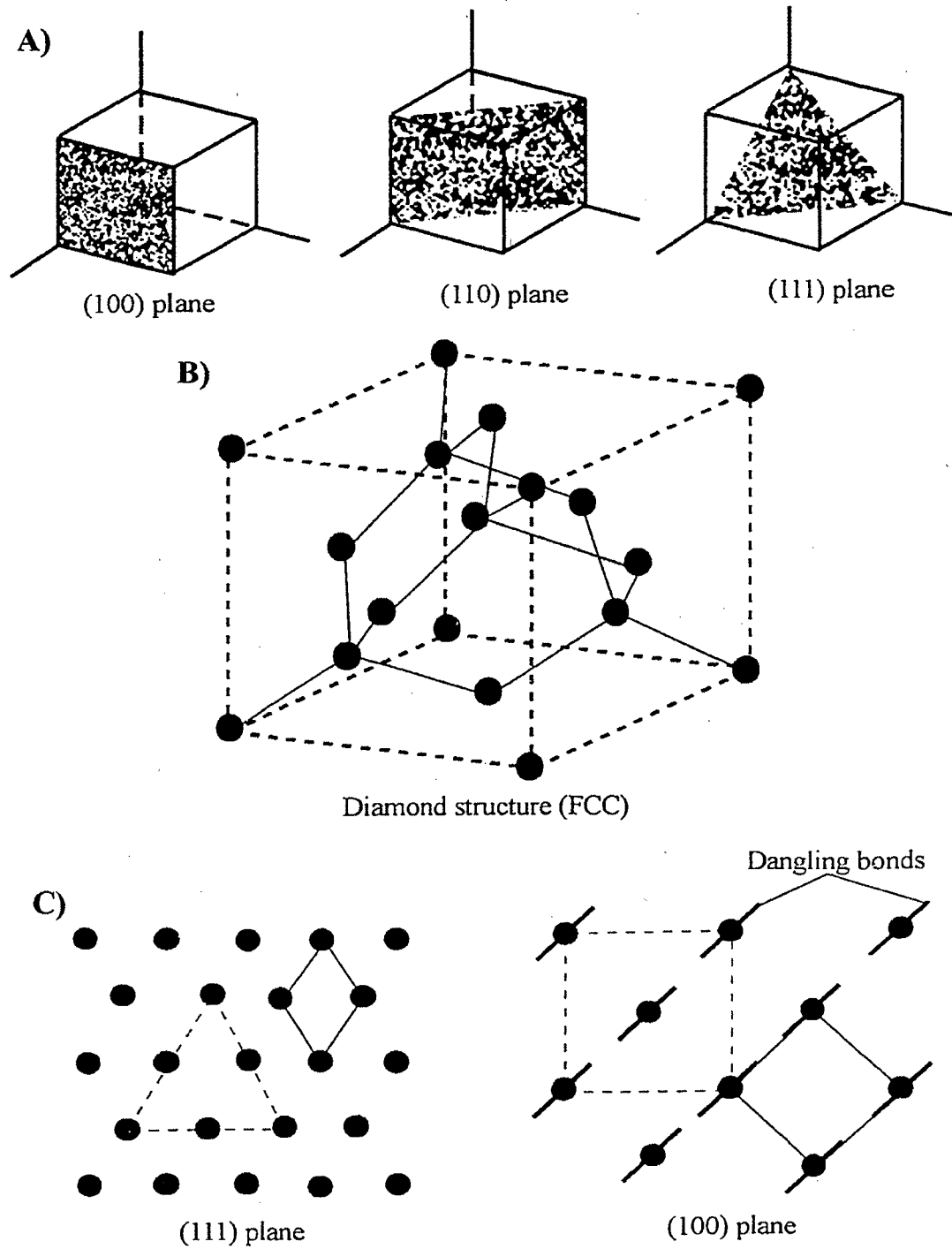
Figure 3.3. A) The Miller indices of three common crystal planes. B) The diamond structure of crystalline silicon. C) The atomic arrangement of atoms for the ideal Si(111) and Si(100) crystal planes. The dashed line represents the plane in reference to the bulk unit cell. The solid line represents the surface unit cell.
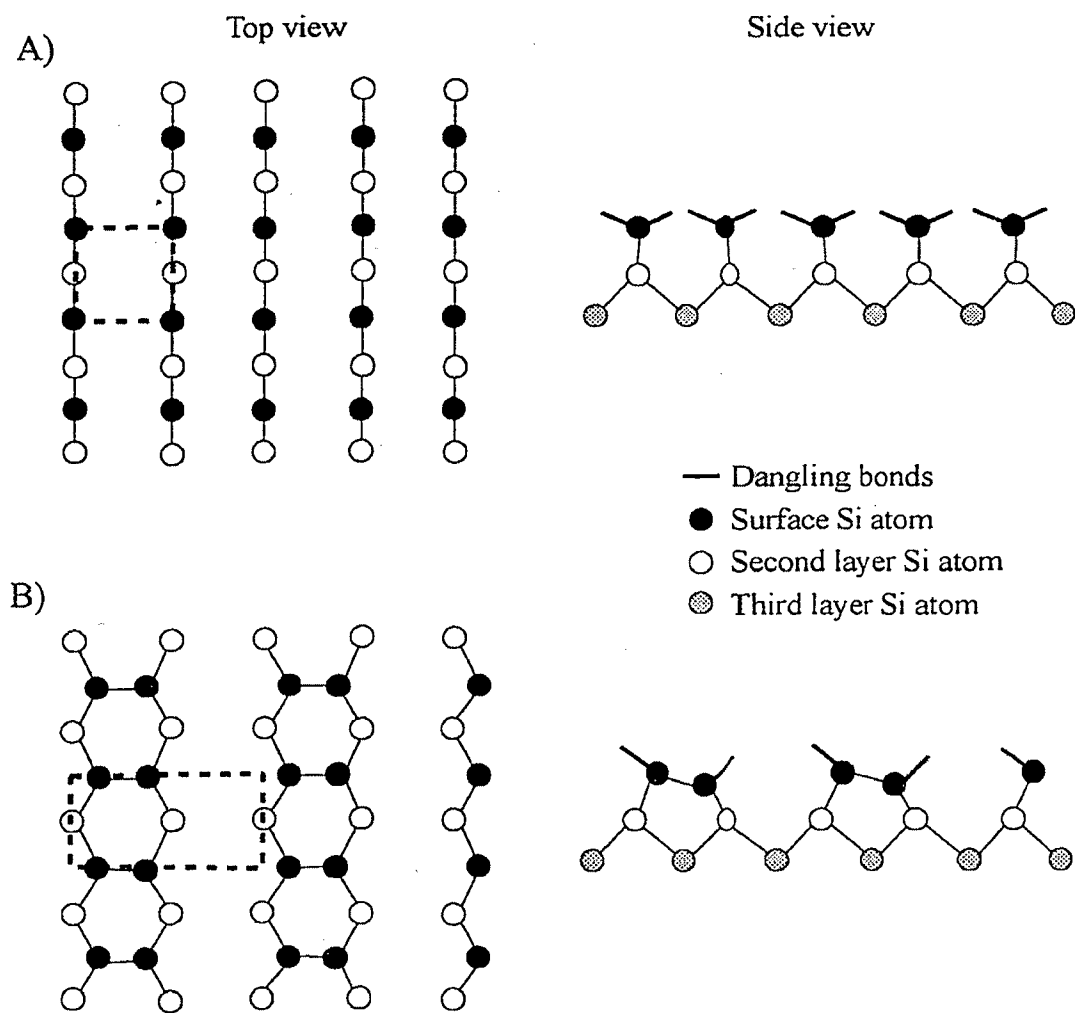
Figure 3.4. Simplified views of the A) unreconstructed (ideal) Si(100) surface, and B) the reconstructed Si(100)-2x1 surface. The dashed line represents the surface unit cell.

covalent solid. Specific crystal planes are defined by a set of numbers (called Miller indices) that specify the coordinates along the unit cell axes where the desired plane crosses these axes. The Miller indices, (hkl) in a cubic system, represent the reciprocals of the coordinates where the plane crosses the unit cell axes (See, Figure 3.3A). For example the (122) plane crosses the unit cell axes at a = 1, b = ½ and c = ½.

Surfaces are formed by cutting the crystal at some plane. At a crystal surface the sp^3 hybrid orbitals directed out of the surface remain unbonded and form so-called, dangling bonds (Figure 3.3C). For the ideal (111) face, one dangling bond per surface Si atom is formed perpendicular to the surface; however, at the (100) face, two bonds per surface Si atom remain dangling. Such surfaces are unstable and reorder themselves, or reconstruct, to decrease the number of dangling bonds and thus, their energy.

In the (100) surface the atoms reconstruct so that opposite rows of atoms move together and form a bond leaving each surface Si atom with only one dangling bond (Figure 3.4). The formation of the dimers on the surface leads to an increase in the size of the surface unit cell by a factor of two in one direction as compared to the unreconstructed surface unit cell. The reconstructed Si(100) surface is thus called the Si(100)-2×1 surface.

Photoemission has proven to be a valuable tool in the elucidation of surface structures. Photoemission looks at the core-level binding energies (See Section 2.3) of the ejected photoelectrons. Any change in the valence electron configuration (through bonding, etc.) modifies the amount of core-charge effectively seen by the core-electrons and thus their binding energies. This is the origin of the chemical shift which is used as a fingerprint of the nature of the environment around an atom. High resolution synchrotron radiation allows the subtle changes (small chemical shifts) to be visible which are not normally visible when using a conventional X-ray source, such as the difference between the up-dimer surface Si atom and the bulk Si atoms.

In a many-electron atom, the coupling of the spin and orbital angular moments (spin-orbit coupling) causes levels with $l > 0$ to no longer be degenerate. Spin orbit coupling causes these energy levels to be split into two levels with $j = l \pm s$ [33]. Thus the

p (l = 1) levels are split into the $p_{3/2}$ and $p_{1/2}$ levels and the f (l = 3) levels are split into the $f_{7/2}$ and $f_{5/2}$ levels. The level with the highest j value is more energetic and has the lowest binding energy. The relative intensity of the two spin orbit split levels reflects the degeneracy ($2j$ + 1) of the spin orbit split levels. As a result, for l > 0 core-levels, each chemically distinct set of atoms gives rise to two photoemission peaks known as a spin-orbit doublet (See Figure 3.5) separated by the spin-orbit splitting. In systems where the spin-orbit splitting is large (as in Au 4f, Δ_{SO} = 3.7 eV), the two doublets can be separated and only one of the components need be considered. In the case where the spin-orbit splitting is small (as in Si 2p, Δ_{SO} = 0.6 eV) the doublets can not always be well separated, adding to the complexity of the subsequent analysis of the photoemission results.

Much debate was centered around the exact structure, both physical and electronic, of the dimer bonds and the subsequent interpretation of the core-level photoemission results. E. Landemark and coworkers, with much improved photoemission resolution and sample preparation, came to the conclusion [34] that the dimer bonding is partially ionic, hence, the surface dimers are asymmetric (Figure 3.4B). The ionic nature implies a small charge transfer from the down-dimer atom to the up-dimer atom. The extra charge on the up-dimer atom decreases the binding energy (relative to a bulk Si atom) of core-electrons escaping from that atom. The loss of charge from the down-dimer atom increases its binding energy. The asymmetric dimer model was originally proposed by D. J. Chadi [35] theoretically.

An example of a well prepared Si 2p core-level photoemission spectrum, taken from our early work on clean and hydrogenated silicon [36], is shown in Figure 3.5 along with a representative fit to the data. Clearly not all the components in the spectrum can be resolved experimentally. Four components other than the bulk peak (**B**) are found necessary to fit the data; these are labelled **S**, **S'**, **SS** and **C** and correspond to emission from the up-dimer atoms, the second layer silicon atoms, the down-dimer atoms and a broad component related to defects, respectively [36]. The binding energy shifts of these components are listed in Table 3.1 and agree with those of E. Landemark et al.. However,
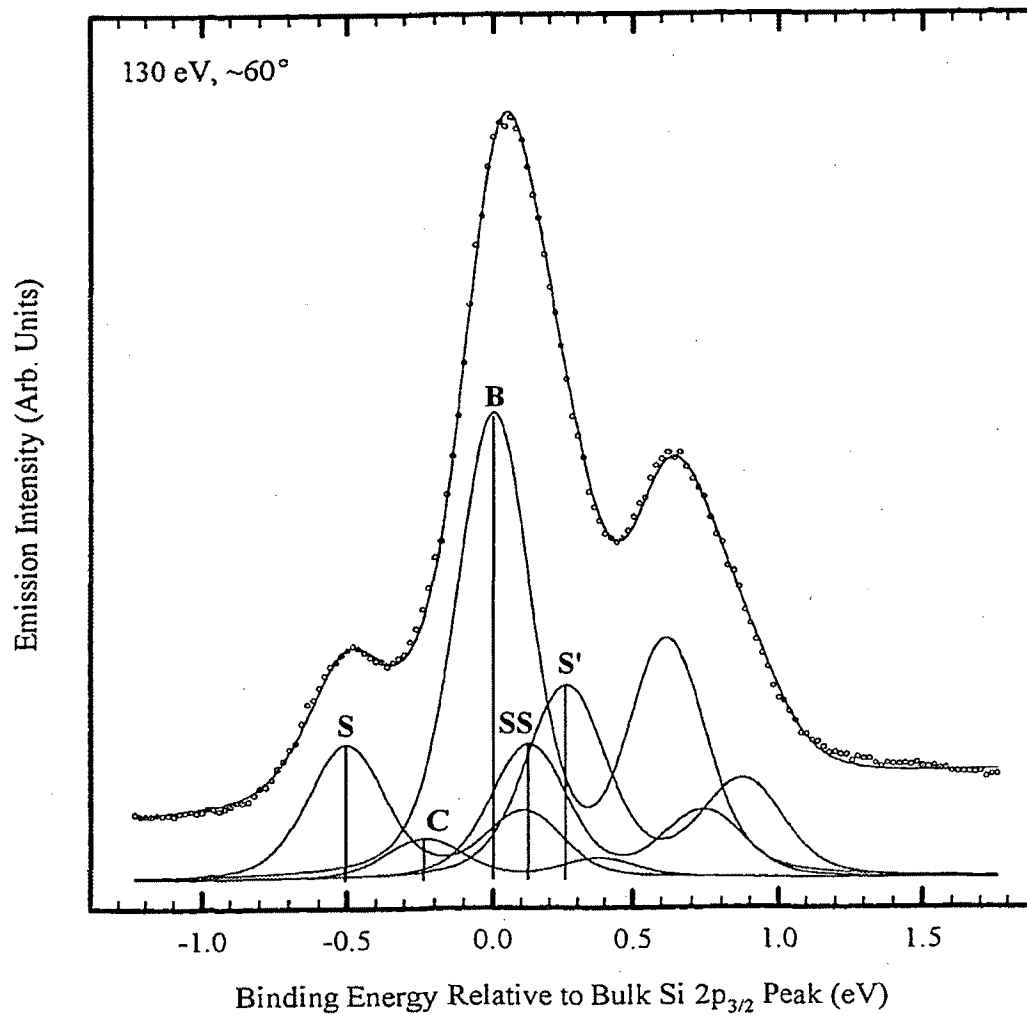
Figure 3.5. Si 2p core-level spectra of a clean Si(100)-2×1 surface and representative fitting components. For description see text. (After D. T. Jiang *et al.* [36])

Table 3.1. Core-level binding energy shifts of the components seen in the Si 2p photoemission spectra of clean silicon. (After D. T. Jiang *et al.* [36])

Component	S	C	SS	S'
ΔE_B relative to bulk* (eV)	-0.50	-0.23	0.12(6)	0.25

*Uncertainty ±0.01 eV except for SS which is as shown.

our interpretation of the origin of the C component differs from that of Landemark.

The surface origin of the four extra components can be verified by changing the emission angle and photon energy in such a way as to increase the escape depth of the electrons as is shown in Figure 3.6. Clearly the relative intensity of the emission from the up-dimer atom (S peak) decreases with increasing escape depth, as do the intensity of SS and S' which is evident from the decrease in intensity between the two spin orbit split components of the bulk doublet.

The surface origin of the S component is also evidenced by its sensitivity to the adsorption of other atoms/molecules on the surface. The S component is seen to disappear from the spectrum by the adsorption of ~½ monolayer of H atoms [36], for example. Thus the presence of the S component in a photoemission spectrum can be used as an indication that a clean silicon surface has been prepared.

The core-level line widths of the photoemission spectra can also be affected by the sample preparation. In order to achieve the narrow lines seen in the preceding Si 2p core-level spectra, the preparation of a sample with low defect density was vital. The effects of poor sample preparation can be seen in Figure 3.7 where we compare spectra taken from the front and back (unpolished) sides of the same sample. Clearly both surfaces are clean and the spectrometer resolution is the same but the spectrum from the back has much broader lines due to the surface non-uniformity (roughness).
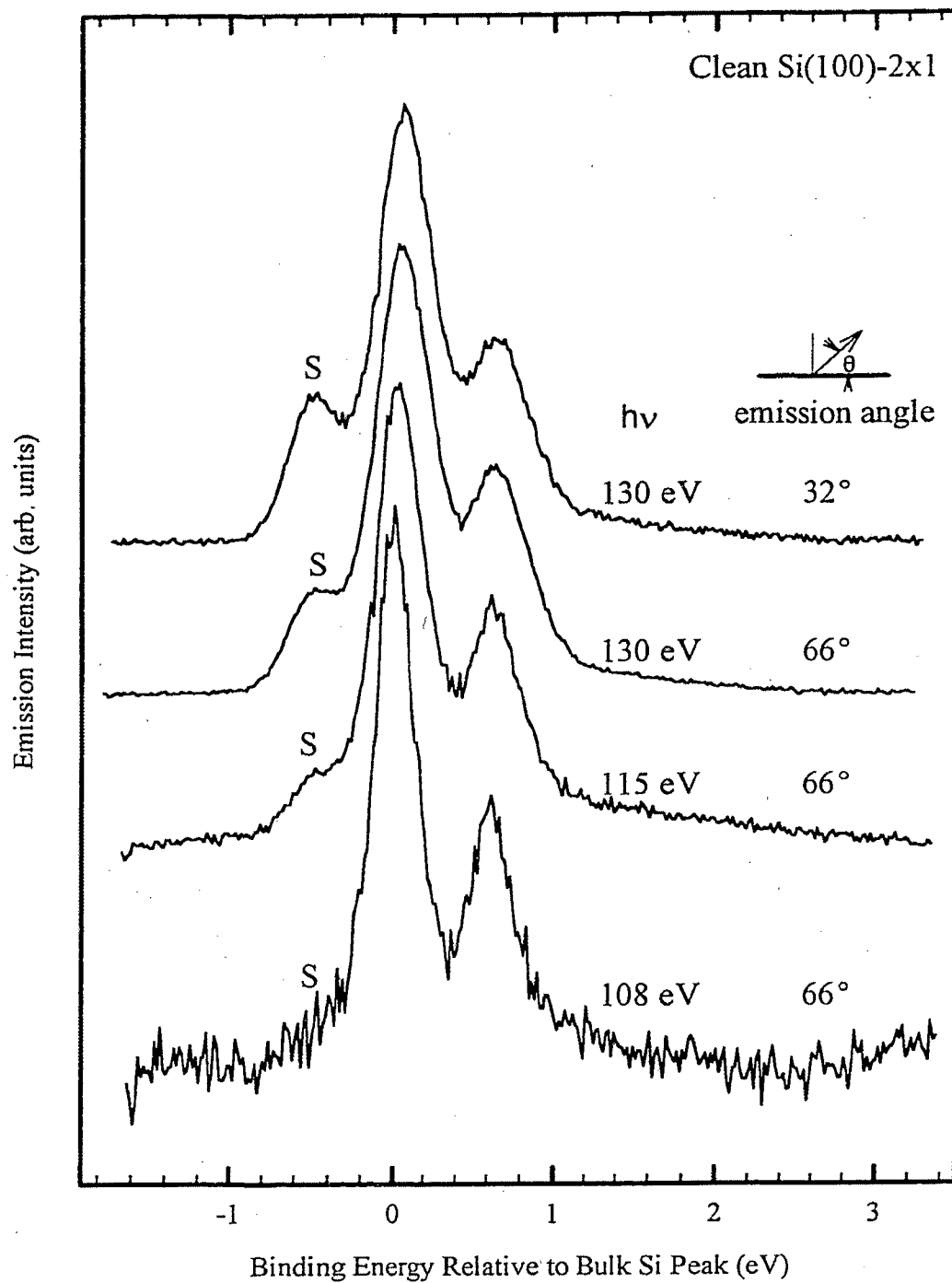
Figure 3.6. Si 2p core-level spectra of the clean Si(100)-2×1 surface. The binding energy zero is defined at the $2p_{3/2}$ peak of the bulk emission. The excitation energies and photoemission angles are labeled. S indicates the up dimer atom emission. (After D. T. Jiang *et al.* [36])
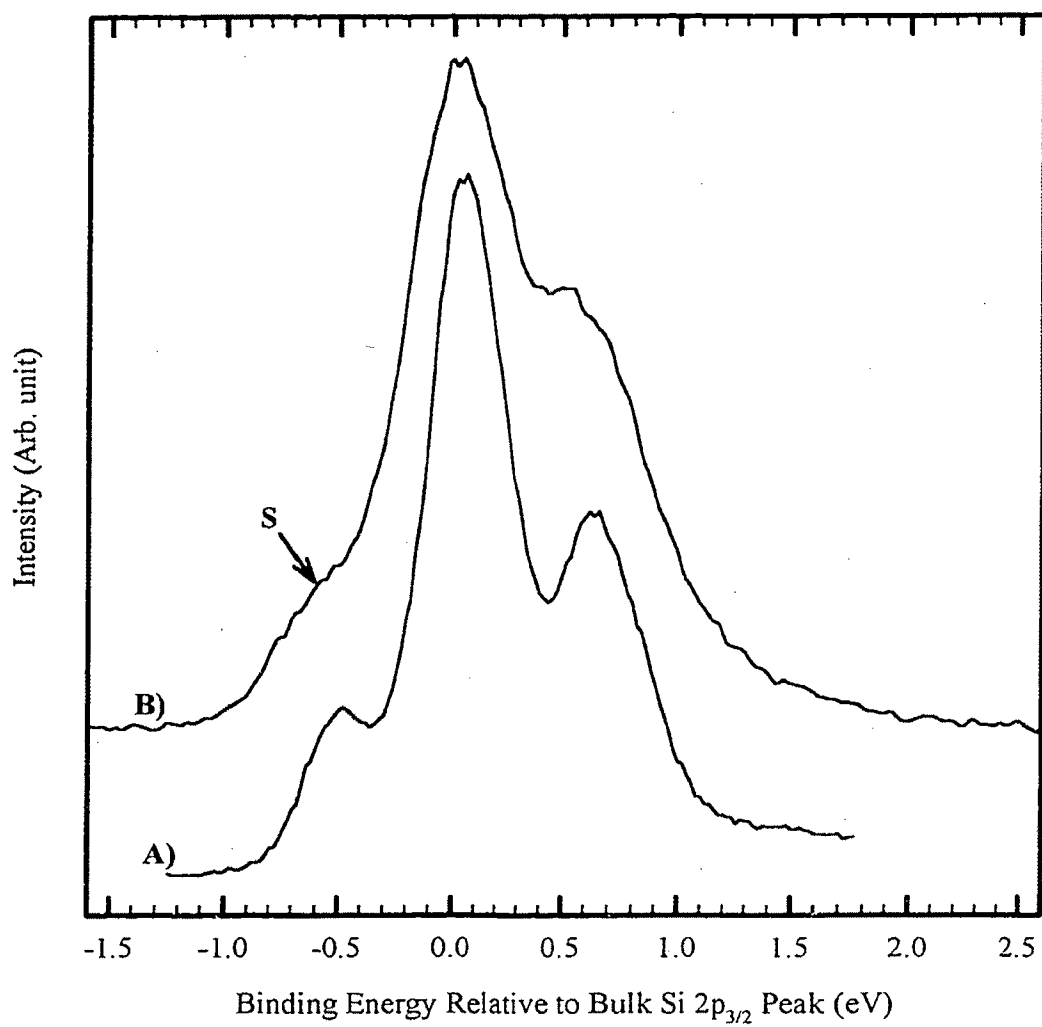
Figure 3.7. Comparison of two Si 2p core-level spectra taken from, A) the front side and B) the back side of, the same sample. S indicates the up dimer atom emission.

3.2 EXPERIMENT

3.2.1 Experimental Equipment

The photoemission experiments were performed on the Grasshopper beamline at the Canadian Synchrotron Radiation Facility (CSRF) located at the Synchrotron Radiation Center (SRC), University of Wisconsin-Madison using an ultrahigh vacuum (UHV) chamber. The experimental chamber was equipped with a Leybold $180°$ hemi-spherical electron energy analyser, a 4-axis manipulator, a Au evaporation source (Figure 3.8), and was pumped by an ion/sublimation pump combination. The base vacuum in the experimental chamber was 1×10^{-10} torr. A 1800 groove/mm grating was used in the grasshopper and provided optimal resolution (~ 0.2 eV) at about 130 eV photon energy, with a 12.5 eV analyser pass energy.

Au was evaporated from a heated tungsten filament held 5-6 cm from the Si sample. The dosing was carried out with the Si(100) substrate at room temperature and no detectable increase in substrate temperature was observed during dosing. The pressure in the chamber during dosing was kept below 5×10^{-9} torr. The coverage of Au adsorbed on the Si(100) surface at the end of a series of experiments was determined by Rutherford Backscattering (RBS). Intermediate coverages were then determined using the accumulated dosing times. The photoemission spectra were taken from two samples. For each sample, the current in the Au doser during evaporation was kept constant but was varied between samples. The dosing rates were approximately 0.18 ML/min and 5 ML/min for the two experimental runs.

The Rutherford Backscattering (RBS) experiments were preformed at the van de Graaff accelerator laboratory located at the University of Western Ontario. The coverage of Au was measured using a 1 MeV ^{4}He$^+$ beam. The backscattered He particles were counted by a Si surface-barrier detector located at a scattering angle of about $150°$. A Bi-implanted standard sample was used to calibrate the coverage measurements with a precision of 3%. An example of a typical RBS spectrum for the Au covered Si(100)

TOP VIEW

Photon Port

Leybold Hemispherical
Analyzer

Au Doser

SIDE VIEW

Sample
Manipulator

Manipulator
Shaft

Au Doser

Photon Port

TNBX Pumping System

Copper rods on manipulator shaft (x, y, z, φ)

Copper blocks

Stainless Steel screws

Ceramic spacers

Mo Supports

Thermocouple wires

Ta clips

Stainless Steel set screws

Si sample (6mm × 20mm)
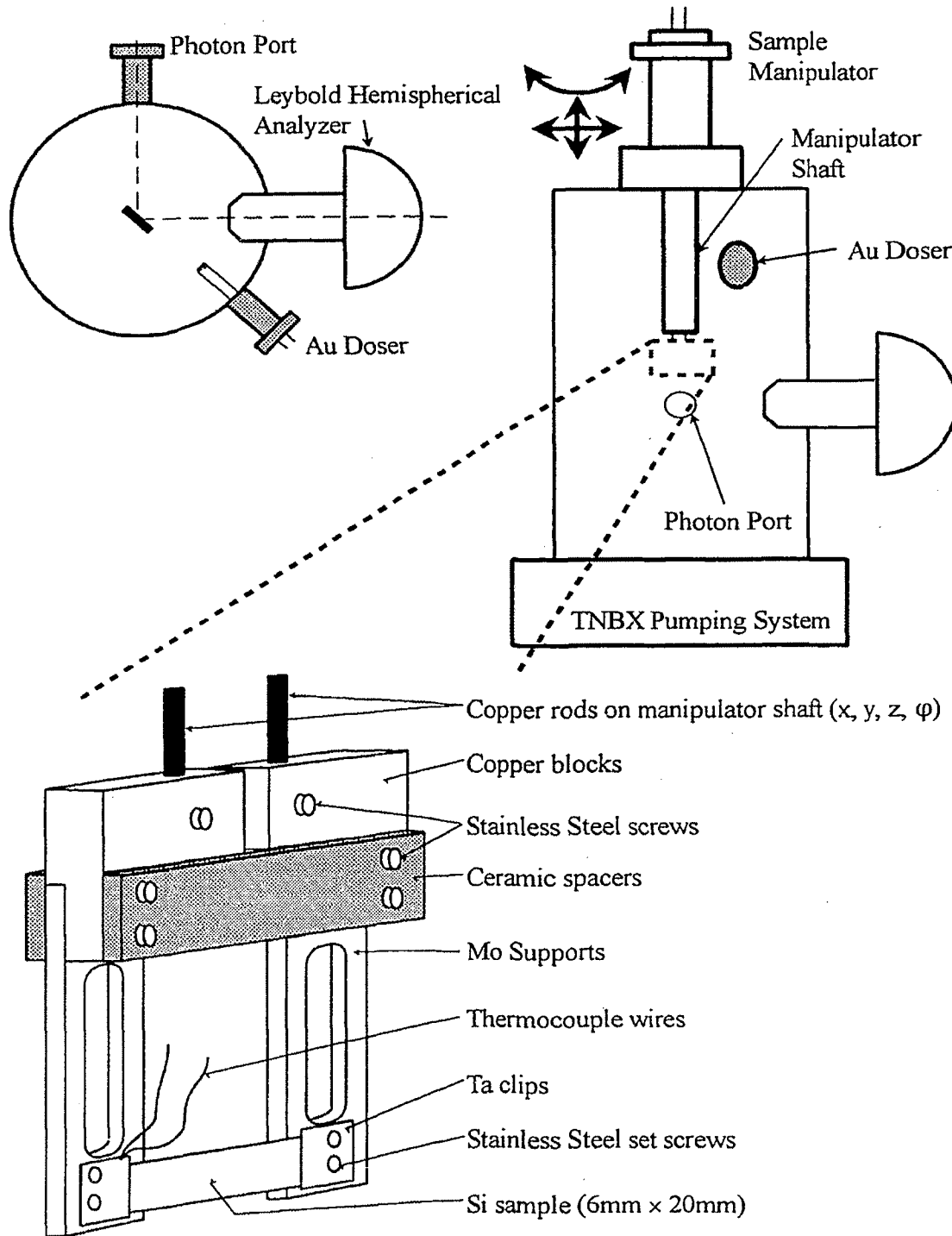
Figure 3.8. Schematic diagram of the PES experimental chamber, the important analytical
devices and the sample mount used to study the Au/Si(100) system.
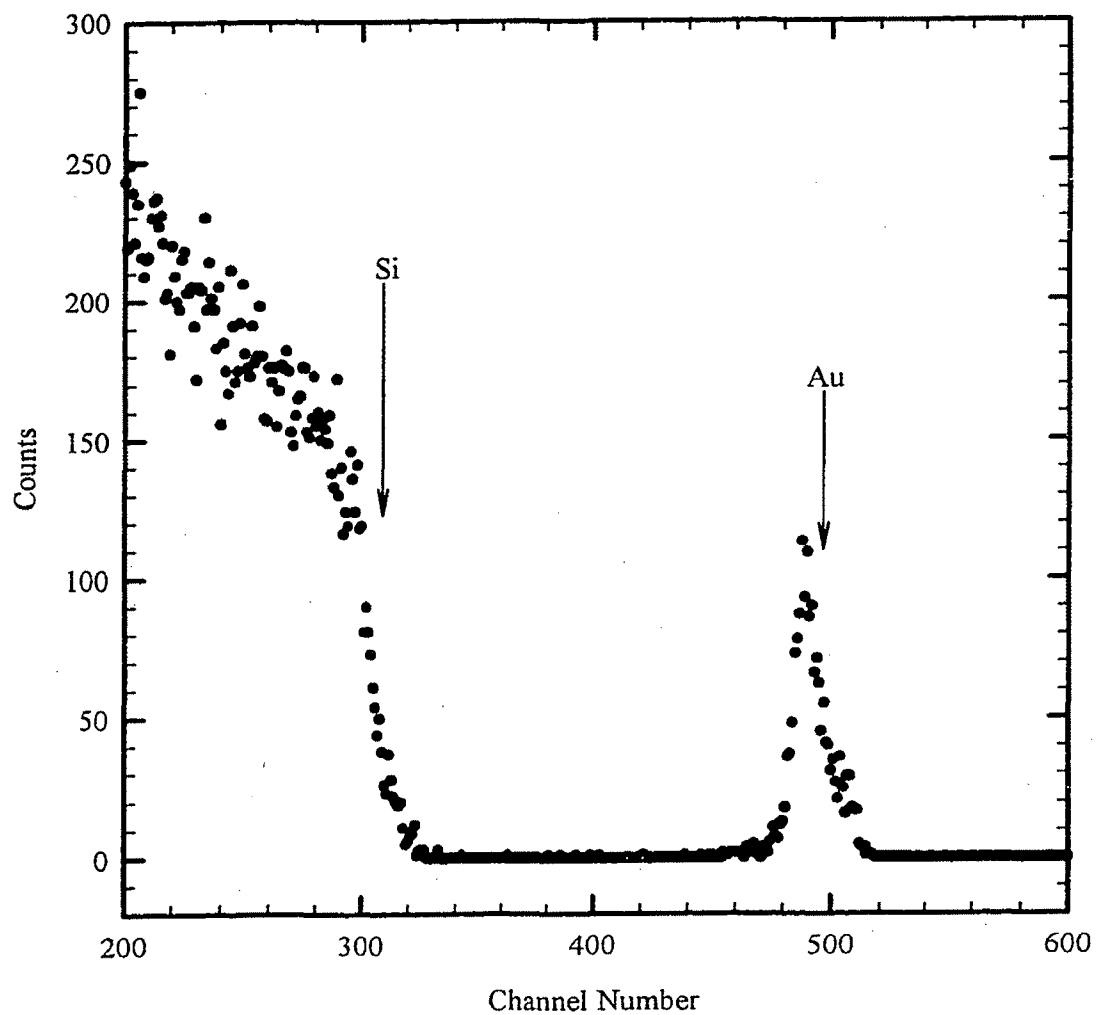
Figure 3.9. 1 MeV He$^+$ Rutherford Backscattering Spectrum of the 3.6 ML Au covered Si(100) wafer.

samples is shown in Figure 3.9. The area under the Au peak is used to determine the coverage in atoms/cm^2. The coverages are then converted to coverages in monolayers (ML). A monolayer is the number of atoms/cm^2 present on a clean surface, for Si(100) 1 ML = 6.78×10^{14} atoms/cm^2.

3.2.2 Sample Preparation

Si (100) samples of about 6mm × 20mm size were cut from an n-type (4-7 Ω cm) wafer and mounted in a tantalum/molybdenum holder (see Figure 3.8) mounted at the end of the sample manipulator in the vacuum chamber. The samples were heated resistively and the temperature was measured by an IR pyrometer (for the high temperature used in cleaning) and by a K-type (Chromel®/Alumel®) thermocouple spot welded on the tantalum holder at lower temperatures.

The Si(100) samples were first degassed at ~600°C for a minimum of 4 hours keeping the chamber pressure in the 10^{-10} torr range. After degassing, the samples were cleaned by flashing to 1100 °C for 30 sec., followed by rapid cooling to below 800 °C then slow (15 - 20 min.) cooling to room temperature. Several flashing and cooling cycles were required to achieve a clean surface initially. The pressure during cleaning was held in the 10^{-9} torr range. Ideally the pressure throughout the degassing and cleaning procedure should be maintained in the 10^{-10} torr range.

When the preparation conditions are optimized, this cleaning procedure is expected to produce a defect density of <5% [37]. Although this cleaning procedure can produce clean surfaces with low defect density (such as the sample whose Si 2p core-level photoemission spectrum is shown in Figure 3.5) it is very difficult to control, and any deviation from ideal conditions can leave a dirty, a visibly rough surface or a surface with a high defect density. The Si(100) surfaces prepared for Au deposition appeared to be clean and were visually smooth but had broad photoemission (Figure 3.10) lines (similar to the back-side spectrum shown in Figure 3.7B) indicating that the prepared surfaces were not atomically smooth.

3.3   RESULTS AND DISCUSSION

3.3.1   Si 2p Core-level Data

Looking first at the spectra taken at 130 eV photon energy. At this photon energy the kinetic energy of the ejected 2p core electrons is approximately 30 eV, which is within the broad minimum in the universal curve of electron escape depths (~5Å, Figure 2.7). The spectra taken at 130 eV are thus surface sensitive. Figure 3.10 shows the spectra obtained from dosing successive amounts of Au onto the Si(100) surface.

The Au coverages as determined by RBS and dosing times are indicated in the figure. The coverages up to and including 3.6 ML are from the sample dosed at a rate of 0.18 ML/min.. Coverages above 3.6 ML (12.8 ML and 25.5 ML) are from a second sample which was dosed at ~5 ML/min.. The spectra shown have been normalized to the point of maximum intensity in the spectra.

The binding energy scale is as recorded experimentally. The expected binding energy of the Si $2p_{3/2}$ peak of bulk silicon is 99.2 eV; we observe the $2p_{3/2}$ bulk peak at approximately 103.5 eV. This discrepancy (4.3 eV) is caused by the spectrometer and sample work functions which have not been calibrated for in the experimental setup.

The peak corresponding to the $2p_{3/2}$ component of the up-dimer atom emission in the clean Si spectrum is indicated by an arrow labelled S in the figure.

A number of observations from these spectra are apparent:

1)   The emission from the up-dimer atom S deceases in intensity with increased gold coverage and is almost completely gone by 0.36 ML.

2)   There is little change apparent in the rest of the spectra for the low coverages except for a small broadening of the peaks towards the higher binding energy side.

3)   The spectrum obtained at 3.6 ML coverage is significantly different from the preceding spectra taken at sub-monolayer coverages. Two components are clearly seen at higher and lower binding energies than in the previous spectra.

4)   The lower binding energy component in the 3.6 ML Au covered spectrum
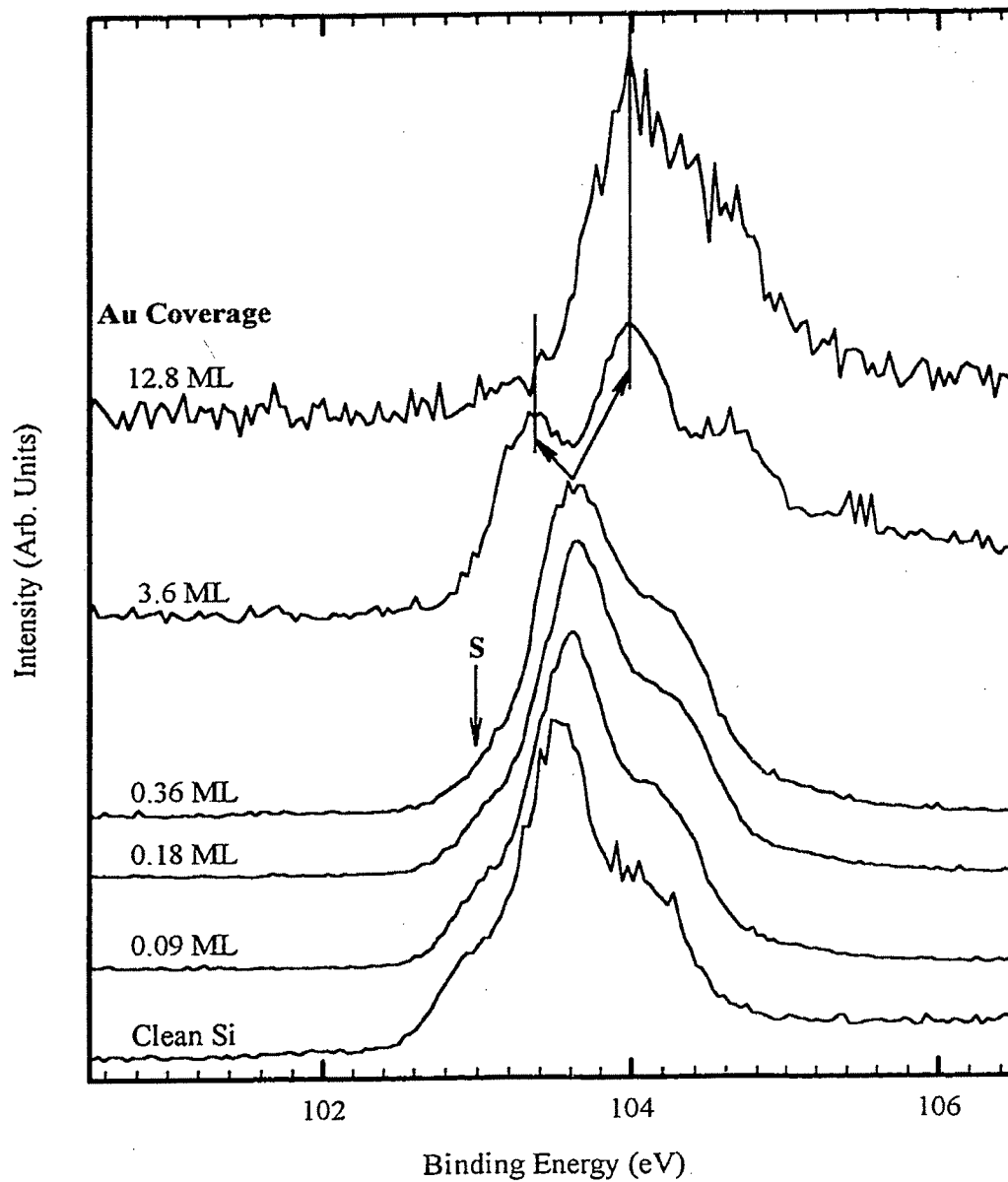
Figure 3.10. Si 2p core-level spectra of clean Si(100) and Au covered Si(100) taken at a photon energy of 130 eV. The Au coverages are indicated in the figure. The surface component (S) corresponding to the up dimer atoms is indicated by an arrow.

disappeared with an increase in the Au coverage, while the higher binding energy component remained.

The rapid decrease in the intensity of the surface component is hardly surprising as this is seen in other systems of adsorbates on Si, including H [36]. Because the sampling depth at this photon energy is only about 5 Å, it is possible that physisorbed Au overlayers could attenuate the signal and thus decrease the relative intensity of the S peak without modifying the surface. This is unlikely as attenuation of S should also decrease the relative intensity of SS and thus decrease the intensity in the valley between the spin orbit components of the main (bulk) peak (as was seen in Figure 3.6). Such a decrease clearly does not happen and indicates that the Au atoms react with the dimer atoms to form some surface Au silicide. The formation of a surface Au silicide would be expected to produce an increase in intensity somewhere else in the spectra corresponding to the emergence of a photoemission doublet characteristic of the silicide or alloy formed. Such a change is not immediately evident from the sub-monolayer Au covered spectra. The valley between the two main peaks is however partially filled in with the broadening of the peaks in the Au covered spectra and a shift of the main peak to higher binding energy. This broadening may be evidence of the expected Au silicide photoemission.

By 3.6 ML of deposited Au, the spectrum develops into two clearly defined components to either side of the original Si bulk peak position. It has been established on both Si(100) and Si(111) surfaces that the lower binding energy component corresponds to bulk unreacted silicon which has been shifted towards E_F by band bending [19][28][30][38]. The band bending shift is approximately 0.17 eV close to the low end of the reported range of 0.2 eV [28] to 0.43 eV [38]. The assignment of the lower binding energy component to bulk silicon is supported by the fact that at higher gold coverages, this component vanishes in favour of the higher binding energy component [19][38], as can be seen in the top spectrum in Figure 3.10 (12.8 ML). At higher Au coverages (12.8 ML) the bulk silicon atoms are too deeply buried for emitted photoelectrons to escape.

The higher binding energy component seen in the 3.6 ML spectrum is attributed to

a Au silicon compound. This peak is shifted by approximately 0.7 eV to higher binding energy from the bulk silicon peak and persists even at high Au coverages. This is evidence that a silicide is always present at the surface and that it originates early in the formation of the Au-Si interface.

Moving now to the spectra obtained at 160 eV photon energy (Figure 3.11). At this excitation energy, the photoelectrons have a slightly longer escape depth (by about 2-3 Å); this makes these spectra slightly more bulk sensitive than the spectra taken at 130 eV. This means that any surface peak should decrease in intensity relative to the bulk while any peak that originates from deeper in the sample should increase in intensity relative to the bulk.

The spectra shown in Figure 3.11 have been treated in the same manner as the 130 eV data in Figure 3.10. The resolution of the spectra decreases slightly with the photon energy. The surface component (S) in the clean Si(100) spectrum is clearly reduced in intensity relative to the bulk as compared to the 130 eV spectra. This is expected since the 130 eV spectra are more surface sensitive.

In the 160 eV spectra the increase in the intensity in the valley between the bulk Si 2p components is much clearer than in the 130 eV data. This is evidence for a component, shifted roughly 0.25 eV to higher binding energy from the bulk, which increases in intensity with increased gold coverage. The approximate position of this Au silicide peak is shown in Figure 3.11 with an arrow labelled "Au-Si A". The silicide peak at higher coverages, shifted by approximately 0.7 eV to higher binding energy, is labelled "Au-Si B" in the figure.

Besides the slight intensity variations noted above, the main features of the spectra are identical to those found for the 130 eV data. The picture of the Au-Si interface formation that emerges is:

1) Initial reaction of deposited Au with Si surface atoms begins immediately; no critical coverage needs to be achieved before the reaction. The loss of the surface silicide component (S) and the development of the "Au-Si A" component at higher binding energies are both clearly seen by 0.36 ML of Au coverage.
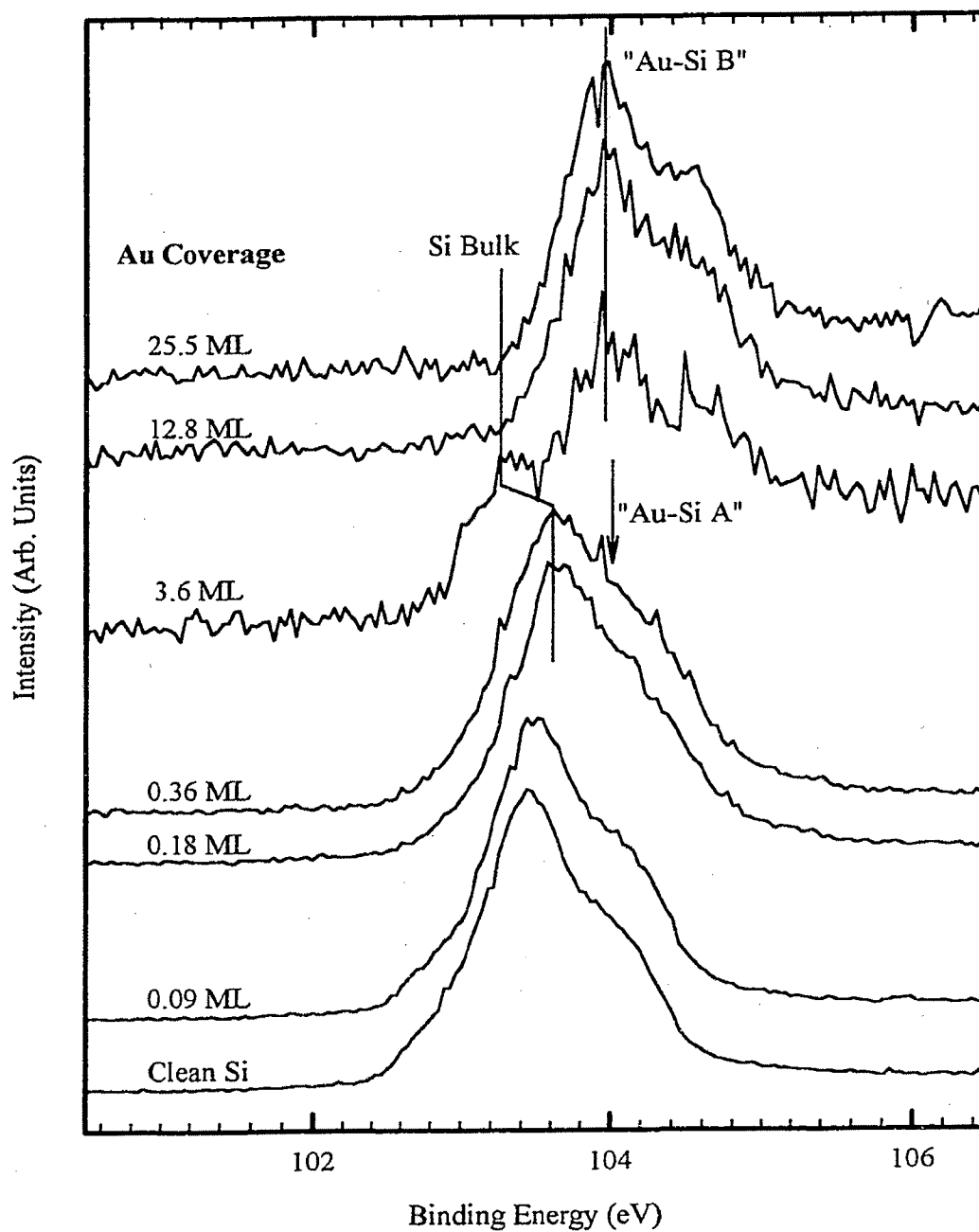
Figure 3.11. Si 2p core-level spectra of clean Si(100) and Au covered Si(100) taken at a photon energy of 160 eV. The Au coverages are indicated in the figure along with the bulk Si signal position and the positions of the two Au-Si "alloy" peaks.

2) At higher coverages, band bending shifts the bulk Si 2p component towards the Fermi level. This is accompanied by the development of the "Au-Si B" component shifted to higher binding energy relative to bulk Si but by a larger amount than "Au-Si A".

3) As more Au is deposited the bulk Si signal disappears leaving only the "Au-Si B" component.

The fact that the low coverage silicide (A) is more evident in the bulk sensitive 160 eV data suggests that the initial silicide is formed somewhat below the surface. This seems reasonable as the silicide is formed under a layer of deposited Au.

The data and description of the Au-Si interface formation described above are consistent with those seen in the formation of the Au-Si(111) interface [19][38] at room temperature, although in these two previous studies no evidence was found for a low coverage silicide. K. Hricovini et al. [28] found that in the Au/Si(100) interface, only one silicide was formed (with a chemical shift of approximately 0.6 eV) from 0.3 ML to over 1 ML of Au coverage.

The core-level shift of the "Au-Si B" component seen at high gold coverages is consistent with those reported on the Si(111) surface [19][38] and on the Au/Si(100)-5×1 surface [30] and has been previously identified as arising from Au_3Si.

The photoemission peaks from both silicides formed exhibit positive binding energy shifts which indicate that Si loses charge in both silicides. The increase in the shift is indicative of each silicon being associated with more Au atoms in the second silicide (B) compared to the first (A). Even though Au is more electronegative than silicon, it is hard to suggest that gold would have a significant negative charge in a compound; thus some charge compensation is expected to exist in both these compounds.

3.3.2 Difference Spectra

Thus far in the discussion we have identified the "Au-Si A" compound in the sub-monolayer coverage range as having a chemical shift of approximately 0.25 eV. The
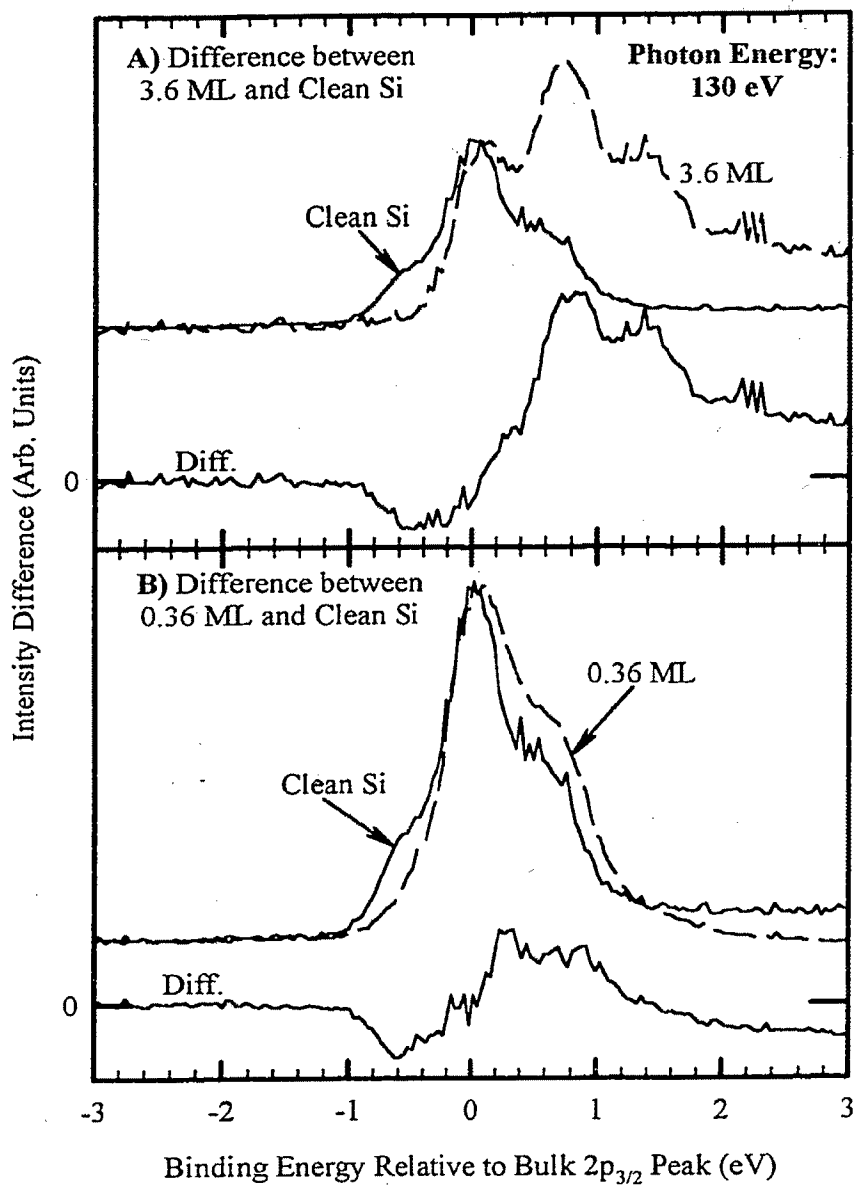
Figure 3.12. Difference between A) 3.6 ML and B) 0.36 ML Au covered and clean Si(100) spectra. The Au covered spectra were shifted so that the bulk peaks were approximately aligned. The core-level spectra were also normalized to the height of the bulk peak.

chemical shift was determined by the filling of the valley between the bulk Si $2p_{3/2}$ and $2p_{1/2}$ components, which has a chemical shift between 0.2 and 0.4 eV. An accurate chemical shift of this component is difficult to determine from the sub-monolayer spectra. Fitting of the spectra with Voigt lineshapes (convolution of a Gaussian and Lorentzian line) using a non-linear least squares fitting program was attempted; however, with the 6 required components, the fits were not unambiguous.

A simpler method to determine the chemical shifts with greater accuracy is by using difference spectra. By taking the clean Si(100) spectrum and subtracting it from a Au covered spectrum, the difference between the spectra can be seen. The differences seen arise from the changes in intensity of the various components affected by the Au adsorption. Such difference spectra are shown, in Figure 3.12, for data collected at a photon energy of 130 eV. The (0.36 ML - clean) and (3.6 ML - clean) cases are shown. In both cases the Au covered spectra have been shifted and scaled to the position and intensity of the bulk $2p_{3/2}$ component in the clean Si spectrum.

The difference spectrum between 0.36 ML Au-covered spectrum and the clean Si(100) spectrum (Figure 3.12B) shows first, a negative peak with a binding energy shift of approximately -0.6 eV, followed by a positive doublet with an approximate separation of 0.6 eV corresponding to the spin-orbit splitting seen in Si 2p levels. The first peak is caused by the decrease in intensity of the $2p_{3/2}$ part of the S (up-dimer surface atom) component of the clean spectrum. The second doublet clearly indicates the growth of a Au-Si doublet in the spectrum at higher binding energies. The $2p_{3/2}$ part of the Au-Si doublet is distorted because of interference from the decrease in intensity of the $2p_{1/2}$ part of the S component. The relative binding energy of the $2p_{1/2}$ part of the doublet is 0.8 eV. Subtracting the spin-orbit coupling value of 0.6 eV leaves an approximate chemical shift of 0.2 eV.

Analysis of the difference spectrum between the 3.6 ML Au covered spectrum and the clean Si spectrum gives the same features except that the Au-Si compound component has a chemical shift of 0.7 eV. This simple analysis clearly illustrates the presence of the "Au-Si A" component, with a chemical shift of 0.2 eV, in the sub-monolayer Au-covered

spectra and the dramatic coverage dependent change in the chemical shift to 0.7 eV, "Au-Si B".

The 3.6 ML Au covered spectrum was analysed using-least squares fitting procedure (shown in Figure 3.14B). Doniach-Sunjic (asymmetric Lorentzian) [39] lineshapes convoluted with Gaussian lineshapes were used. The asymmetry parameter (α) found was small (< 0.1); thus the components are almost symmetrical. If $\alpha=0$ the D-S lineshape used reduces to a Voigt lineshape. The asymmetry arises from many-body metallic screening of the core-hole [39][40]. In silicon, with no electron density at the Fermi level, no asymmetry is required in the fitting lineshapes [34][36]. The presence of a small asymmetry in the peaks suggests that the silicide "Au-Si B" is metallic. The spectrum is fitted with two doublets (spin-orbit splitting of 0.602 eV) with a separation of 0.70 eV consistent with previous results [19][30] and the difference spectra analysis above.

In the analysis of the Si 2p core-level data the presence of the other known surface related components (SS, S') have been ignored because there is not enough information in the spectra recorded to determine exactly the changes in intensity or positions occurring with these peaks. Higher resolution and more detailed fitting in the sub-monolayer coverage region, based on the known clean Si(100) components (Figure 3.5), may reveal whether Au adsorbs simultaneously on both surface dimer atoms, or whether the adsorption process is sequential, as is the case for H atoms adsorbed on Si(100) [36].

3.3.3 Au 4f Core-level Data

Au 4f core-level data were taken simultaneously with the Si 2p data. Au core-levels were only seen for the 3.6 ML Au coverage and above. The Au 4f core-level spectra are shown in Figure 3.13 and representative fits of two of the 160 eV data are shown in Figure 3.14a. As for the Si 2p data the binding energies are as recorded and show a 4.3 eV shift due to the spectrometer work function.

As the Au coverage is increased, the Au 4f doublet appears to shift to lower
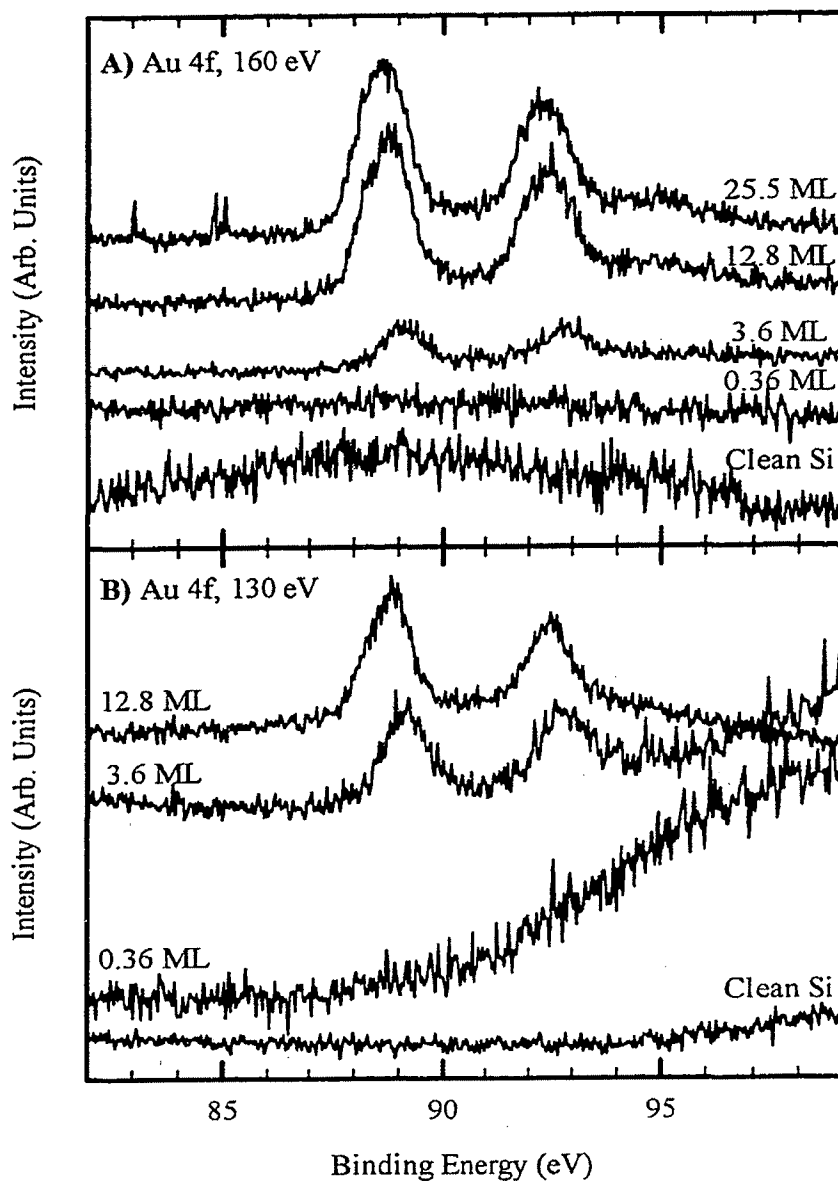
Figure 3.13. Au 4f core-level spectra of clean and Au covered Si(100) taken at a photon energy of, A) 160 eV and B) 130 eV. The Au coverages are indicated in the figure.
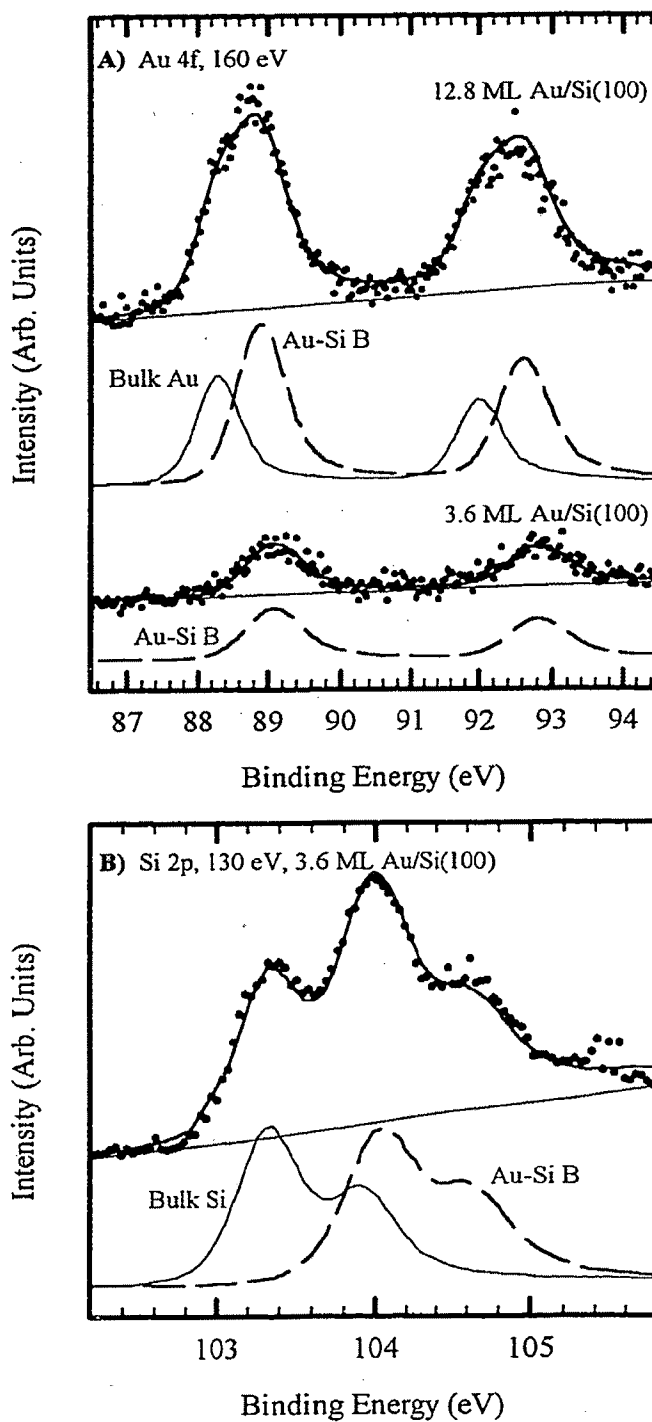
Figure 3.14. Representative fits to the core-level data. A) Au 4f data taken at 160 eV, B) Si 2p data taken at 130 eV. Dots corespond to the data, the thick solid line is the fitted spectrum, components are labeled.

binding energy while broadening to the lower binding energy side. The shift in the Au 4f levels towards E_F was first seen by L. Braicovich *et al.* [32]. The 3.6 ML spectrum can be fitted with one doublet (spin-orbit splitting 3.7 eV) at 89.0 eV. The higher coverage spectra require two doublets, one at 88.85 eV consistent with the doublet found at 3.6 ML coverage within experimental error, and one shifted to lower binding energy by 0.6 eV to 88.25 eV. These results are consistent with others on both the Si(100) [30] and the Si(111) surfaces [19][38]. The lower binding energy component has been identified as arising from the forming Au layer since it increases with increasing Au coverage and because its position matches that for pure Au. The higher binding energy doublet is identified with the surface silicide "Au-Si B". It should be noted that this doublet never disappears from the spectrum regardless of Au coverage indicating that some silicide remains on the surface [19] even at high Au coverages.

It is interesting to note that for similar coverages on the Si(111) surface, J.-J. Yeh *et al.* [19] find that the bulk Au peak is more intense than the silicide peak while in our spectra the situation is reversed. This suggests that for a similar coverage, the thickness of the surface silicide formed is larger in our samples. Whether this is due to differences between Si(100) and Si(111) or just our sample preparation is unclear.

The positive binding energy shift of the Au silicide Au 4f peaks suggests that Au loses charge. This seems to contradict the Si 2p results that had Si losing charge as well. This effect is common in Au compounds [41] and is consistent with the charge compensation model. The charge compensation model [42] states that Au gains sp-type charge but loses d-charge to compensate, causing a small net charge flow onto the Au site. This allows Au to satisfy both electronegativity and electroneutrality considerations. The Au 4f binding energy shift is positive since the shift depends not only on the charge transferred but also on the screening ability of the charge. Since the d-electrons screen the nucleus better than sp-electrons a small loss of d-charge dominates the binding energy shifts.

3.4 CONCLUSIONS

In this portion of the project, the bottom-up approach to the investigation of the interactions of metals with Si(100) was used to study the initial stages of the formation of the Au/Si(100) interface. The interface was studied using core-level photoemission spectroscopy using synchrotron radiation.

It was found that the Au/Si interaction is immediate, with a decrease in Si surface state intensity and an accompanying increase in intensity of a Au-Si phase (Au-Si A). As the Au coverage increases, the Au-Si phase shifts relative to the bulk Si (Au-Si A → Au-Si B transition) and at the same time the Si bulk state is shifted towards the Fermi level by band bending effects. The second silicide formed persists as the Au coverage increases, while the bulk silicon signal decreases until it eventually disappears from the spectrum as the sampling depth of PES is exceeded by the thickness of the Au overlayers. The loss of the Si 2p bulk signal in the Si 2p core-level spectra is accompanied by the increase of a pure Au doublet feature in the Au 4f spectra. The Au 4f doublet arising from the silicide persists through out the Au coverage series up to high Au (25 ML and above) coverages, indicating that the Au layer forms between the top silicide and the interface. The chemical shifts of the Au 4f and Si 2p core levels for the high coverage silicide (Au-Si B) indicate that the charge transfer in the silicide follows the charge compensation model for Au bimetallics. No Au 4f peak was observed for the low coverage silicide. The picture of the interface formation described above is similar to that seen for the Si(111) and Si(100) surface; however, the immediate reaction and presence at low coverages of a Au-Si peak with a different chemical shift from the final Au-Si peak has not been reported before.

Several questions remain:

1) Whether the development of the band bending is abrupt or gradual. Along with this is the question of when the surface changes from semiconducting to metallic and the progress of the development of the Schottky barrier.

2) Whether the Au-Si compounds are alloys or stoichiometric compounds. If the transition from one chemical shift to the other is gradual, then alloys are formed.

3) Whether the first Au silicide remains at the Au-Si interface, or the second Au silicide remains at the interface or if the interface becomes atomically abrupt as the Au layer forms between it and the top silicide. This is difficult to answer using photoemission as the overlayers prevent the probing of the interface. Perhaps XANES can sample the interface through the overlayers to answer this question.

4) The exact positions of the atoms at the interface and composition of the first Au silicide formed up to a few ML; this information is increasingly important to control interfacial structures in ultrathin films.

5) Whether the discrepancies with previous Au/Si(100) core-level data are due to differences in surface preparation, Au dosing rates or other factors.

Overall the bottom-up approach of following the evolution of the Au/Si(100) interface has solved some questions but much more work is required, in photoemission and other techniques, to answer the remaining questions as this project continues.

3.5 REFERENCES

[1] H. von Känel, Mat. Sci. Rep. **8**, 193 (1992), and references therein.

[2] F. Comin, J. E. Rowe and P. H. Citrin, Phys. Rev. Lett. **51**, 2402 (1984).

[3] J. van Luenen, J. W. M. Frenken and J. F. van der Veen, Appl. Phys. Lett. **45**, 41 (1984).

[4] A. Cros and P. Muret, Mat. Sci. Rep. 8, 271 (1992).

[5] *Binary Alloy Phase Diagrams*, eds. T. B. Massalski, J. L. Murray, L. H. Bennett and H. Baker (American Society for Metals, Metals Park, 1986), pg. 313.

[6] For reviews of Au/Si systems see; a) G. Le Lay, Surf. Sci. **132**, 169 (1983), b) A. Hiraki, Surf. Sci. Rep. **3**, 357 (1984), c) C. Calcandra, O. Bisi and G. Ottaviani, Surf. Sci. Rep. **4**, 516 (1984) and d) A. Cros and P. Muret, Mat. Sci. Rep. **8**, 271 (1992).

[7] H. E. Bishop and J. C. Rivière, J. Phys. D **2**, 1635 (1969).

[8] A. Hiraki, F. Lugujjo and J. W. Mayer, J. Appl. Phys. **43**, 3643 (1972).

[9] J. S. Song and C. A. Chang, IBM Rept. RC 12136 (1986).

[10] A. Cros, F. Salvan and J. Derrien, J. Appl. Phys. **52**, 4757 (1981).

[11] L. Hultman, A. Robertson, H. T. G. Hentzell, I. Engström and P. A. Psaras, J. Appl. Phys. **62**, 3647 (1987), and references therein.

[12] See for example, R. F. Wolffenbuttel, Sensors and Actuators A **62**, 680 (1997), and references therein.

[13] B. Lamontagne, E. Sacher and M. R. Wertheimer, Appl. Surf. Sci. **78**, 399 (1994).

[14] C. Grupp and A. Taleb-Ibrahimi, Phys. Rev. B **57**, 6258 (1998).

[15] Z. H. Lu, T. K. Sham and P. R. Norton, Appl. Phys. Lett. **57**, 37 (1990).

[16] Z. H. Lu, K. Griffiths, P. R. Norton and T. K. Sham, Phys. Rev. B **44**, 5648 (1991).

[17] A. K. Green and E. Bauer, J. Appl. Phys. **47**, 1284 (1976).

[18] Z. Ma and L. H. Allen, Phys. Rev. B **48**, 15484 (1993).

[19]   J.-J. Yeh, J. Hwang, K. Bertness, D. J. Friedman, R. Cao and I. Lindau, Phys. Rev. Lett. **70**, 3768 (1993).

[20]   K. Oura and T. Hanawa, Surf. Sci. **82**, 202 (1979).

[21]   B. Carrière, J. P. Deville and A. El Maachi, surf. Sci. **82**, 2929 (1979).

[22]   T. Narusawa, K. Kinoshita and W. M. Gibson, in *Proceedings of the Fourth International Conference on Solid Surface*, Cannes, 1980 [Le Vide, Les Couches Minces **210**, 673 (1980).]

[23]   K. Yagi, N. Osakabe, Y. Tanishiro and G. Honjo, Le Vide, Les Couches Minces **201**, 1007 (1980).

[24]   H. S. Jin, T. Ito and W. M. Gibson, J. Vac. Sci. Tech. A **3**, 942 (1985).

[25]   M. Hanbücken, Z. Imam, J. J. Métois and G. Le Lay, Surf. Sci. **162**, 628 (1985).

[26]   M. Hanbücken and G. Le Lay, Surf. Sci. **168**, 122 (1986).

[27]   B. Carrière, J. P. Deville, M. Hanbücken and G. Le Lay, in *Structure of Surfaces II. Vol. 11 of Springer Series in Surface Science.*, Eds. J. F. van der Veen and M. A. Van Hove (Springer, Berlin, 1988), p. 368.

[28]   K. Hricovini, J. E. Bonnet, B. Carrière, J. P. Deville, M. Hanbücken and G. Le Lay, Surf. Sci. **211/212**, 630 (1989).

[29]   Z. H. Lu, T. K. Sham, K. Griffiths and P. R. Norton, Solid State Communications **76**, 113 (1990).

[30]   Z. H. Lu, T. K. Sham and P. R. Norton, Solid State Communications **85**, 957 (1993).

[31]   X. F. Lin and J. Nogami, J. Vac. Sci. Tech. B **12**, 2090 (1994).

[32]   L. Braicovich, C. M. Garner, P. R. Skeath, C. Y. Su, P. W. Chye, I. Lindau and W. E. Spicer, Phys. Rev. B **20**, 5131 (1979).

[33]   P. W. Atkins, *Molecular Quantum Mechanics*, 2nd ed.(Oxford University Press, Oxford, 1983), p. 219.

[34]   E. Landemark, C. J. Karlsson, Y.-C. Chao and R. I. G. Uhrberg, Phys. Rev. Lett. **69**, 1588 (1992).

[35]   D. J. Chadi, Phys. Rev. Lett. **43**, 43 (1979): Appl. Opt. **19**, 3971 (1980).

[36]   D. T. Jiang, P. R. Norton, T. K. Sham and S. J. Naftel, *Unpublished data.*

[37]   B. S. Swartzentruber, Y.-W. Mo, M. B. Webb and M. G. Lagally, J. Vac. Sci. Tech. A **7**, 2901 (1989).

[38]   S. L. Molodtsov, C. Laubschat, G. Kaindl, A. M. Shikin and V. K. Adamchuk, Phys. Rev. B **44**, 8850 (1991).

[39]   S. Doniach and M. Šunjić, J. Phys. C **3**, 285 (1970).

[40]   G. K. Wertheim and S. B. Dicenzo, J. Elec. Spec. Rel. Phen. **37**, 57 (1985).

[41]   See for example: a) R. M. Friedman, J. Hudis, M. L. Perlman and R. E. Watson, Phys. Rev. B **8**, 2433 (1973), b) T. K. Sham, M. L. Perlman and R. E. Watson, Phys. Rev. B **19**, 539 (1979), c) P. M. Th. M. van Attekum, G. K. Werthiem, G. Crecelius and J. H. Wernick, Phys. Rev. B **22**, 3998 (1980), d) A. Bzowski and T. K. Sham, J. Vac. Sci. Tech. A **11**, 2153 (1993), e) D. T. Jiang, T. K. Sham, P. R. Norton and S. M. Heald, Phys. Rev. B **49**, 3709 (1994), f) S. J. Naftel, A. Bzowski and T. K. Sham, J. Alloys Comp. **283**, 5 (1999), and references therein.

[42]   R. E. Watson, J. Hudis and M. L. Perlman, Phys. Rev. B **4**, 4139 (1971).

CHAPTER 4: COBALT SILICIDE THIN FILMS[†]

4.1 INTRODUCTION

As noted in the introduction, transition metal silicides are used in the manufacture of modern MOSFET devices as low resistivity contacts to the source, drain and gate (Fig. 1.2). In the search for the silicide with optimal properties for incorporation into devices, almost all the transition metal silicides have been extensively investigated (for reviews see [1][2][3][4][5][6][7]). For existing devices, Ti ($TiSi_2$) has been the most commonly used metal silicide [8][9][10]. However, the continued down scaling of device size and development of new manufacturing techniques has demanded continual reevaluation of the properties of all the metal silicides [7][11][12][13]. Recently, Co has come under intense investigation as a possible candidate to replace Ti [7][10][13] in semiconductor devices. As a result cobalt silicides have been heavily studied [10][14][15] with the major thrust being the material's characteristics and compatibility with current processing techniques.

Typically the formation and properties of silicides have been studied by Rutherford Backscattering (RBS), Transmission Electron Microscopy (TEM), X-ray Diffraction (XRD), Auger spectroscopy and VB photoemission. Soft X-ray emission spectroscopy at the Si L-edge has also been extensively used [16]. However, even with the large volume of work on Co silicides, only a handful of studies using X-ray absorption have been

---

[†]Portions of this chapter have been published:
a) S. J. Naftel, I. Coulthard, Y. Hu, T. K. Sham and M. Zinke-Allmang, Mat. Res. Soc. Symp. Proc. **524**, 273 (1998).
b) S. J. Naftel and T. K. Sham, J. Synchrotron. Rad. **6**, 526 (1999).

published (see Table 4.1). These X-ray absorption studies have only focused on the pure spectra and theoretical descriptions. No studies have been carried out using X-ray absorption as a tool to follow changes in the electronic structure arising from variations in the thin film formation conditions.

Thin film silicides in industry are formed by heat induced diffusion synthesis [1][2][4][6][7]. In this process a layer of pure metal is deposited on (or in) a silicon substrate. The deposition is accomplished using any available metal deposition source, evaporation sources, sputtering sources, molecular beam sources, chemical vapour deposition, or even ion implantation to form buried silicide layers. Once deposited, the metal film is then heated to induce formation of silicide compounds at the interface between the substrate and metal by solid state reaction. The silicide phase grows and changes until all the metal deposited has been used and the desired silicide phase has been reached (See Fig. 1.3). The heating is accomplished by placing the sample in a furnace or by a Rapid Thermal Annealing (RTA) process.

Rapid thermal annealing [6] involves the heating of the sample by the application of an intense beam, either of photons or electrons. This process allows rapid heating of the sample surface, followed by rapid cooling. The sample is usually held at the desired temperature for only a few seconds and the heating process is repeated. RTA usually requires higher final temperatures than furnace annealing [6] but the processing time is seconds rather than hours in the furnace and small areas may be processed separately from the whole wafer. The short processing times and rapid heating and cooling of RTA can lead to distinct features in the formation of thin films.

Cobalt and silicon form four stable compounds in the bulk as seen in the phase diagram (Figure 4.1); however, only three compounds can be detected when thin films of Co are heated on a silicon surface to form a silicide thin film. Initially the Co and Si react to form a Co_2Si film, beginning at about 300 °C, which grows until all the Co deposited has reacted. At about 400-500 °C the CoSi phase starts to form. At higher temperatures the silicon rich final phase, $CoSi_2$, forms. $CoSi_2$ becomes the only phase present above 700 °C [6][7].

Figure 4.1. The Co-Si phase diagram. (From T. B. Massalski [17], used with permission)

$$Co \rightarrow Co_2Si \rightarrow CoSi \rightarrow CoSi_2 \qquad\qquad (4.1)$$
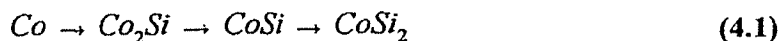
The above sequence of phases is the same whether the film is processed in a standard furnace or if RTA is used [6]. Generally, the sequential appearance of the phases is not distinct; thus two phases close in silicon content generally coexist in specific temperature ranges. For example, the Co_2Si and $CoSi$ phases have been observed to grow simultaneously at 400-500 °C [6]. Simultaneous existence of all the cobalt silicides has been reported in extremely thick (2 mm) samples [18]. Work has also been reported that at low coverages (3-4 ML) Co reacts with the substrate to form a $CoSi_2$ like phase at room temperature (see [15] and references therein). Overall it is clear that the growth depends strongly on the deposition conditions and thickness of the initial Co film.

Table 4.1 lists the crystal structures and lattice parameters for all the silicide phases seen along with other important parameters. All the silicides are metallic in character [27] with low resistivities. The final product, $CoSi_2$, is stable up to 950 °C once formed. Since $CoSi_2$ is the most important cobalt silicide industrially it has been most extensively studied with X-ray absorption, both in the bulk and as a thin film.

In this study the aim is to follow the differences in the electronic and physical structure of cobalt silicide thin films under various preparation conditions. X-ray absorption near edge structure spectroscopy will be used to investigate the electronic changes throughout the full depth of the films. In order to accomplish this, the variations in the sampling depth of XANES at different edges and detection techniques (Table 2.1), are capitalised on. This multi-core and multi-detection technique allows the films to be investigated from the perspective of the Co or the Si from a range of depths (surface to bulk). The XANES spectra together provide an accurate and non-destructive look at the morphology of the thin films.

Table 4.1. Important properties of the cobalt silicides.

Co Silicide	Crystal Struct.[a]	Resistivity $(\mu ohm$-cm$)$[b]	Formation Temp. (°C)[c]	nm of Final Silicide per nm of Co[d]	XAS edge and Ref.
Co$_2$Si	ortho., Co$_2$Si a=4.918 Å b=3.738 Å c=7.109 Å	~110	350-500	1.47	
CoSi	cubic, FeSi a=4.447 Å	~147	400-500	2.02	Si K [19]
CoSi$_2$	cubic, CaF$_2$ a=5.364 Å	14-20	600-700	3.52	Si K [19][20][21] Co L [20][21][22] [23][24] Co K [21][25]

[a]From P. Villars and L. D. Calvert [26], ortho.=orthorhombic.
[b]From U. Gottlieb et al. [27] and J. P. Gambino et al. [7].
[c]Compiled from [2][4][6][7].
[d]From S. P. Murarka [1].

4.2 SAMPLES

For this study, a CoSi$_2$ ingot was obtained to function as a standard reference. The CoSi$_2$ ingot was prepared from the melt by the materials preparation group at McMaster University using standard procedures. A set of three Co/Si(100) films were prepared at Northern Telecom using a DC sputtering technique. 55.6 nm of Co metal were deposited onto the Si(100) wafers and then annealed using a two step RTA process in a nitrogen ambient. The details of this procedure have been described elsewhere [28]. An additional thin film sample was obtained from Martin Zinke-Allmang of the Physics department at

the University of Western Ontario. This fourth film was prepared by annealing a 100 nm Co film deposited using an MBE process. The preparation conditions of all samples are given in Table 4.2.

All specimens were degreased by washing with methanol before introduction into the various vacuum systems. No attempt was made to remove the native oxide from the thin films. The $CoSi_2$ ingot was mechanically scraped with a diamond file to remove the majority of the oxide before introduction into the experimental chamber. A cartoon of

Table 4.2. Description and preparation conditions of the cobalt silicide samples.

Sample	Description
$CoSi_2$	Bulk ingot
Co-Si (1)	Co (55.6 nm) film, not annealed.
Co-Si (2)	Co (55.6 nm) film, annealed 450 °C/60 sec then 690 °C/60 sec.
Co-Si (3)	Co (55.6 nm) film, annealed 550 °C/60 sec then 690 °C/ 60 sec.
Co-Si(4)	Co (100 nm) film, annealed 525 °C/ 30 min, deposition at room temp.

the basic structure of the thin film samples, both before and after annealing, is presented in Figure 4.2. The structure of the films is also visually compared to arrows representing the approximate sampling depths at each edge and detection method. The sampling depths range from the very shallow (5 nm for Si L-edge TEY spectra) to well beyond the thickness of the films (> 10 μm for Co K-edge FLY spectra). Comparing the XANES
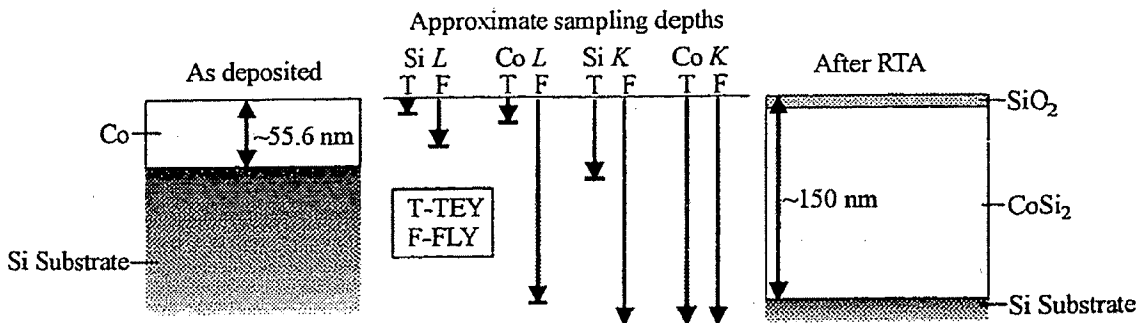
Figure 4.2. Schematic of the basic Co-Si thin film structure before and after annealing.

spectra with sampling depths across this range will provide information on how the thin film structure changes (what actual phases are formed and where) under the preparation conditions listed above.

4.3   EXPERIMENT

The experiments were carried out at four locations. Three different experimental arrangements were utilized.

The Co *K*-edge spectra were measured using beamline X-11A at the National Synchrotron Light Source (NSLS) located at Brookhaven National Lab. This beamline is equipped with a Si(111) double-crystal monochromator.

A standard ionization chamber, fed with a steady flow of Ar gas, was used to measure the incident photon intensity (I_0). Light of sufficient energy ionizes the gas in the detector creating electron/ion pairs. With the application of an appropriate voltage across the chamber the electrons and ions can be collected. The measured current will be proportional to the intensity of the incident light [29].

The spectra taken in a total electron yield (TEY) mode were obtained using a He amplified total electron yield detector [30]. This is basically a small ion chamber built around the sample. Photoelectrons emitted from the sample cause the subsequent ionization of the He atoms creating more photoelectrons which are accelerated to the collector grid. In this way the ionization of the He atoms amplifies the original photoelectron signal.

During some experiments, an Ar filled ion chamber detector was used to obtain fluorescence yield (FLY) spectra simultaneously with the TEY spectra. The monochromator was detuned 30 % during experiments in order to decrease contributions from higher harmonics. The sample was aligned to the beam by using pieces of photographic paper mounted in the same place as the samples. Figure 4.3 depicts the experimental setup and the He amplified TEY detector utilized.

The Si *K*-edge spectra were measured using the soft X-ray Canadian Double-

A) Experimental Setup

X-rays

Detector Leads

I_0 Ionization Chamber

He Amplified Detector

Sample

Fluorescence Detector

Detector Holder

B) He Amplified Detector

Shielding

Sample

Ni or Ag Grid

He in

X-rays

Electrons

He out

Bias Voltage
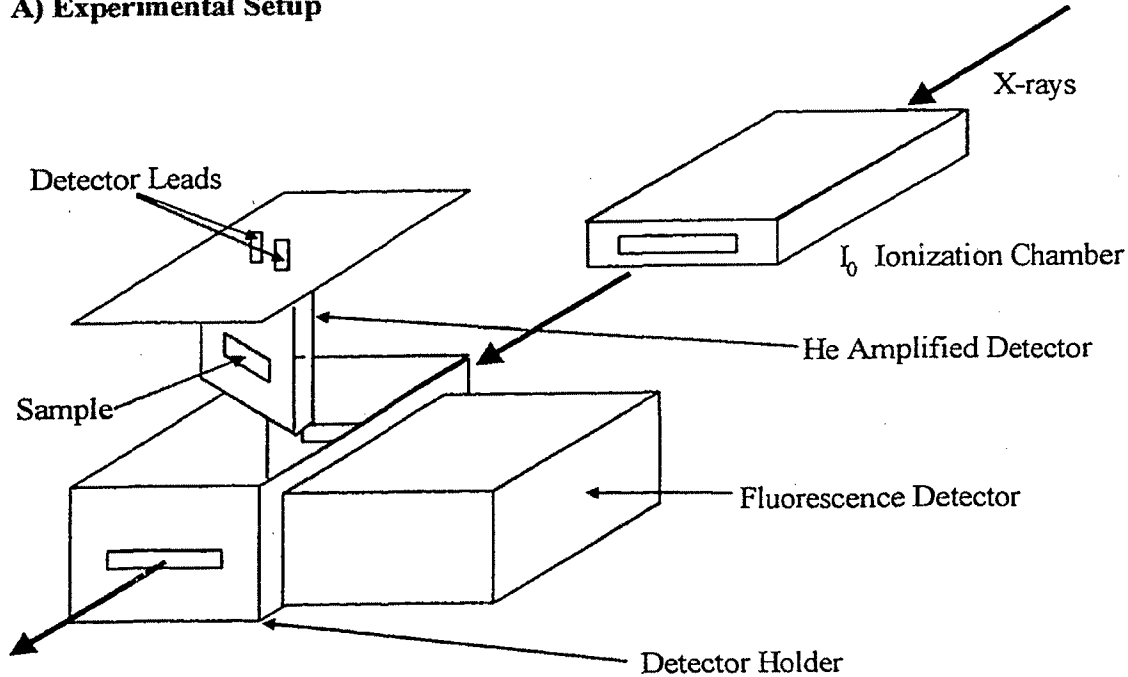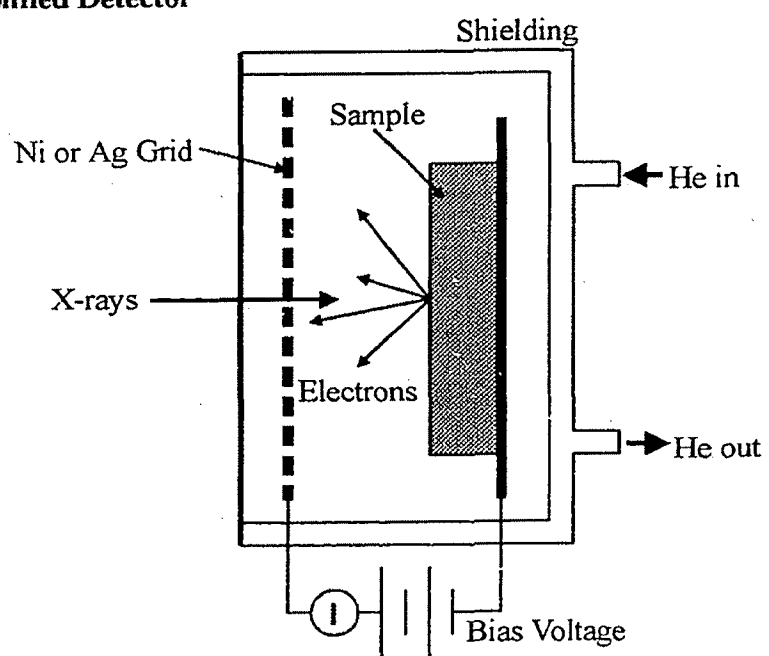
Figure 4.3. Schematic diagram of A) the experimental XANES setup on beamline X11-A and B) the He amplified TEY detector.

Crystal Monochromator (DCM) beamline of the Canadian Synchrotron Radiation Facility (CSRF) located at the Synchrotron Radiation Centre (SRC) of the University of Wisconsin-Madison. The DCM is equipped with InSb(111) crystals.

The incident photon intensity was measured using a N_2 ionization chamber. Unlike the ion chambers used at NSLS the chamber had to be sealed to isolate it from the beamline vacuum. Two Be windows isolate the N_2 cell from the beamline but allow the passage of X-rays.

Total electron yield spectra were obtained by measuring the sample current from ground. A wire loop was placed in front of the sample, so as not to interfere with the incident light, and held at +135 V. This setup pulls low kinetic energy electrons away from the sample. The vacuum system could also be equipped with a channel plate FLY [31][32] detector shown schematically in Figure 4.4B. The channel plate FLY detector consists of a Cu grid, two multi-channel plates (MCP) and a Cu collector, all electrically isolated from each other. The front of the first MCP was placed at -1450 V to prevent any electrons from reaching the detector. The incident fluorescent X-rays create a photoelectron cascade in the first MCP. The electrons accelerate to the second MCP where they are amplified and finally collected by the Cu collector. The collector current to ground was measured to provide a signal proportional to the intensity of the incident fluorescent X-rays. The FLY detector was placed at 90° to the sample in the plane of the ring.

The samples were mounted on stainless steel disks using double sided carbon tape which provided suitable electrical contact. Up to five disks could be mounted onto the manipulator at one time. The manipulator was aligned to the incident beam using a sixth disk coated in phosphor. Once the manipulator was aligned all the mounted samples could be reproducibly moved into position with the beam. The sample holder was mounted on a manipulator on which the sample angle could be controlled but most measurements were made in normal incidence. Figure 4.4A shows the typical experimental setup at the DCM beamline.

The Si L-edge spectra were measured on the Canadian Grasshopper

A) Exerimental Setup

TOP VIEW

Channel Plate Fluorescence Detector

Chamber

Sample Holder

Bias Coil (+ 135 V)

I_0 Chamber

X-rays

DCM Beamline

Be Windows

SIDE VIEW

Manipulator

Sample Holder

Bias Coil (+ 135 V)

Turbo- molecular punping system

Be Windows

I_0 Chamber

X-rays

DCM Beamline

SAMPLE HOLDER

Phosphor coated disk (for alignment of beam)

Sample Disks

B) Channel Plate Fluorescence Detector

-1450 V   -156 V   Cu collector

Cu Grid

Multi-channel Plates (MCP's)
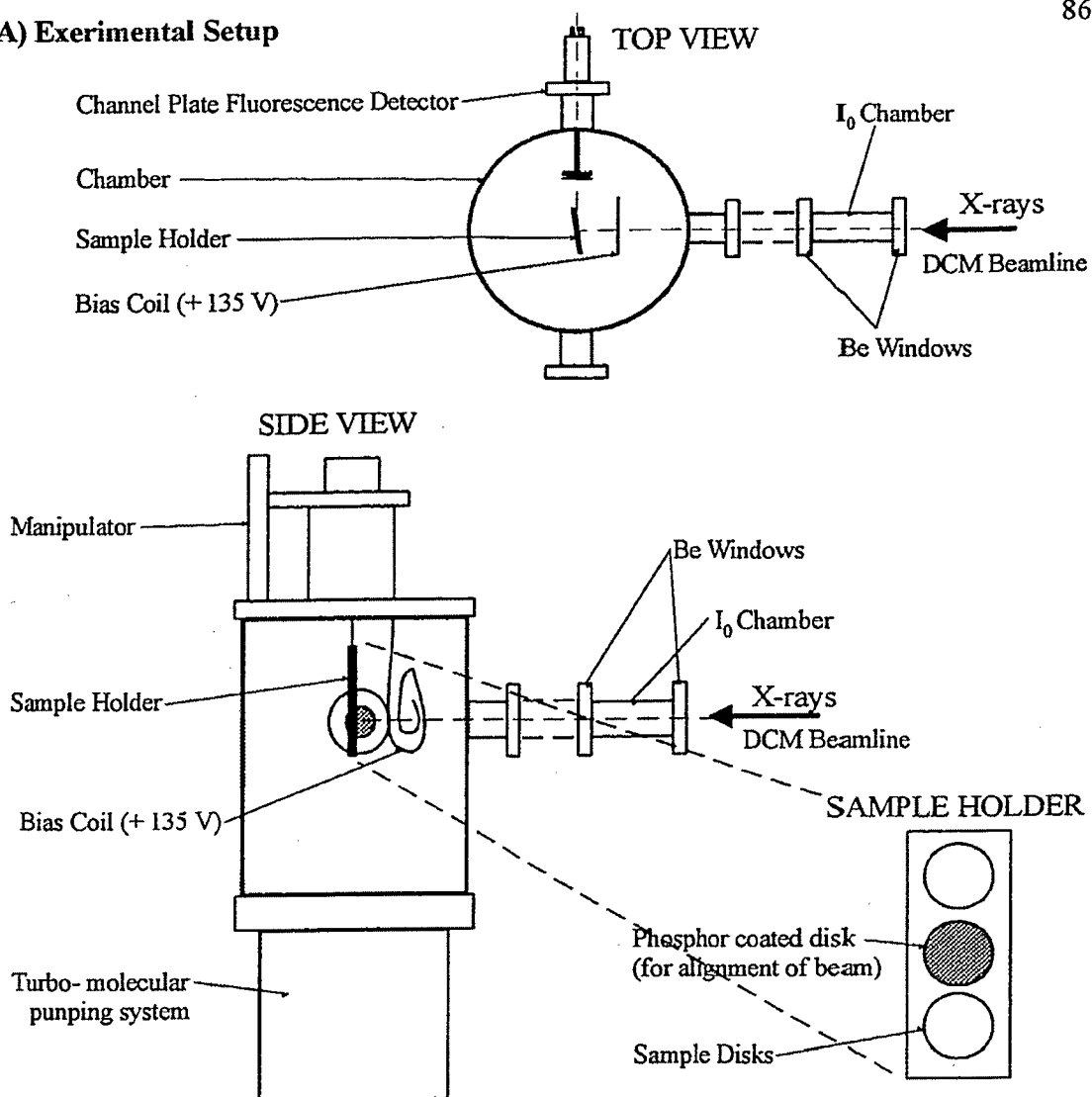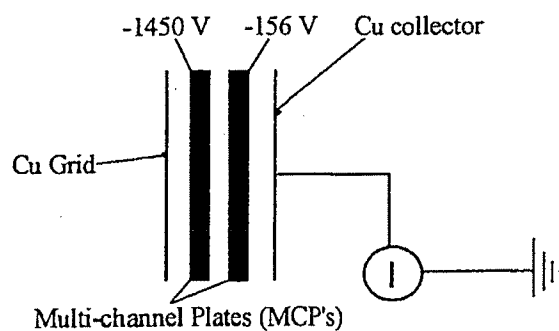
Figure 4.4. Schematic diagram of A) the experimental XANES setup on the Canadian DCM and B) the channel plate fluorescence detector.

A) Experimental Setup

TOP VIEW

Sample Holder

I_0 Detector

X-rays

Grasshopper Beamline

Load Lock Chamber

Channel Plate Fluorescence Detector

Transfer Arm

Gate Valve

SIDE VIEW

Manipulator

I_0 Detector

X-rays

Grasshopper Beamline

Sample Holder

Turbo Pump

B) Au Mesh I_0 Detector

Electrons

X-rays

Collector Bias (+150 V)
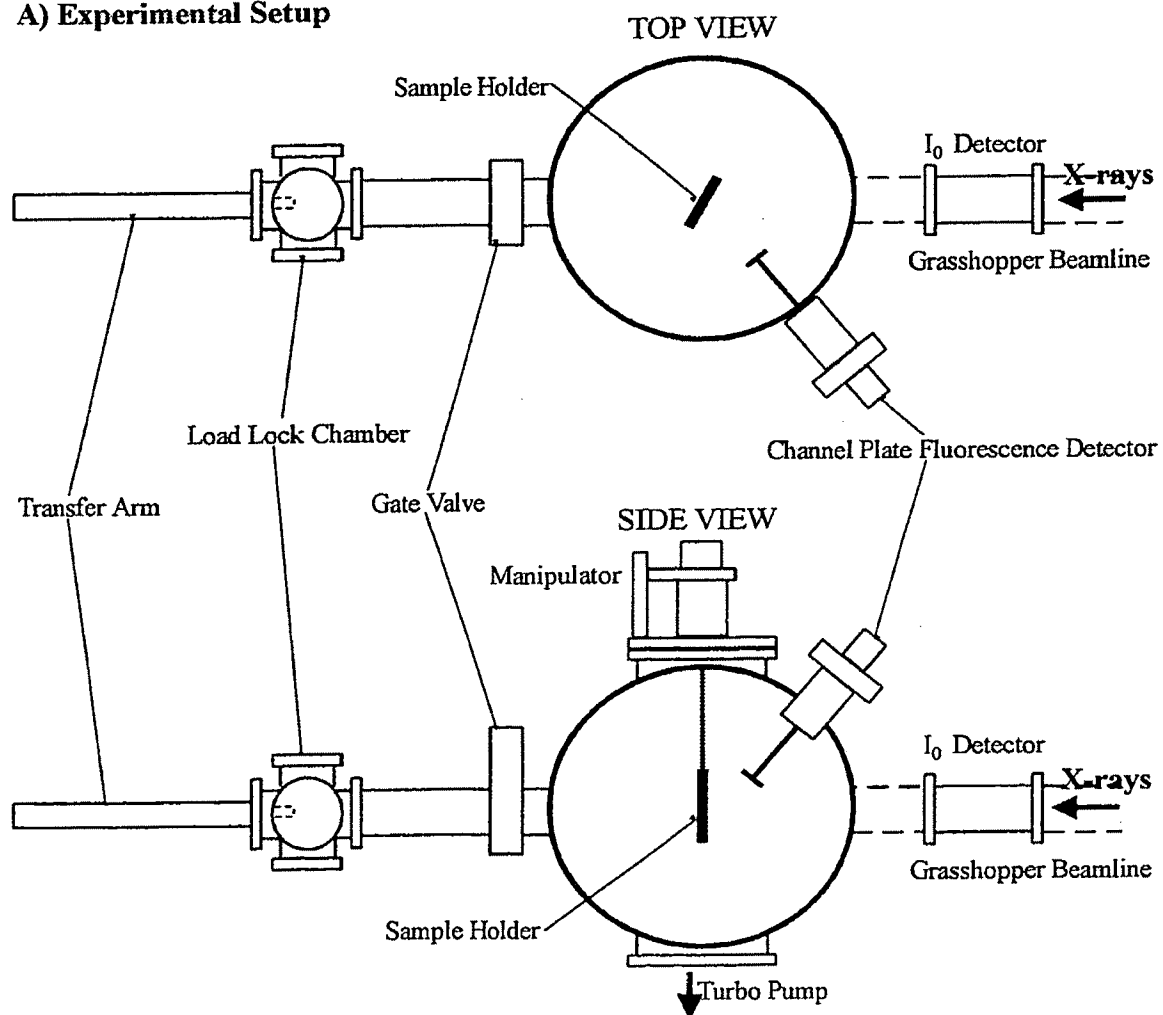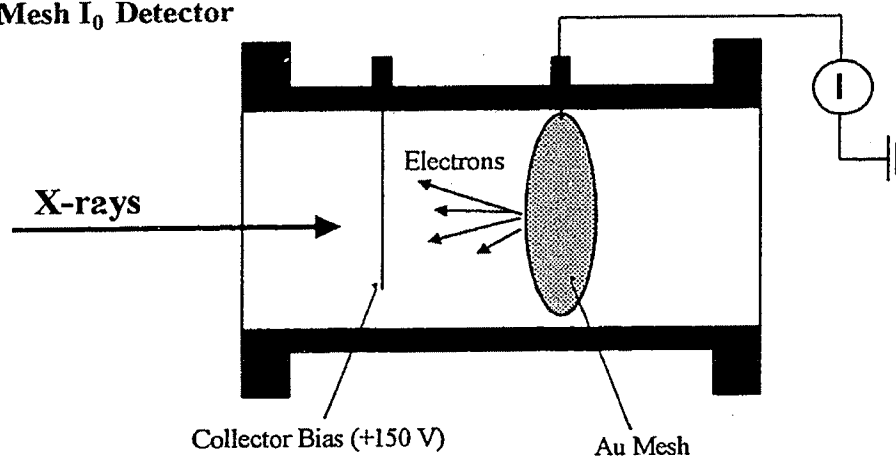
Au Mesh

Figure 4.5. Schematic diagram of A) the experimental XANES setup on the Canadian Grasshopper beamline and B) the Au mesh I_0 detector.

monochromator beamline of the CSRF. The grasshopper was equipped with a 1800 groove/mm grating which has its best resolution and intensity around 100 eV making it ideally suited for measuring Si L-edge spectra. The experimental chamber used for these measurements was the same as that used for the Co L-edge measurements. The Co L-edge spectra were measured on the High Resolution Monochromator (HERMON) beamline at SRC. HERMON was equipped with two variable line spacing plane gratings which can be changed easily without breaking vacuum in the beamline.

The experimental chamber used in these measurements was equipped with a load lock system which allowed a single sample to be introduced into the chamber without breaking the main chamber vacuum. The samples were again mounted on stainless steel disks with double sided carbon tape. TEY spectra were again measured via the sample current from ground; however, no additional voltage loop was present in this arrangement. The FLY spectra were again measured by a channel plate detector placed about 50° from the incident light and about 50° up out of the plane of the ring and sample. This detector position helps reduce interference from light reflected off the sample.

The incident light intensity was measured in these cases by a Au mesh I_0 detector. In this detector a thin Au mesh is suspended in the path of the photon beam. The incident X-rays cause photoelectrons to be ejected from the Au which are collected at a wire biased at +150 V. The current to the Au mesh from ground is measured and is proportional to the amount of incident light. The experimental setup is shown in Figure 4.5 along with a schematic of the Au mesh I_0 monitor.

4.4   RESULTS AND DISCUSSION

4.4.1   Si $L_{3,2}$-edge spectra

To start the investigation of the Co–Si films, the soft X-ray absorption spectra at the Si $L_{3,2}$-edge were examined. The Si $L_{3,2}$-edge arises from excitation of electrons in the Si 2p core levels. The near-edge structures originate from the allowed p→s or d

transitions. The spectra thus represent the densities of states above the Fermi level, specifically of s- and d-character. The Si 2p level is spin-orbit split into the $2p_{3/2}$ and $2p_{1/2}$ states with a separation of 0.6 eV. Transitions originating from these levels give rise to doublet structures in Si $L_{3,2}$-edge spectra separated by 0.6 eV. This doublet feature can be seen in the Si $L_{3,2}$-edge spectra of a Si(100) wafer shown in Figure 4.6.

All the Si L-edge spectra shown have had a linear pre-edge background removed. The Si(100) L-edge threshold energy (99.2 eV) was used as a standard for the calibration of the edge energies. An overall experimental resolution (photon, lifetime and spectrometer) of ~300 meV was obtained at the Si L-edge using the 1800 grove/mm grating and 30 μm slits in the grasshopper.

The Si(100) spectra shown in Figure 4.6 clearly consist of two distinct edges separated by about 5 eV. The first edge originates from Si atoms in the Si(100) environment while the second, at about 105 eV, originates from Si atoms in a SiO_2 environment [33]. Silicon naturally oxidizes in the ambient atmosphere to form a surface layer of SiO_2 which is the origin of this second edge. This separation of the Si and SiO_2 spectra is an important feature of the Si $L_{3,2}$-edge. Because the separation of 5 eV is significantly larger than the core hole lifetime broadening (< 0.3 eV) of the near-edge region, the Si spectrum, free of oxide features, can be studied without removing surface oxide so long as the oxide thickness does not exceed the sampling depth. This convenient feature allows us to study the Si $L_{3,2}$-edge XANES of the top-most layers of the Co-Si films without removing the native oxide.

Si(100) spectra taken in both Total Electron Yield (TEY) and Fluorescence Yield (FLY) are shown in Figure 4.6. The spectra clearly demonstrate the differences between the two XANES detection techniques used. In the TEY spectrum the silicon and oxide edges have edge jumps of similar intensity. In the FLY spectrum the relative intensity of the oxide edge is greatly reduced. This is a graphic illustration of the effect of the sampling depths of the two detection modes. TEY only samples approximately 5 nm [33] of the sample which is mostly composed of SiO_2. FLY on the other hand samples approximately 70 nm [33] of the sample, thus the number of Si atoms in an oxide
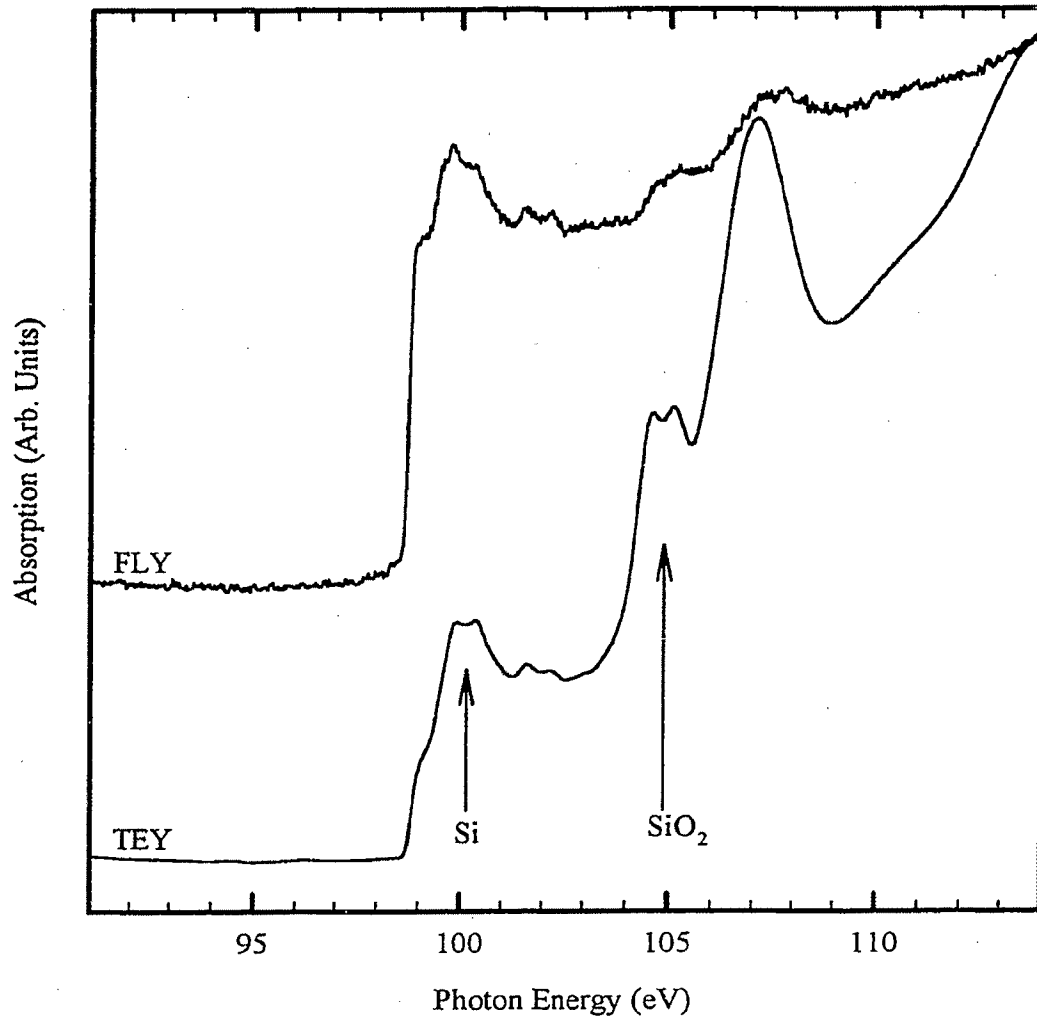
Figure 4.6. Si $L_{3,2}$-edge spectra of a Si(100) wafer in both TEY and FLY detection modes. The arrows indicate the two distinct edges.

environment decreases relative to the total number of silicon atoms in the crystalline environment. This leads to the relative reduction of the oxide edge seen in the FLY spectrum.

The Si $L_{3,2}$-edge XANES spectra of the Co-Si films taken in total electron yield mode are shown in Figure 4.7 along with the Si(100) and $CoSi_2$ spectra for comparison. As noted in chapter 2 and above, TEY detection leads to a sampling depth of only ~5 nm. With this sampling depth only the top most 100 ML or so of the sample give rise to the observed spectra.

Looking first at the TEY spectrum of the unannealed film (Co-Si (1)) we see a flat line. This is not surprising since this sample is simply a 55.6 nm film of deposited Co metal. Since X-ray absorption is element specific (ejection of a specific core electron), this tells us that there are not enough Si atoms within the top 5 nm of the sample to be detected. This in turn indicates that there was no significant diffusion of Si through the Co film or any significant solid state reaction to form silicides such that Si would appear at the surface. Reactions between Co and Si occurring at the interface between the materials can clearly not be ruled out at this point as they are beyond the sampling depth of the technique.

The TEY spectra of the two annealed DC sputter deposited films show no silicide edge occurring around 99 eV but only a SiO_2 edge at 105 eV. This clearly shows that in films (2) and (3) the surface is SiO_2 to a depth of at least 5 nm. The $CoSi_2$ bulk sample and the remaining film (4) both show the presence of a silicide edge around 100 eV. Although this edge is small it can still be seen that it has a two peaked structure. There is a broad increase in intensity before the obvious sharp features which makes the exact threshold position difficult to determine. Careful analysis shows that the threshold energy of $CoSi_2$ is shifted 0.4 ± 0.1 eV to lower binding (lower photon) energy compared to that of Si(100) (See the vertical line on Figure 4.7).

By changing to Fluorescence detection the sampling depth increases by about a factor of 10 (See Table 2.1, minimum ~25 nm to a maximum ~70 nm). Thus, the sampling depth for FLY detection at the Si $L_{3,2}$-edge is similar to the thickness of the
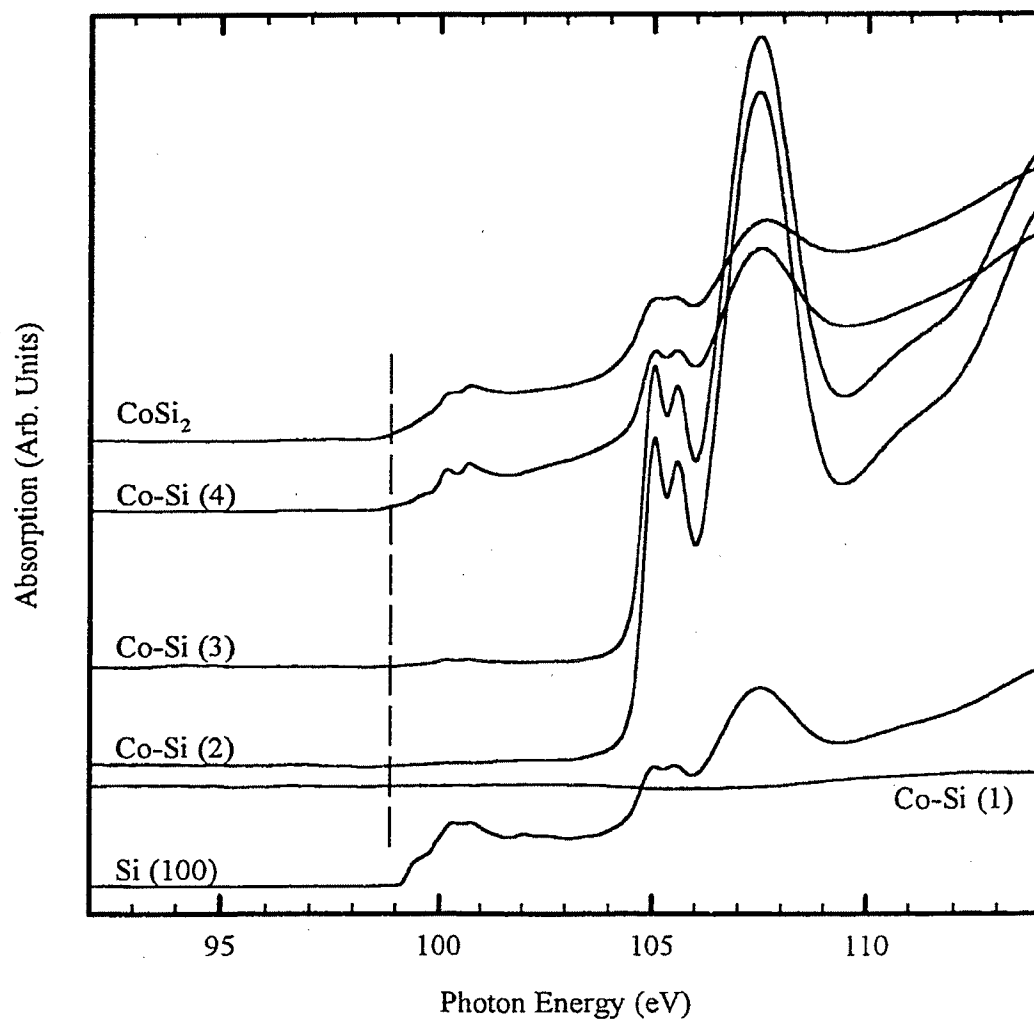
Figure 4.7. Si $L_{3,2}$-edge spectra of the Co-Si thin films, CoSi$_2$ and Si(100) taken in TEY mode. The vertical line indicates the CoSi$_2$ threshold position.
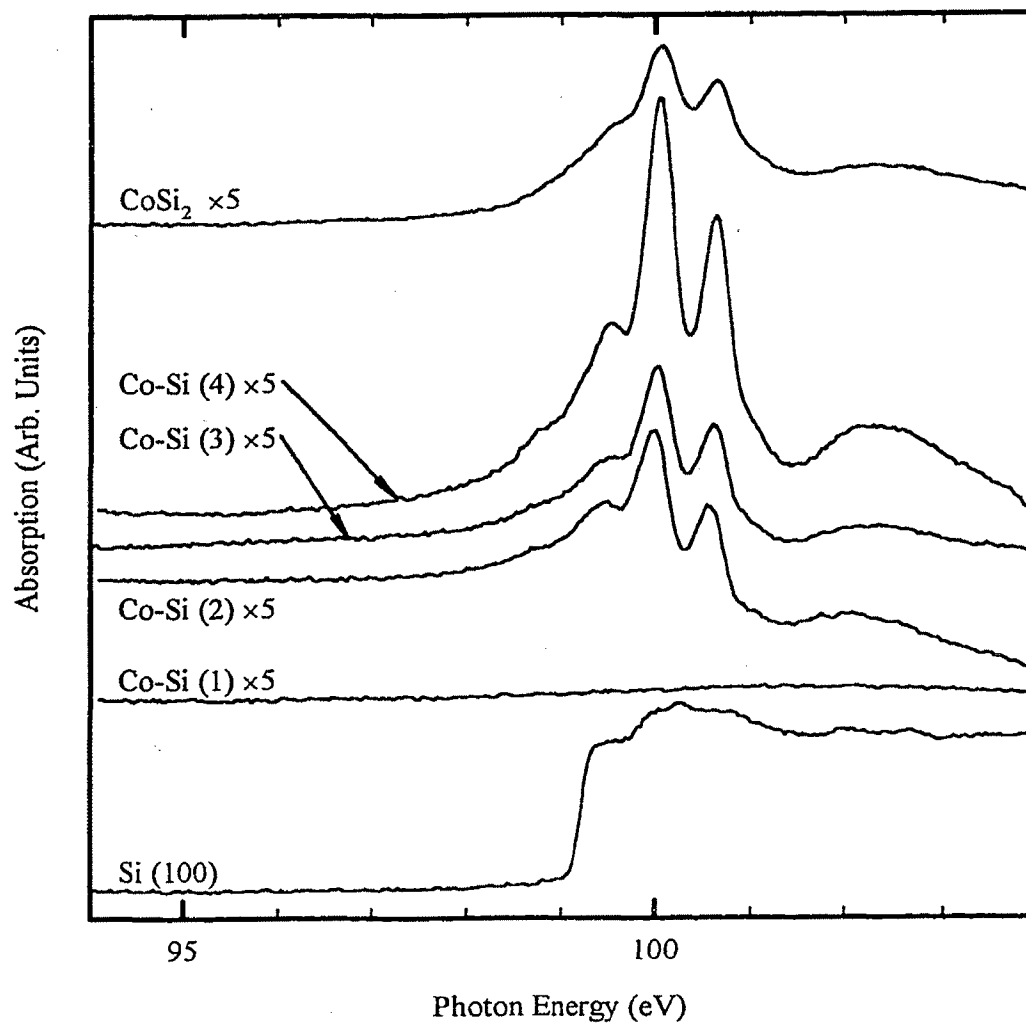
Figure 4.8. Si $L_{3,2}$-edge spectra of the Co-Si thin films, $CoSi_2$ and Si(100) taken in FLY mode.

original deposited Co layer. The Si $L_{3,2}$-edge spectra for the Co-Si films, bulk CoSi$_2$ and Si(100) are shown in Figure 4.8. Only the silicide region (<104 eV) of the spectra are shown after a pre-edge background removal. The oxide absorption (not shown) is still present but is significantly reduced in the FLY spectra as compared to the TEY spectra shown in Figure 4.7.

The spectra of the unannealed film is again a flat line in the silicide region, even with the increased sampling depth of FLY, confirming that no silicon has reached the top layers of the film. With the increased sampling depth of FLY the Si $L_{3,2}$-edge spectra of the annealed films can now be clearly seen.

The spectra of the annealed films consist of a broad shoulder followed by a spin orbit split doublet of narrow intense peaks. The spectra of the annealed films and the bulk CoSi$_2$ ingot are the same except for the relative intensity. Thus the silicide formed on annealing of the films can be identified as CoSi$_2$, which is the desired product. The threshold energy shift measured from the FLY spectra is again 0.4 ± 0.1 eV to lower binding energy from pure Si, as in the case for the TEY spectra.

The influence of the sample preparation can be clearly seen in Figure 4.7 as the sample prepared by annealing for longer time clearly has less surface oxide development than those prepared using the RTA procedure. At this point no difference between the two RTA annealed films is evident.

4.4.2 Co $L_{3,2}$-edge spectra

The Co $L_{3,2}$-edge spectra have the next largest sampling depths (Table 2.1). At the Co L-edge, the sampling depth of FLY is similar to the thickness of the silicide film formed (~150 nm), and the spectra are dominated by the bulk characteristics of the films. The FLY spectra for the Co $L_{3,2}$-edge are shown in Figure 4.9. All spectra have had a linear pre-edge background removed and been scaled to the maximum peak height. The position of the edge for the unannealed Co film was calibrated to the known position of the Co metal L-edge. In this case the spin orbit splitting between the Co 2p levels is
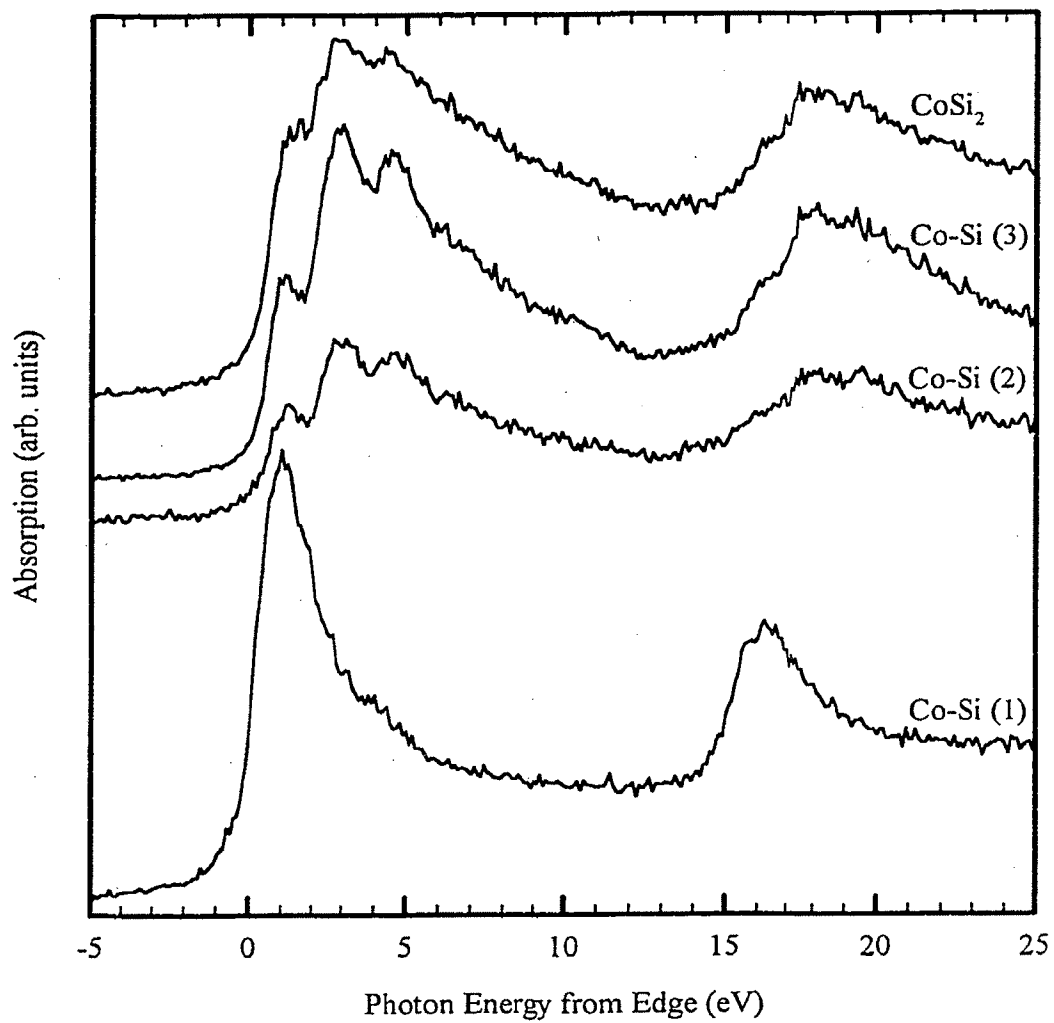
Figure 4.9. Co $L_{3,2}$-edge spectra of the Co-Si films and $CoSi_2$ taken in FLY mode.

15 eV which separates the contributions into the L_3-edge from the $2p_{3/2}$ level at 778 eV and the L_2-edge from the $2p_{1/2}$ level at 793 eV. The L_3-edge is the more intense and thus the most structure can be seen in it, so the following discussion focuses on the L_3-edges.

The Co L_3-edge of the unannealed film has one main peak (sometimes known as the whiteline) with an asymmetric tail. This corresponds to the expected spectra of Co metal [34] and represents the unoccupied densities of states of d-character above the Fermi level. The lack of any component in the spectrum due to a silicide is consistent with the Si $L_{3,2}$-edge results that the unannealed Co layer does not react with the underlying silicon to form any significant amount of silicide.

The spectrum of the $CoSi_2$ ingot has a three peak structure which has also been reported elsewhere for bulk $CoSi_2$ [20][21][22][24], confirming the identity of our ingot. The spectra of both the annealed films studied here (Co-Si (2) and Co-Si (3)) are similar to that of the bulk sample. This confirms the Si L-edge result that the bulk of the films is $CoSi_2$.

The threshold energy of the Co L_3-edge is shifted to higher photon energy (higher binding energy) by 0.6 ± 0.1 eV. The Si L-edge shifted to lower photon energy. At face value this indicates that Si gains charge and Co loses charge upon silicide formation. This is interesting in connection with electronegativity considerations, since Pauling's scale shows that Co and Si have nearly identical electronegativities, suggesting minimal net charge transfer. The apparent charge transfer must, thus, be viewed in terms of a charge redistribution in which Co favours d→s and Si favours p→s redistribution upon silicide formation. This is reasonable, since in the silicide the Co d-d interaction is reduced (Co has less Co nearest neighbours) and the Si sp^3 hybridization is broken by interaction with the metal. A reduction of 3d-charge at the Co site will increase the binding energy of all the core-levels even if the depletion is fully compensated for by a gain of s-charge; this is because the d-charge is more compact and screens the nucleus better than the 4s-charge. For the silicon, any change from sp^3 hybridization will increase the s-character at the Si site, and hence the screening, leading to lower binding energies [35]. The above picture of silicide bonding is similar to the charge compensation model [36] used to explain the

charge transfer in bimetallic alloys and to the accepted picture of silicide bonding [1][37] which involves metal d and silicon p rehybridization.

The Co $L_{3,2}$-edge spectra taken in TEY mode are shown in Figure 4.10. All spectra have had a linear background removed and been scaled to the maximum peak height. The sampling depth of TEY detection at this edge is estimated to be 10's of nm (at least 13 nm, see Table 2.1) thus the spectra are sensitive to the near surface region of the samples.

The spectrum of the $CoSi_2$ ingot (top spectrum in Figure 4.10) has essentially the same spectral features as that taken in FLY mode although they differ in intensity and width. The TEY spectrum of the unannealed film shows two distinct shoulders above and below the edge. These shoulders have been seen before, and Pong et al. [20] attribute them to metal oxide. These shoulders are not present in the FLY spectra, which samples to a greater depth, indicating that the unannealed film has a small amount of metal oxide present on the surface. This oxide layer could not be seen in the Si L-edge spectra because of the elemental selectivity.

The TEY spectra of the two annealed films are very different from their associated FLY spectra and the TEY spectra for $CoSi_2$. In these spectra there are many peaks overlapping, with the lowest energy peak having the highest intensity. This is most evident in the film that was only annealed to 450 °C in the initial RTA step. The near surface region of the annealed films is thus, clearly not solely $CoSi_2$ as concluded from the Si $L_{3,2}$-edge FLY data. The additional phase that exists is only visible in the Co $L_{3,2}$-edge TEY spectra, which probes the Co environment in the near-surface region of the film.

Since the FLY spectra indicate that the bulk of the films is predominantly $CoSi_2$, the TEY spectra could be expected to be a superposition of a $CoSi_2$ spectrum and the spectrum of the unknown surface phase. Taking the TEY spectrum from the $CoSi_2$ ingot, scaling it to just below the background level between the L_3- and L_2-edges, then subtracting the scaled spectrum from the spectra of the annealed films should give an approximation of the spectrum of the unknown phase. The results of this procedure are shown in Figure 4.11. The difference spectra thus generated are compared to the spectra
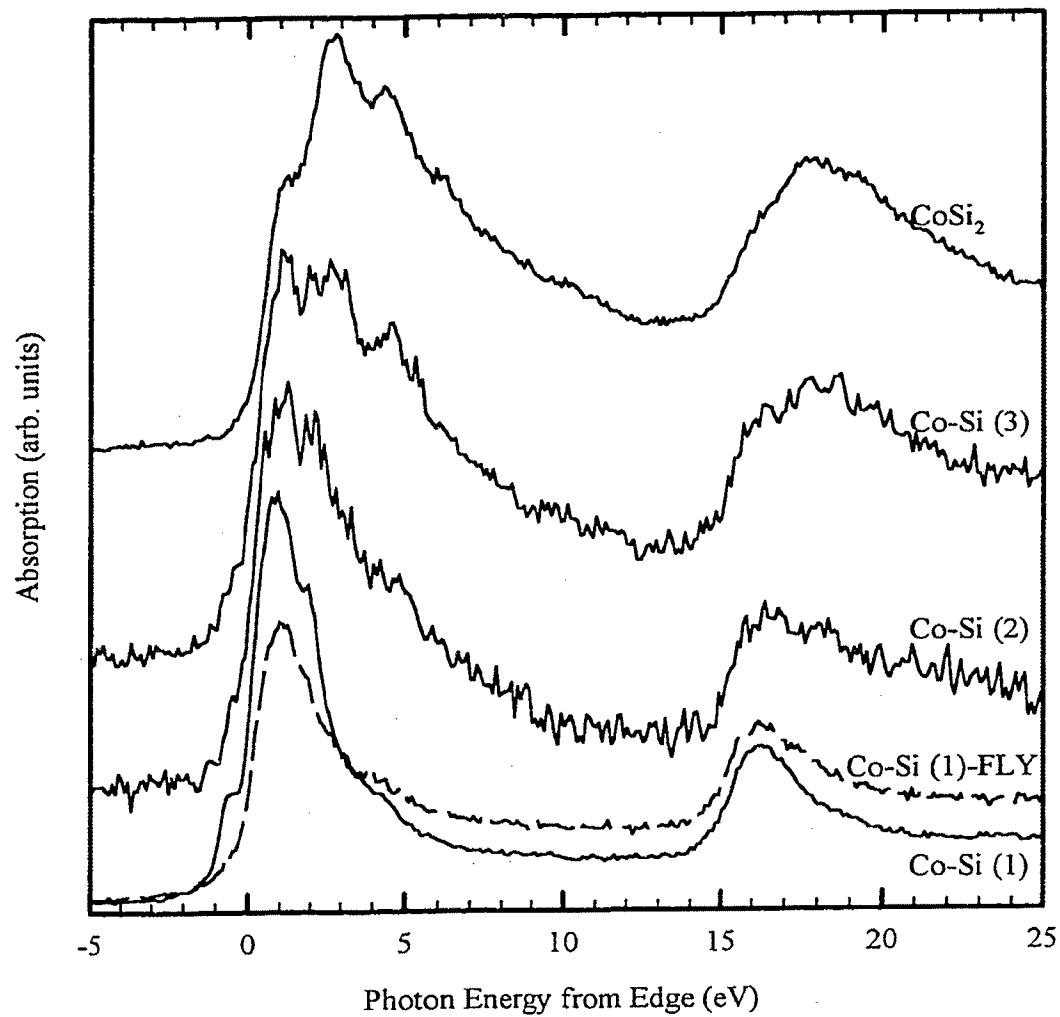
Figure 4.10. Co $L_{3,2}$-edge spectra of the Co-Si films and $CoSi_2$ taken in TEY mode. The FLY spectra of the Co film on Si (Co-Si (1)) is also shown for comparison.
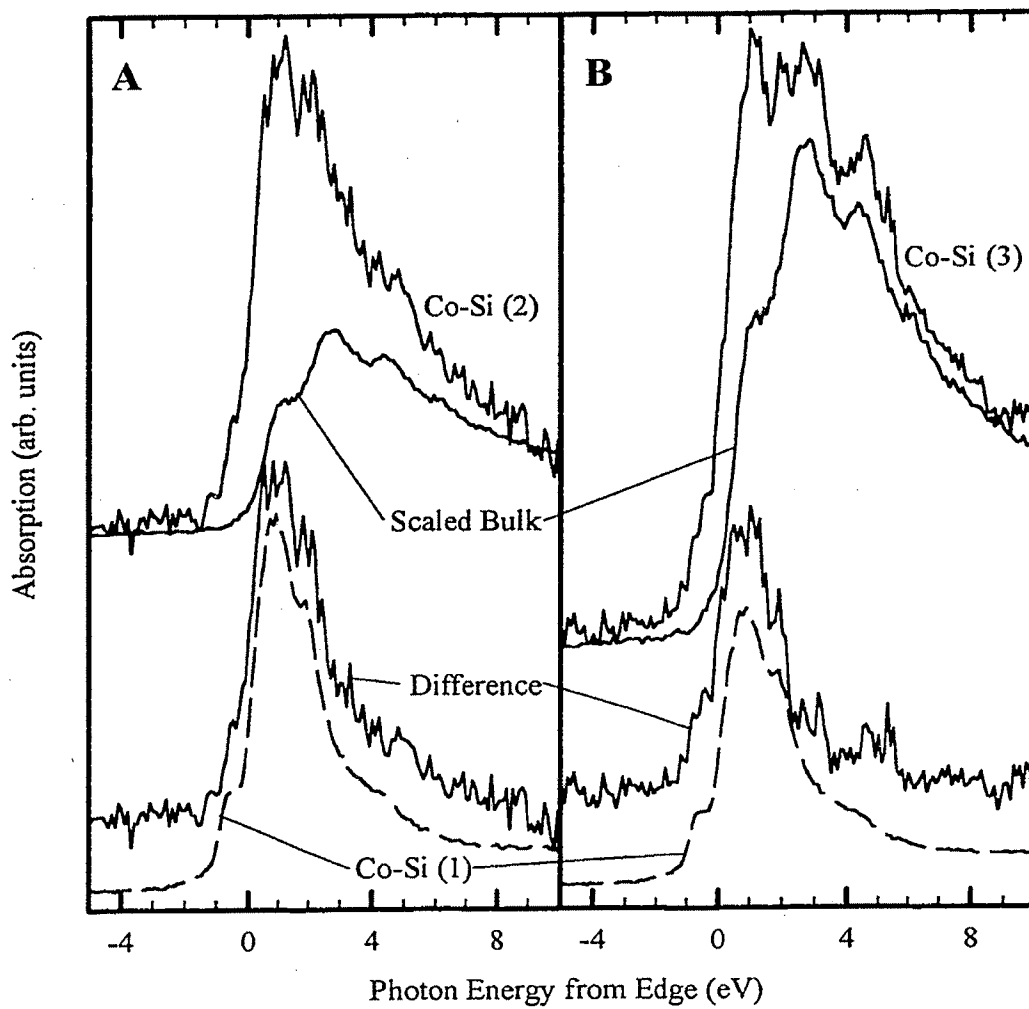
Figure 4.11. Subtraction of scaled bulk $CoSi_2$ spectra from the TEY spectra of the annealed Co-Si films, compared to the TEY spectrum of the unannealed film. A) Co-Si (2), B) Co-Si (3).

of the unannealed film (Co metal). Both difference spectra match that of the Co spectra, indicating that the additional phase present at the surface of these films is Co metal. The identity of this surface phase as Co is corroborated by the fact that no evidence of its existence is seen in the Si $L_{3,2}$-edge FLY spectra, which matched the spectra of pure $CoSi_2$. If the phase had been one of the Co rich silicides, the Si $L_{3,2}$-edge FLY spectra of the annealed films should have been a mixture of silicide spectra and would not have matched that of $CoSi_2$.

The presence of metallic Co in the surface and near-surface regions of the RTA prepared samples was unexpected. The Co could exist as a layer between the SiO_2 cap and the $CoSi_2$ film, or as regions of Co and SiO_2 interdispersed on the surface of the $CoSi_2$ film. The two possibilities can not be distinguished on the basis of XANES alone, a surface sensitive technique such as photoemission spectroscopy would allow the exact morphology of these surface layers to be determined.

The fact that the metallic Co component of the spectra in Co-Si (2) was more intense, relative to the $CoSi_2$ component, than in Co-Si (3) points to the dependence of this phenomenon on the preparation conditions. From the Si $L_{3,2}$-edge TEY spectra (Figure 4.7), it was seen that Co-Si (4), which was annealed in one long step, had significantly less surface oxide formed on it than the RTA prepared samples; this also points to a dependence of the surface structure to the preparation conditions of the films. M. Saran and A. Naem [28] have seen a dependence on the first anneal temperature in the sheet resistance and diffuse reflectivity of similar Co-Si films.

The origin of the metallic Co is puzzling. The possibility of there being an unreacted layer of Co metal on the surface after the annealing of the films can be ruled out from the details of the preparation of the RTA films [28]. The RTA films were subjected to an etch (70% H_3PO_4, 28% CH_3COOH, 2% HNO_3) between annealing steps to remove any unreacted Co that remained from the first RTA step. Thus if the second step was incomplete, the top layer would be either Co_2Si or CoSi, not Co.

The near noble metal silicides ($CoSi_2$, $NiSi_2$, NiSi, for example) are known to oxidize via the decomposition of the silicide to give SiO_2 and the pure metal. The metal

then diffuses through the underlying silicide to the Si/silicide interface where it reacts to form more silicide [7][38][39]. This occurs because, for the near noble metals, the metal diffusivity is high. Most studies of metal silicide oxidation, however, are done at elevated temperatures to match conditions used in industrial oxidation processes. At room temperature the diffusivity may decrease enough to prevent the diffusion of the Co through the silicide and thus Co may build up at the silicide/oxide interface. K. Prabhakaran and T. Ogino [39] observed that $CoSi_2$ decomposed during oxidation and that Co diffused to the Si/silicide interface at low temperatures as well; however, their silicide was only ~2 ML thick.

The decomposition of the surface silicide with limited metal diffusion may explain the existence of metallic Co in the surface and near-surface region of the films but why and how the oxidation behaviour depends on the preparation conditions is still unknown. A more detailed study of this phenomenon is necessary.

4.4.3   Si K-edge spectra

The Si K-edge core level, at 1839 eV, has the next deepest sampling depth. At photon energies around the edge, the incident X-rays penetrate well beyond the film thickness. At the Si K-edge then, the data are complicated by the presence of the substrate Si crystal.

Using fluorescence yield, the sampling depth is several hundred nm; thus the majority of the measured signal is expected to originate from the substrate silicon. The FLY spectra shown in Figure 4.12 for the films bears this out. All the spectra from the films are very similar to that of the Si(100) standard spectrum. Compared to the Si(100) spectrum, the spectra of the films display a relative reduction in the whiteline intensity and broader features. These two differences point to the presence of the silicide whose spectrum must contribute to those observed.

The FLY spectrum of the bulk $CoSi_2$ ingot is also shown as the bottom curve in Figure 4.12 This spectrum closely matches previously published spectra and calculations
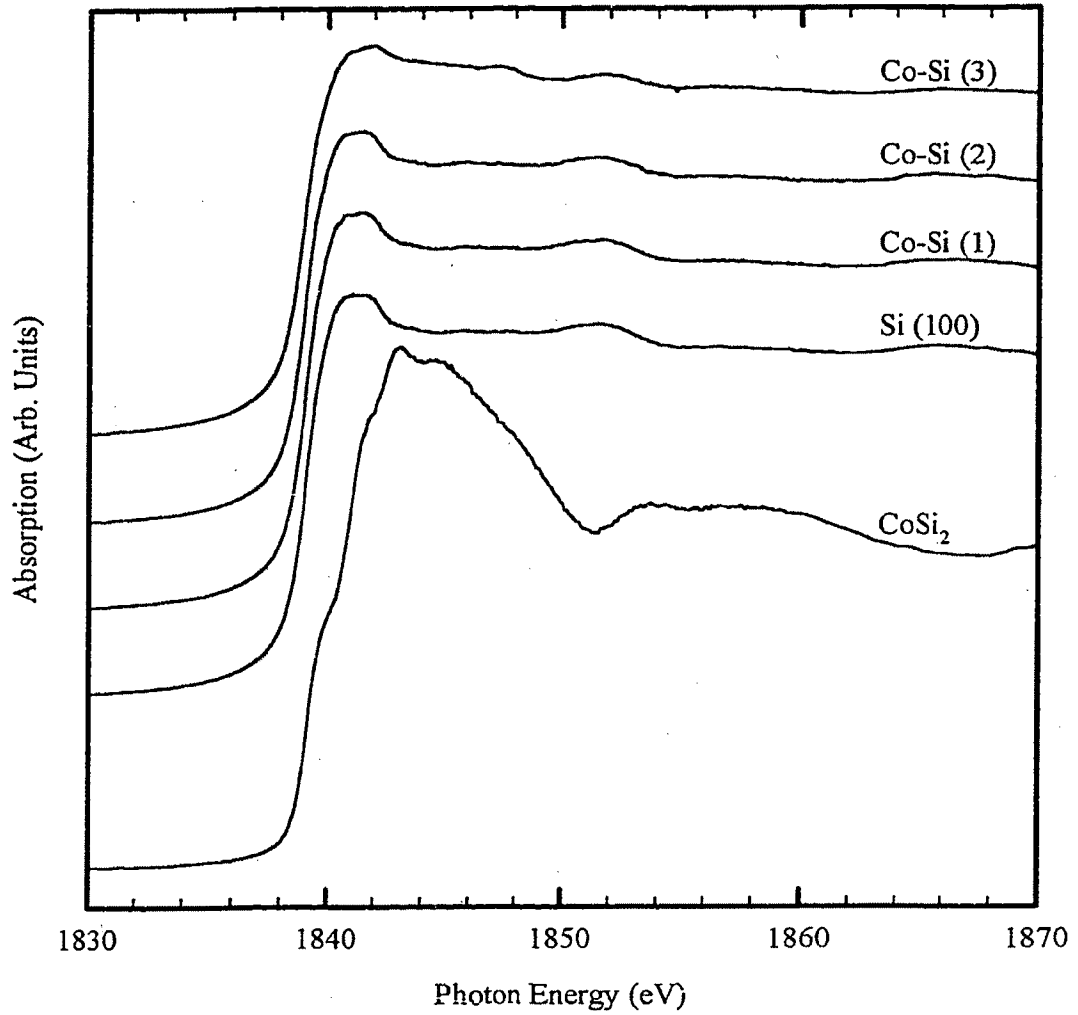
Figure 4.12. Si K-edge spectra of the Co-Si films, Si(100) and CoSi$_2$ taken in FLY mode.

[21] for CoSi$_2$, confirming that the ingot is in fact CoSi$_2$.

Total electron yield detection is inherently more surface sensitive. At the Si K-edge the TEY sampling depth is only about 40-70 nm (Table 2.1) which is similar to the unannealed thickness of the deposited Co film. Thus, TEY effectively minimizes the effect of the underlying Si substrate in the spectra. It should be noted for the unannealed film, TEY can still sample the underlying substrate. Figure 4.13 shows the TEY Si K-edge spectra for the films, clean Si(100) and the CoSi$_2$ ingot. All spectra have been normalized to an edge jump of unity after pre-edge background removal.

Looking first at the spectrum of the unannealed film (Co-Si (1)) it is, at first glance, similar to the spectrum for Si(100). However, three differences are apparent between the two spectra:

1) The relative whiteline intensity is greatly reduced in the spectrum of the as-deposited film.

2) There is a peak at ~1844 eV in the spectrum of the unannealed film, and

3) The whiteline of the unannealed film is broader than that in Si(100).

Similar differences have been seen in the Ni-Si system [40]. The presence of the above differences indicate that some reaction occurs at the interface between the deposited Co metal and the Si(100) substrate even at room temperature. This reaction is most likely the formation of a Co rich silicide at the interface. Because the spectrum of the unannealed film is predominantly that of the substrate silicon, the contributions to the spectrum of the interfacial phase can not be determined, except for the presence of the peak at ~1844 eV.

The TEY spectra of the annealed films clearly resemble that of the bulk CoSi$_2$ ingot, and with Si K-edge spectra from the literature [19][20][21], except for a much larger peak at ~1847 eV. This peak arises predominantly from SiO$_2$; however, it has a small contribution from a silicide peak as well [41]. The intensity of the oxide peaks in the two films suggests that the lower temperature annealed film (Co-Si (2)) has had more oxide formed by reaction with the ambient atmosphere.

The presence of the silicide peak can be seen by comparing the CoSi$_2$ spectra taken
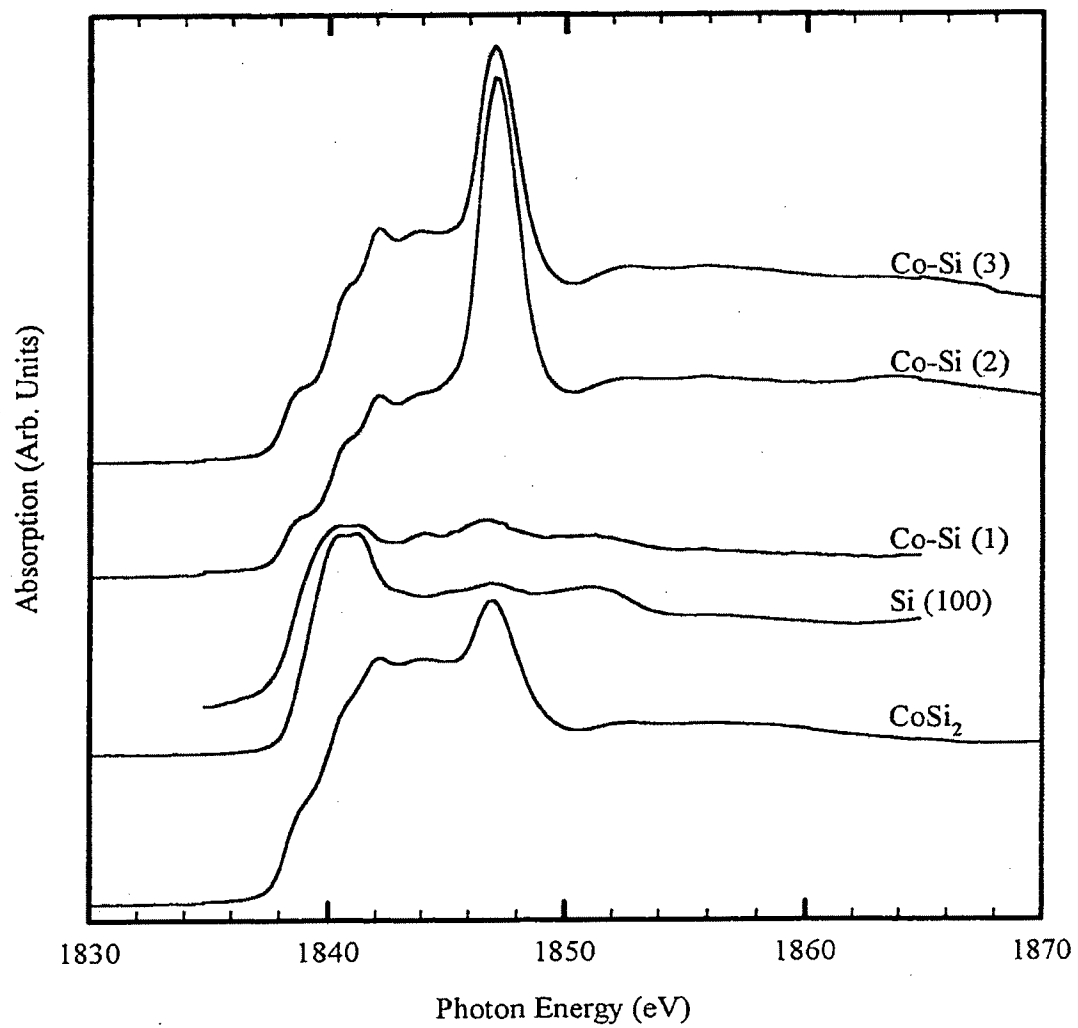
Figure 4.13. Si K-edge spectra of the Co-Si films, Si(100) and CoSi$_2$ taken in TEY mode.
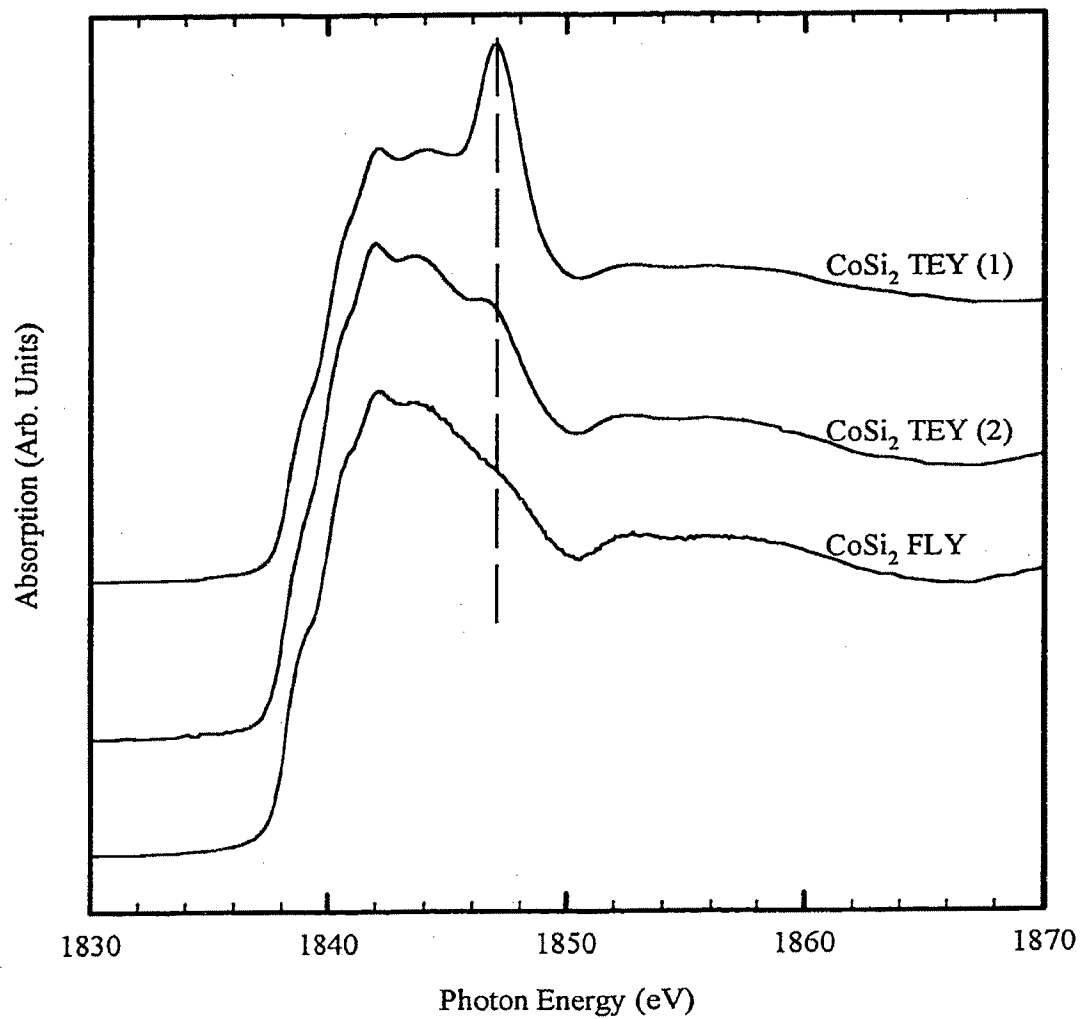
Figure 4.14. Comparison of Si K-edge spectra of $CoSi_2$ taken in different detection modes and sample preparation conditions. The vertical line indicates the position of the SiO_2 peak.

in TEY and FLY modes. Figure 4.14 compares the $CoSi_2$ spectra from two different TEY spectra and an FLY spectra. The two TEY spectra differ only in their preparation (more or less scraping). The only difference between these spectra is the intensity of the peak at ~1847 eV. The bulk sensitive FLY spectrum lacks a large peak at ~1847 eV but, there is a small shoulder present which is attributed to $CoSi_2$.

Overall, Si K-edge data confirm that:

1) The bulk of the annealed films is largely $CoSi_2$.

2) There is an SiO_2 layer on the surface of the annealed films which varies in thickness with the preparation conditions.

3) There is some interaction between deposited Co metal and the silicon substrate at the interface that occurs upon deposition at room temperature before annealing.

4.4.4   Co K-edge spectra

The Co K-edge, corresponding to absorption of photons by the 1s electron of Co, has a threshold energy of 7709 eV in pure Co metal. At these energies the sampling depths for TEY and FLY are estimated at ~300 nm and ~8.9 μm, respectively. With these estimates it is easy to see that in the case of the Co K-edge the sampling depth for both detection methods far exceeds the expected thickness of the final silicide films (~ 150 nm). The actual sampling depth in this case is limited to the distribution of Co in the sample since the X-ray absorption is site selective.

The Co K-edge spectra are shown in Figure 4.15. The spectra have had a linear pre-edge background removed and then have been normalized to an edge jump of unity (edge jump is calculated from the pre-edge background to the EXAFS background level).

It is apparent that the EXAFS spectra of the annealed films are similar to that of the $CoSi_2$ ingot. Since the EXAFS oscillations are sensitive to the physical structure of the material, it is clear that the films are composed of $CoSi_2$ predominantly. The unannealed film (Co-Si (1)) is clearly distinct from the other spectra, which is understandable as no extensive reaction between the Si and Co is expected without
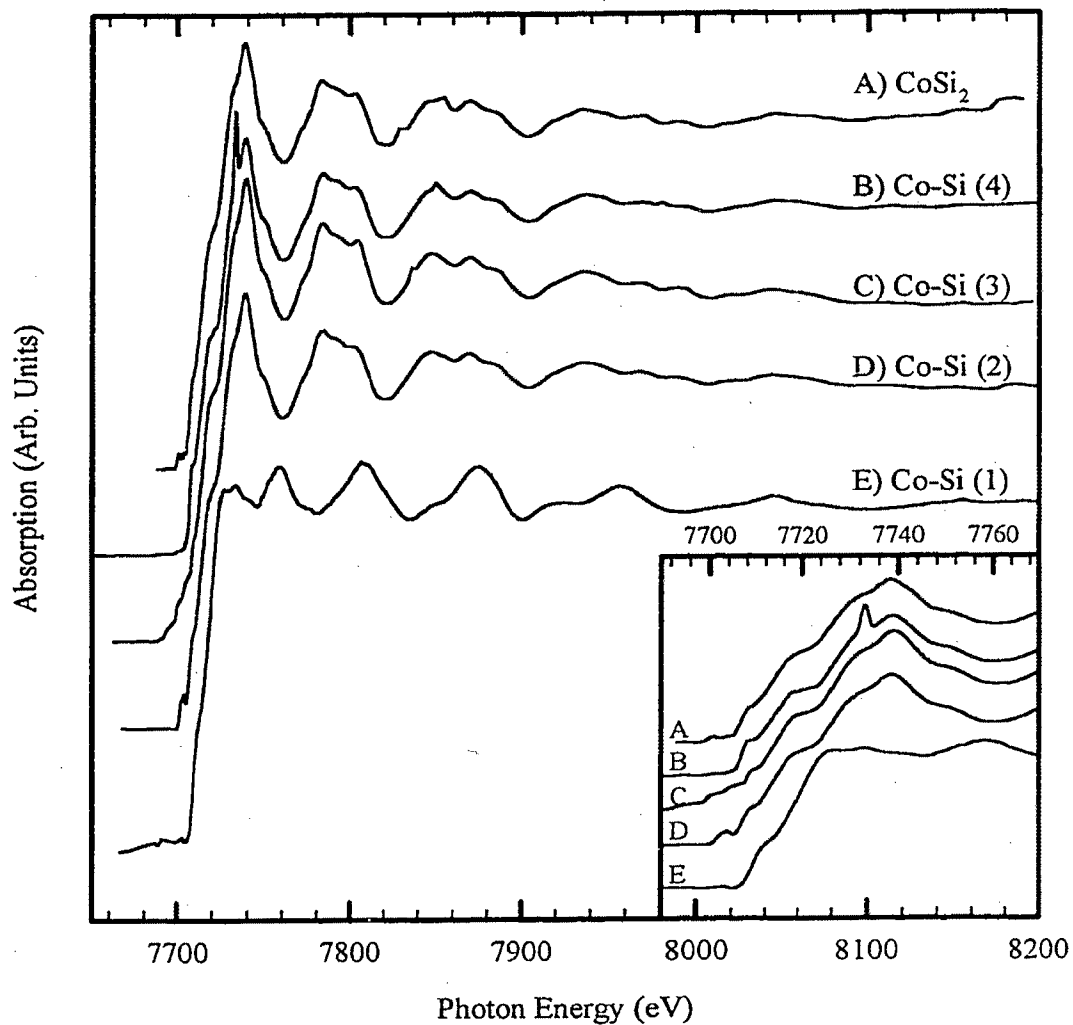
Figure 4.15. Co K-edge spectra of the Co-Si films and $CoSi_2$ taken in TEY mode. The inset shows the detail of the XANES region of the spectra.
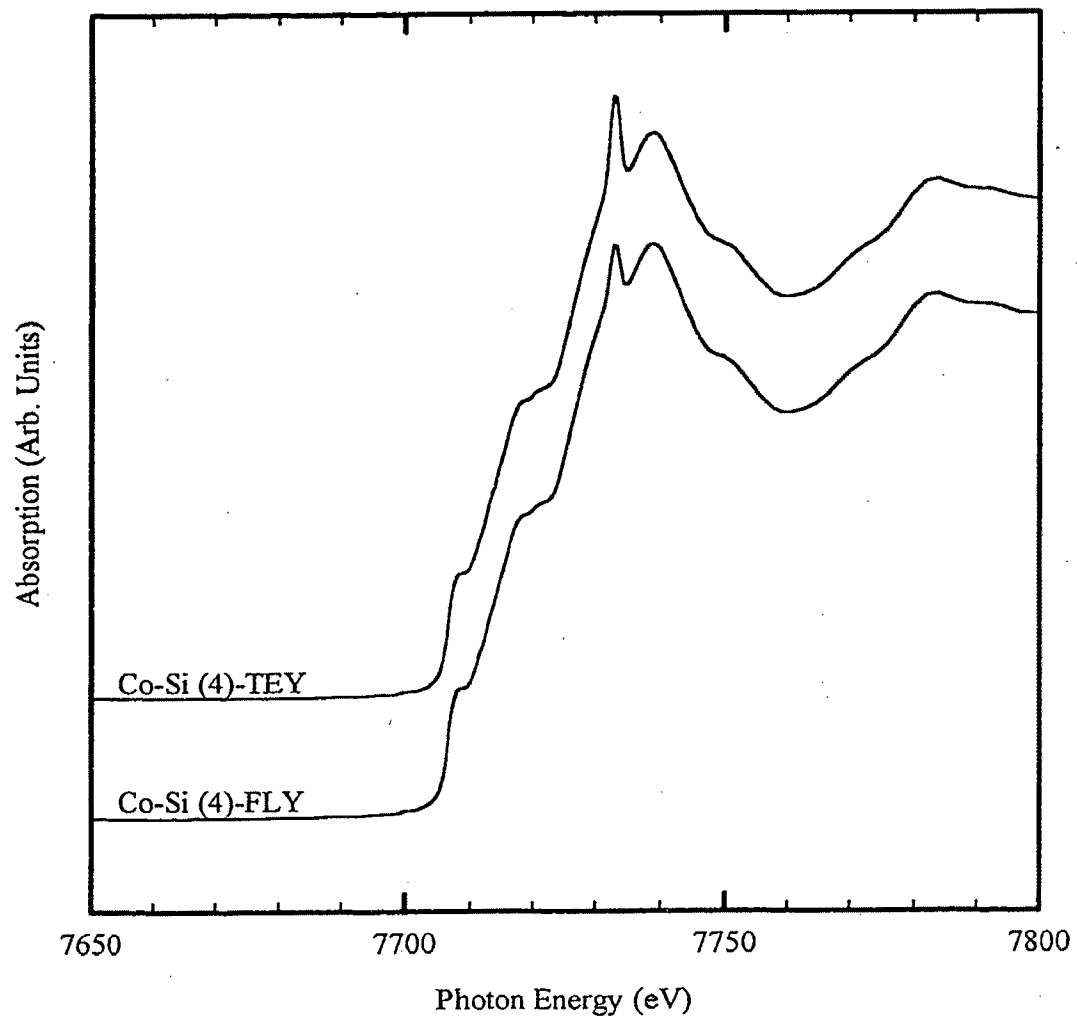
Figure 4.16. Comparison of TEY and FLY Co K-edge spectra for Co-Si (4).

annealing.

The Ni K-edge spectra for Co-Si (4) is similar to that of Co-Si (3), Co-Si (2) and CoSi$_2$ except for the presence of a peak at about 7730 eV. The origin of this peak is not known; although, it could relate to the presence of some impurity picked up in the processing of the Co-Si (4) sample. The rest of the spectral features, especially EXAFS, indicate that the Co-Si (4) film is largely CoSi$_2$.

Figure 4.16 shows a comparison of the TEY and FLY spectra for Co-Si (4). It is clear that the spectra are similar as would be expected since the element specificity limits the sampling depth of both techniques to the same region of the sample. Thus, both detection methods agree with each other that the films are composed predominantly of CoSi$_2$.

4.5 CONCLUSIONS

This study set out to investigate the structure of Co-Si films, formed by standard thermal annealing processes used in industry. For this purpose XANES spectroscopy was chosen. The reasons for choosing XANES were:

1) XANES is a proven technique that has been used to study the electronic and physical structure of many systems.

2) The Co-Si system has rarely been investigated by X-ray absorption.

3) The availability of beamlines and equipment to the group offered the opportunity to capitalize on the inherent characteristics of XANES.

This investigation, together with others (Ni-Si, Pt-Si, Al-TiN), was aimed at investigating the feasibility of using soft X-ray XANES to characterize thin films industrially, either in a research setting or as quality control.

The samples obtained were made under slightly different preparation conditions but were expected to give a basic CoSi$_2$ film (Figure. 4.2). It was found that a more detailed picture was required (Figure 4.17, below) to account for the observed results.

For the unannealed film it was found that the surface of the deposited Co film was
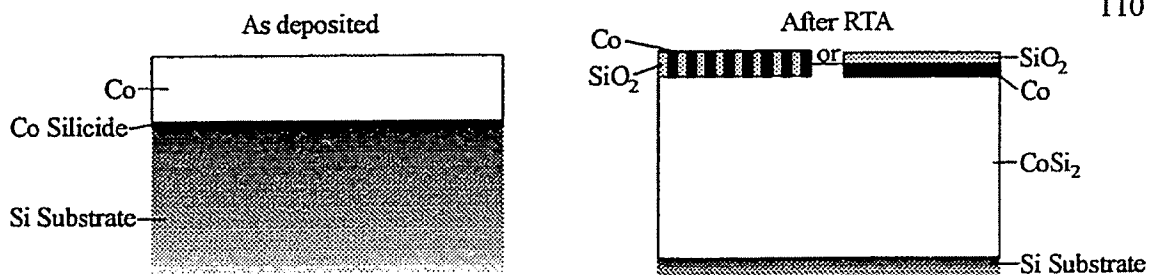
Figure 4.17. Schematic of the structure of the studied Co-Si films.

oxidized in the ambient and that some reaction occurred at the Co-Si interface even without annealing.

For the annealed films we found:

1) The films were capped with SiO_2 layers, less than 5 nm thick, but the thickness varied with the preparation conditions.

2) Metallic Co was found in the surface and near-surface regions of the films. This metallic Co could exist as a thin layer under the oxide cap or as regions of Co interdispersed with SiO_2. The exact morphology of the metallic Co could not be determined from XANES. Photoemission spectroscopy should distinguish between Co, SiO_2 layers or a mixture of phases. The intensity of the metallic Co spectra varied with the preparation conditions. The exact origin of this layer of Co could not be determined from this study but is thought to be related to the oxidative decomposition of the surface silicide to give Co and SiO_2.

3) The bulk of the film was indeed $CoSi_2$.

Overall it was found that multi-core multi-detection XANES is well suited to the study of thin films and buried interfaces.

4.6 CALCULATIONS OF COBALT SILICIDES

Many of the spectra discussed in the preceding section have distinctive structures. For example, the Si L-edge, which has not been theoretically investigated, has intense narrow features. Some distinctive spectral features were also found that may relate to
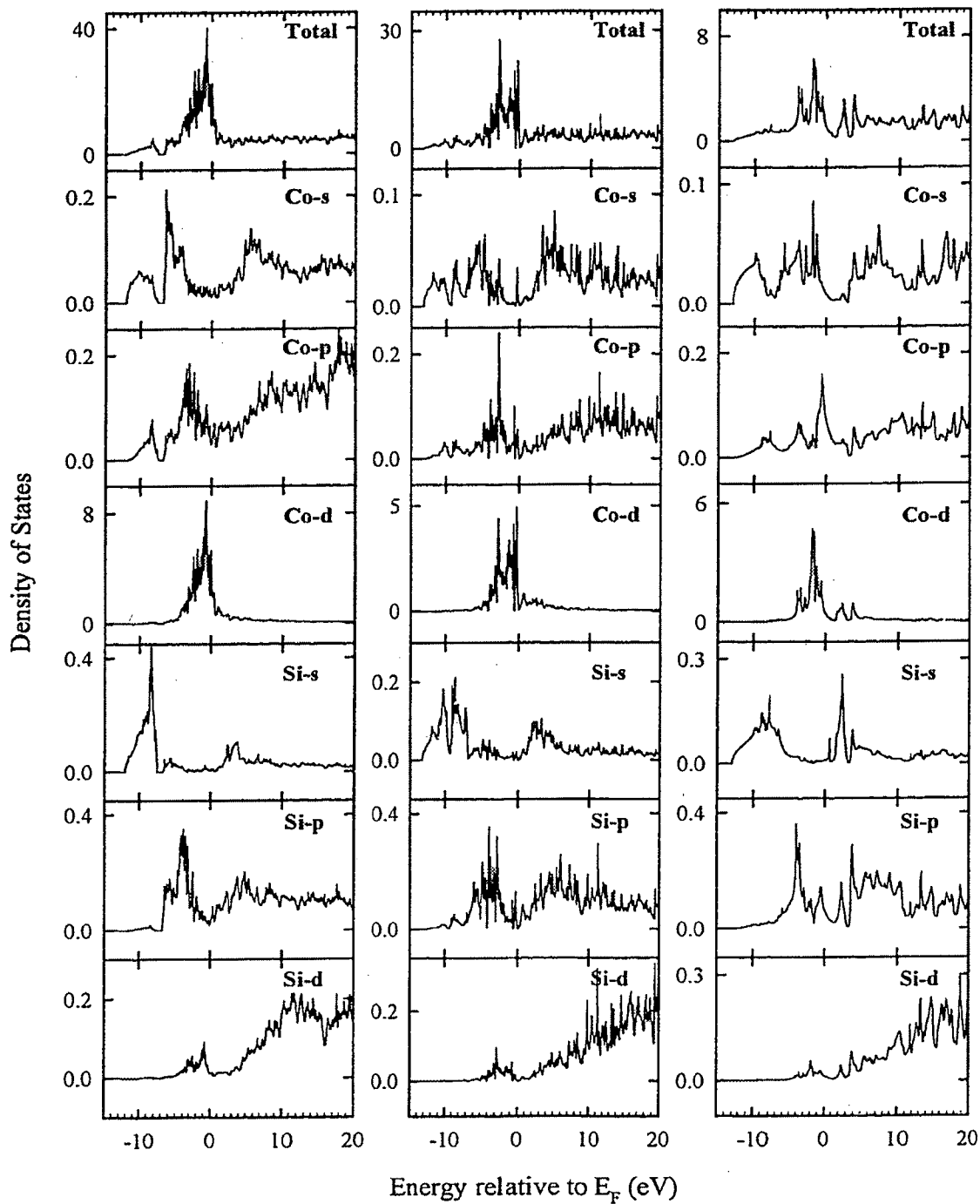
Figure 4.18. Calculated total and partial densities of states for Co_2Si, $CoSi$ and $CoSi_2$.

compounds for which no standard was available. To investigate the origins of the spectral features and possibly help identify compounds, calculations of X-ray absorption spectra were carried out using the LAPW package WIEN97 [42].

The resulting DOS for $CoSi_2$, CoSi, and Co_2Si are shown in Figure 4.18. The results compare favourably with those in the literature for $CoSi_2$ [21].

Using these DOS the X-ray absorption spectra were calculated for both the K and L-edges of both Si and Co. After the X-ray absorption spectra have been calculated from the DOS and the appropriate matrix elements, they are broadened by convolution with a Gaussian which represents the instrumental resolution. The width of this Gaussian was estimated (from approximate total spectral resolutions seen in the data) as 0.15 eV, 0.8 eV, 0.6 eV and 1.5 eV for the Si L, Co L, Si K and Co K-edges respectively.

The results of the calculations for $CoSi_2$ are shown in Figure 4.19 along with the spectra from the films, which have been aligned to the point of inflection of the edge, and the unbroadened spectra. The comparison with the experimental spectra shows that the calculations reproduce the features of the spectra near the edge well, although the intensity of the resonances is somewhat off, with increasing error farther from the edge. Some of these discrepancies were accounted for by P. Lerch *et al.* [21] and P. J. W. Weijs *et al.* [19] by including the relaxation of the core hole in their calculations. Perhaps the most interesting edge is the Si $L_{3,2}$-edge which had intense sharp features and a broad feature at the Fermi level. These features are reproduced well in the calculated spectrum. It can be seen by comparing the unbroadened spectra and the Si unoccupied d-, and s-DOS that the sharp features result from localized features of d-character while s-DOS accounts for the broad absorption just above the Fermi level.
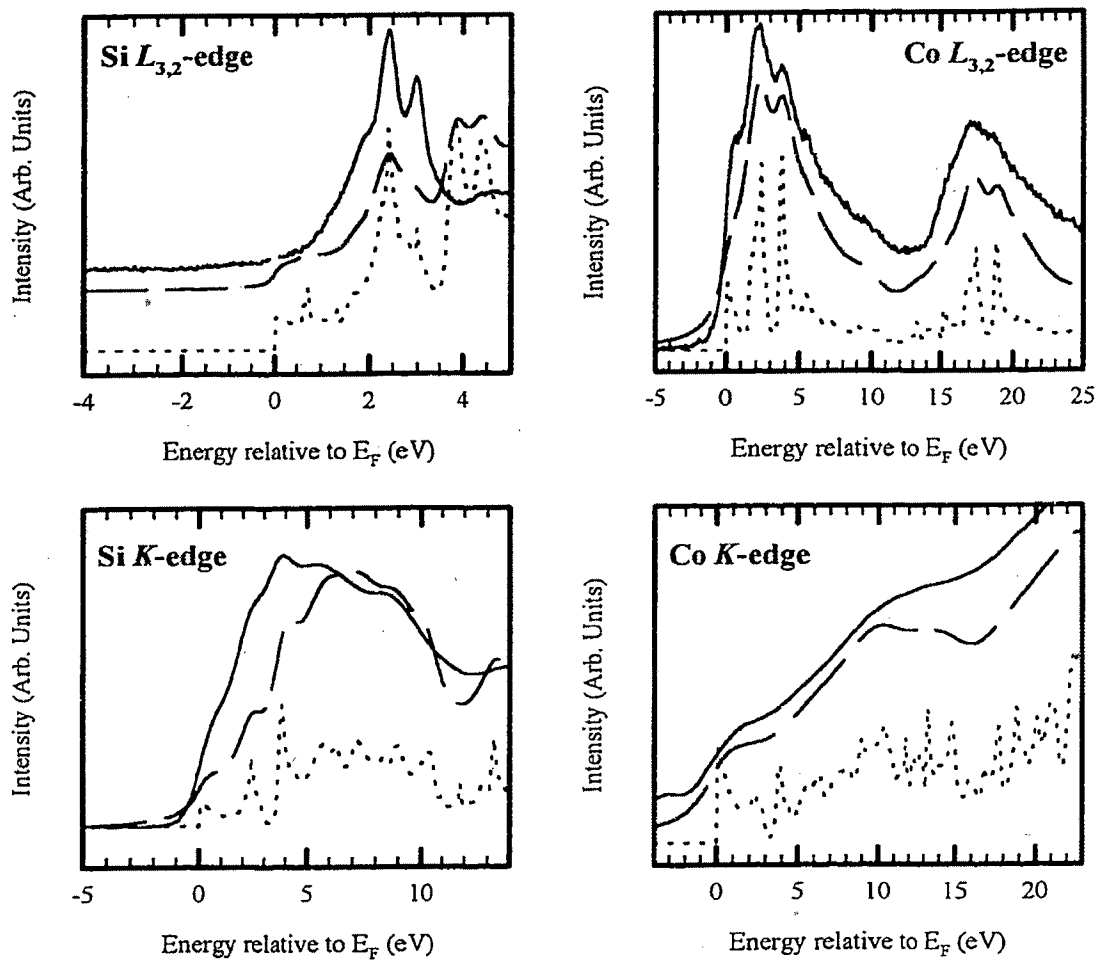
Figure 4.19. Comparisons of $CoSi_2$ data and calculations. (____) Data, (_ _ _) Calculated spectra and (......) Unbroadened spectra.

4.7 REFERENCES

[1] S. P. Murarka, *Silicides for VLSI Applications* (Academic Press, New York, 1983).

[2] K. N. Tu and J. W. Mayer, in *Thin Films: Interdiffusion and Reactions*, eds. J. M. Poate, K. N. Tu and J. W. Mayer (Wiley-Interscience, New York, 1978), Ch. 10.

[3] S. P. Murarka and M. C. Peckerar, *Electronic Materials: Science and Technology* (Academic Press, Boston, 1989), Ch. 6.

[4] G. Ottaviani, J. Vac. Sci. Tech. **16**, 1112 (1979).

[5] E. G. Colgan, J. P. Gambino and Q. Z. Hong, Mater. Sci. Eng. **R16**, 43 (1996).

[6] V. E. Burisenko and P. J. Hesketh, *Rapid Thermal Processing of Semiconductors* (Plenum Press, New York, 1997), Ch. 5.

[7] J. P. Gambino and E. G. Colgan, Mater. Chem. and Phys. **52**, 99 (1998).

[8] C. M. Osburn, Q. F. Wang, M. Kellam, C. Canovai, P. L. Smith, G. E. McGuire, Z. G. Xiao and G. A. Rozgonyi, Appl. Surf. Sci. **53**, 291 (1991).

[9] F. Deng, R. A. Johnson, P. M. Asbeck, S. S. Lau, W. B. Dubbelday, T. Hsiao and J. Woo, J. Appl. Phys. **81**, 8047 (1997).

[10] K. Maex, Mater. Sci. Eng. **R11**, 53 (1993).

[11] K. Maex, Appl. Surf. Sci. **53**, 328 (1991).

[12] K. Maex and M. Van Rossum, eds., *Properties of Metal Silicides* (Inspec, London, 1995).

[13] J. Chen, J.-P. Colinge, D. Flandre, R. Gillon, J. P. Raskin and D. Vanhoenacker, J. Electrochem. Soc. **144**, 2437 (1997).

[14] S. Mantl, Mater. Sci. Rep. **8**, 1 (1992).

[15] H. von Känel, Mater. Sci. Rep. **8**, 193 (1992).

[16] E. Z. Kurmaev, V. R. Galakhov and S. N. Shamin, Crit. Rev. Solid State Mater. Sci. **23**, 65 (1998).

[17] *Binary Alloy Phase Diagrams*, eds. T. B. Massalski, J. L. Murray, L. H. Bennett and H. Baker (American Society for Metals, Metals Park, 1986), pg. 801.

[18]   C.-H. Jan, C.-P. Chen and Y. A. Chang, J. Appl. Phys. **73**, 1168 (1993).

[19]   P. J. W. Weijs, M. T. Czyżyk, J. F. van Acker, W. Speier, J. B. Goedkoop,
        H. van Leuken, H. J. M. Hendrix, R. A. de Groot, G. van der Laan,
        K. H. J. Buschow, G. Wiech and J. C. Fuggle, Phys. Rev. B **41**, 11899 (1990).

[20]   W. F. Pong, Y. K. Chang, R. A. Mayanovic, G. H. Ho, H. J. Lin, S. H. Ko,
        P. K. Tseng, C. T. Chen, A. Hiraya and M. Watanabe, Phys. Rev. B **53**, 16510
        (1996).

[21]   P. Lerch, T. Jarlborg, V. Codazzi, G. Loupias and A. M. Flank, Phys. Rev. B **45**,
        11481 (1992).

[22]   S. Eisebitt, T. Böske, J.-E. Rubensson, W. Eberhardt, Phys. Rev. B **47**, 14103
        (1993).

[23]   S. Eisebitt, J.-E. Rubensson, T. Böske and W. Eberhardt, Phys. Rev. B **48**, 17388
        (1993).

[24]   S. Eisebitt, T. Böske, J.-E. Rubensson, J. Kojnok, W. Eberhardt, R. Jebasinski,
        S. Mantl, P. Skytt, J.-H. Guo, N. Wassdahl, J. Nordgren and K. Holldack, Phys.
        Rev. B **48**, 5042 (1993).

[25]   G. Rossi, A. Santaniello and P. De Padova, Solid State Com. **73**, 807 (1990).

[26]   P. Villars and L. D. Calvert, eds., *Pearson's Handbook of Crystallographic Data
        for Intermetallic Phases*, 2nd ed. (ASM International, Materials Park, OH, 1991).

[27]   U. Gottlieb, F. Nava, M. Affronte, O. Laborde and R. Madar, in *Properties of
        Metal Silicides*, eds. K. Maex and M. Van Rossum (Inspec, London, 1995), p.
        189.

[28]   M. Saran and A. Naem, J. Electrochemical Soc. **142**, 1688 (1995).

[29]   For a general review of photon detectors see: J. A. R. Samson, *Techniques of
        Vacuum Ultraviolet Spectroscopy* (Wiley, New York, 1967).

[30]   W. T. Elam, J. P. Kirkland, R. A. Neiser and P. D. Wolf, Phys. Rev. B **38**, 26
        (1988).

[31]   R. A. Rosenberg, J. K. Simons, S. P. Frigo, K. Tan and J. M. Chen, Rev. Sci.
        Instrum. **63**, 2193 (1992).

[32]   M. Kasrai, Z. Yin, G. M. Bancroft and K. H. Tan, J. Vac. Sci. Tech. A **11**, 2694
        (1993).

[33] M. Kasrai, W. N. Lennard, R. W. Brunner, G. M. Bancroft, J. A Bardwell and K. H. Tan, Appl. Surf. Phys. **99**, 303 (1996).

[34] T. Böske, W. Clemens, C. Carbone and W. Eberhardt, Phys. Rev. B **49**, 4003 (1994).

[35] S. J. Naftel, I. Coulthard, T. K. Sham, S. R. Das and D.-X. Xu, Phys. Rev. B **57**, 9179 (1998).

[36] R. E. Watson, J. Hudis and M. L. Perlman, Phys. Rev. B **4**, 4139 (1971).

[37] G. W. Rubloff, Surf. Sci. **132**, 268 (1983).

[38] F. M. d'Heurle, A. Cros, R. D. Frampton and E. A. Irene, Phil. Mag. B **55**, 291 (1987).

[39] K. Prabhakaran and T. Ogino, Appl. Surf. Sci. **121/122**, 213 (1997).

[40] S. J. Naftel, I. Coulthard, T. K. Sham, D.-X. Xu, L. Erickson and S. R. Das, Thin Solid Films **308-309**, 580 (1997).

[41] I. Coulthard, T. K. Sham, M. Simard-Normandin, M. Saran and J. D. Garrett, J. Phys. IV France 7, C2-1135 (1997).

[42] P. Blaha, K. Schwarz and J. Luitz, **WIEN97**, Vienna University of Technology 1997. (Improved and updated Unix version of the original copyrighted WIEN-code, which was published by P. Blaha, K. Schwarz, P. Sorantin and S. B. Trickey, Comput. Phys. Commun. **59**, 399 (1990)).

CHAPTER 5: NICKEL SILICIDE THIN FILMS[†]

5.1   INTRODUCTION

Like any metal whose silicides have properties that make them suitable for use in semiconductor device manufacture, the Ni-Si system has been heavily studied (for reviews see [1][2][3][4][5][6][7]). The self aligned silicidation process [7][8][9] (SALICIDATION), in which the solid state reaction of a deposited metal film with a silicon substrate is thermally induced, is the process used to make interconnects with low resistance to the source, drain and gate in modern metal-oxide-semiconductor (MOS) devices (Figure 1.2). The most commonly used metal for this purpose is Ti [6][10]. Recently, however, it has been found that as the lateral dimensions of devices shrink below submicron widths, the resistivity of the $TiSi_2$ films increases due to the retardation of the phase transition from the high resistivity C49 phase to the low resistivity C54 phase [11][12][13][14].

NiSi has been found to maintain its low resistivity down to the 0.1 μm feature size [12] and has thus recently been proposed as a suitable replacement to $TiSi_2$ in submicron technologies [6][12][15]. NiSi has several advantages over $CoSi_2$, whose resistivity is also relatively insensitive [6] to feature width. The main advantage is that less silicon is consumed in the production of NiSi, hence there is less risk of the silicide formed

---

[†]Portions of this chapter have been published:
a) S. J. Naftel, I. Coulthard, T. K. Sham, D.-X. Xu and S. R. Das, Thin Solid Films **308-309**, 580 (1997).
b) S. J. Naftel, I. Coulthard, T. K. Sham, S. R. Das and D.-X. Xu, Phys. Rev. B **57**, 9179 (1998).
c) S. J. Naftel, I. Coulthard, T. K. Sham, D.-X. Xu, L. Erickson and S. R. Das, Appl. Phys. Lett. **74**, 2893 (1999).
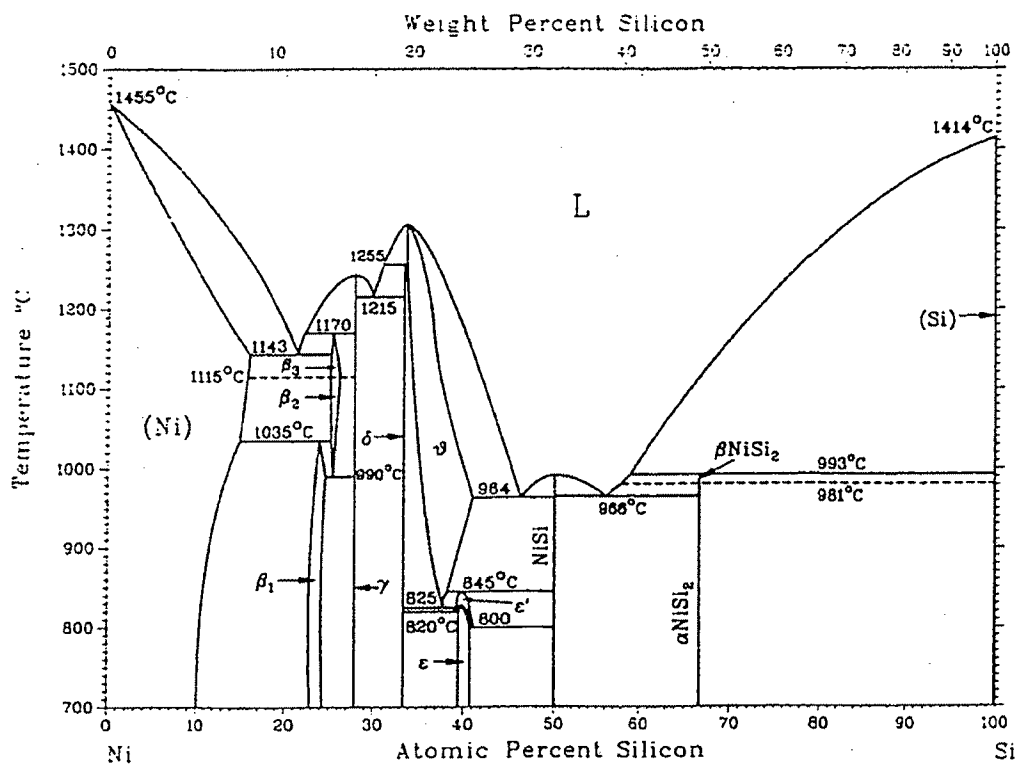
Figure 5.1. The Ni-Si phase diagram. (From T. B. Massalski [16], used with permission)
Note: β_1 - β_3 correspond to Ni_3Si, δ and ϑ correspond to Ni_2Si,
γ corresponds to $Ni_{31}Si_{12}$ or (Ni_5Si_2) and ϵ corresponds to Ni_3Si_2.

penetrating through shallow junctions [12]. NiSi also has a low formation temperature (~ 450 °C), an extended thermal stability range (450 - 700 °C) [3][12] and a sheet resistance comparable to $CoSi_2$ and $TiSi_2$ [7][12]. The main disadvantage with NiSi is that it is thermodynamically unstable on Si, the much higher resistivity $NiSi_2$ being the stable phase above 700 °C [5][7][10]. Thus, high temperature heat treatments are not possible after NiSi formation and the formation temperature must be carefully controlled.

Nickel and silicon form six stable compounds in the bulk as seen in the phase diagram (Figure 5.1). However, only three of these can be detected when thin films of Ni are heated on a silicon surface to form a silicide thin film. Similar to Co, the Ni initially reacts to form a Ni_2Si film, at about 250 °C, which grows until all the Ni deposited has reacted. At about 350 °C the NiSi phase starts to form. At higher temperatures the silicon rich final phase, $NiSi_2$, forms. $NiSi_2$ becomes the only phase present above 800 °C [3][7].

$$Ni \rightarrow Ni_2Si \rightarrow NiSi \rightarrow NiSi_2 \qquad (5.1)$$
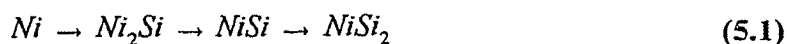
The sequence of phases is the same whether the film is processed in a standard furnace or if RTA is done [5]. Ni_2Si has been recently observed to nucleate at room temperature [17].

Table 5.1 lists the crystal structures and lattice parameters for all the thin film silicide phases along with other important parameters. All the silicides are metallic in character with low resistivities [18].

Few studies of the X-ray absorption of Ni silicides have been done (see Table 5.1). Mostly the band structures and absorption spectra of $NiSi_2$ have been calculated and reported. The other silicides have received much less attention, P. J. W. Weijs *et al.* [19] have reported the Si K-edge XANES of NiSi while U. del Pennino *et al.* [20] and others have reported the Ni L-edge XANES of Ni_2Si.

In this study, the aim is to follow the differences in the electronic and physical structure of nickel silicide thin films with various preparation conditions. X-ray absorption

near-edge structure spectroscopy will be used to investigate the electronic changes throughout the full depth of the films. In order to accomplish this, the variations in the sampling depth of XANES at different edges and detection techniques (Table 2.1) are capitalised on. This multi-core and multi-detection technique allows the films to be investigated from the perspective of the Ni, and of the Si, over a range of depths from the surface to the bulk. The XANES spectra taken together provide an accurate, non-destructive look at the morphology of the thin films.

Table 5.1. Important properties of the nickel silicides.

Ni Silicide	Crystal Struct.[a]	Resistivity (μohm-cm)[b]	Formation Temp. (°C)[c]	nm of Final Silicide per nm of Ni[d]	XAS edge and Ref.
Ni_2Si	ortho., Co_2Si a=4.99 Å b=3.72 Å c=7.06 Å	24	200-250	1.52	Ni L [20][21][22]
NiSi	ortho., MnP a=5.233 Å b=3.258 Å c=5.659 Å	14-20	350-650	2.34	Si K [19]
$NiSi_2$	cubic, CaF_2 a=5.406 Å	35-50	700-800	3.63	Ni K [23] Ni L [22][23] Si K [19][23]

[a]From P. Villars and L. D. Calvert [24], ortho. = orthorhombic.
[b]From U. Gottlieb et al. [18] and J. P. Gambino et al. [7].
[c]Compiled from [2][3][5][7].
[d]From S. P. Murarka [1].

5.2   SAMPLES

For this study a set of Ni-Si films was obtained from S. R. Das at The National Research Council, Ottawa, Canada. Ni films, of a thickness of 50 nm, were sputter-deposited onto chemically clean, n-type Si(100) single crystal wafers in an Ultra High Vacuum (UHV) magnetron sputtering system. After deposition, the Ni films were annealed *ex-situ*, in an RTA system, at successively higher temperatures in a dry N_2 ambient. Details of the cleaning process and the sputter-deposition system and process have been described previously [14]. A nickel foil was used to obtain pure Ni spectra. The preparation conditions of the samples are summarized in Table 5.2.

Table 5.2. Description of the preparation conditions of the nickel silicide thin film samples.

Sample	Description
Ni-Si (1)	Ni (50 nm) film, not annealed.
Ni-Si (2)	Ni (50 nm) film, annealed 300 °C/30 sec.
Ni-Si (3)	Ni (50 nm) film, annealed 300 °C/30 sec, 350 °C/30 sec, 400 °C/30 sec, then 500 °C/30 sec.
Ni-Si (4)	Ni (50 nm) film, annealed 300 °C/30 sec, 350 °C/30 sec, 400 °C/30 sec, then 850 °C/30 sec.

All specimens were degreased by washing with methanol before introduction into the various vacuum systems. No attempt was made to remove the native oxide from the thin films. The Ni foil was mechanically scraped with a diamond file to remove the majority of the oxide before introduction into the experimental chamber.   A cartoon of the expected basic structure of the thin film samples, before and after annealing, is presented in Figure 5.2.

What structural changes occur under the preparation conditions listed above is the question that we want to answer using XANES.

Approximate sampling depths

As deposited

Si *L*   Ni *L*   Si *K*   Ni *K*
T F   T F   T F   T F

After RTA

Ni —| ↕ ~50 nm

T-TEY
F-FLY

Si Substrate—

~150 nm

—SiO₂

—NiSi₂

—Si Substrate
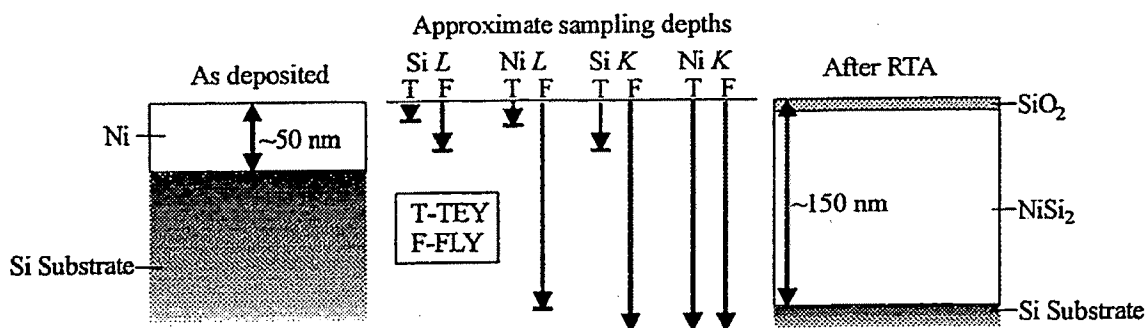
Figure 5.2. Schematic of the basic nickel silicide thin film structure before and after annealing.

5.3   EXPERIMENT

The experiments were carried out at four locations using three different experimental arrangements.

The Ni K-edge spectra were measured using beamline X-11A at the National Synchrotron Light Source (NSLS) located at Brookhaven National Lab. This beamline is equipped with a Si(111) double-crystal monochromator. The spectra were obtained in Total Electron Yield (TEY) mode using a He amplified total electron yield detector [25]. During some experiments an Ar filled ionization chamber detector [26] was used to obtain Fluorescence yield (FLY) spectra simultaneously. Standard ionization chambers [26] were used to measure the incident photon intensity (I_0). The monochromator was detuned 30 % during experiments in order to decrease contributions form higher harmonics. The sample was aligned to the beam by using pieces of photographic paper mounted in the same place as the samples. Figure 4.3 (page 84) depicts the experimental setup and the detectors utilized.

The Si K-edge spectra were measured using the soft X-ray Canadian Double-Crystal monochromator (DCM) beamline of the Canadian Synchrotron Radiation Facility (CSRF) located at the Synchrotron Radiation Centre (SRC) of the University of Wisconsin-Madison. The DCM is equipped with InSb(111) crystals. The incident photon intensity was measured using a N₂ filled ionization chamber isolated from the beamline vacuum by beryllium windows. Total electron yield spectra were obtained by measuring

the sample current to ground. A wire loop was placed in front of the sample, so as not to interfere with the incident light, and held at +135 V to help pull low kinetic energy electrons away from the sample. The vacuum system could also be equipped with a channel plate FLY detector [27][28] placed at 90° to the incident beam in the plane of the ring (Figure 4.4, page 86).

The samples were mounted on stainless steel disks using double sided carbon tape which provided suitable electrical contact. Up to five disks could be mounted onto the manipulator at one time. The manipulator was aligned to the incident beam using a sixth disk coated in phosphor. Once the manipulator was aligned all the mounted samples could be reproducibly moved into position with the beam. The samples could be rotated to change the angle of incidence but most measurements were made in normal incidence.

The Si L-edge spectra were measured on the Canadian Grasshopper monochromator beamline of the CSRF. The grasshopper was equipped with a 1800 groove/mm grating which has its best resolution and intensity around 100 eV making it ideally suited for measuring Si L-edge spectra. The experimental chamber used for these measurements was the same as that used for the Ni L-edge measurements.

The Ni L-edge spectra were measured on the High Resolution Monochromator (HERMON) beamline at SRC. HERMON was equipped with two variable line spacing plane gratings which can be changed easily without breaking vacuum in the beamline. The experimental chamber used in these measurements was equipped with a load-lock system which allowed a single sample to be introduced into the chamber without breaking the main chamber vacuum. The samples were again mounted on stainless steel disks with double sided carbon tape. TEY spectra were measured via the sample current, however, no additional voltage loop was present in this arrangement. The FLY spectra were again measured by a channel plate detector placed about 50° from the incident light and about 50° up out of the plane of the ring and sample. This detector position helps reduce interference from light reflected off the sample. The incident light intensity was measured in these cases by a Au mesh detector. The experimental setup is shown in Figure 4.5 (page 87) along with a schematic of the Au mesh I_0 monitor.

5.4   RESULTS AND DISCUSSION FOR THE NICKEL SILICIDE FILMS

5.4.1   Si $L_{3,2}$-edge spectra

The Si $L_{3,2}$-edge spectra, taken in total electron yield mode (TEY), for the Ni-Si films as well as a Si(100) crystal are shown in Figure 5.3. As noted previously (Chapter 2), the one absorption length above the Si $L_{3,2}$-edge photon energy (100 eV) is approximately 40 nm. This penetration depth is comparable to the initial Ni film thickness before annealing. Using TEY limits the sampling depth at this edge to a maximum of about 5 nm (Table 2.1), thus, the spectra shown represent the electronic structure of the Si atoms at the surface of the films.

The Si $L_{3,2}$-edge arises from excitation of electrons in the Si 2p core levels. The near-edge structures originate from the allowed p→s or d transitions. The Si 2p level is spin-orbit split into the $2p_{3/2}$ and $2p_{1/2}$ states with a separation of 0.6 eV. Transitions originating from these levels give rise to doublet structures in Si $L_{3,2}$-edge spectra separated by 0.6 eV. This doublet feature can be seen in the Si $L_{3,2}$-edge spectra of a Si(100) wafer shown as the bottom spectrum in Figure 5.3.

All the Si L-edge spectra shown have had a linear pre-edge background removed. The Si(100) spectra threshold energy was used as a standard for the calibration of the edge energies. An overall resolution of ~300 meV was obtained using the 1800 groove/mm grating and 30 μm slits in the grasshopper.

The Si(100) spectra shown in Figure 5.3 consists of two distinct edges separated by about 5 eV. The first edge originates from the Si in the Si(100) environment while the second, at about 105 eV, originates from the Si in SiO_2. Silicon naturally oxidizes in the ambient atmosphere to form a surface layer of SiO_2 and this is the origin of this second edge. This separation of the Si and SiO_2 edges is an important feature of the Si $L_{3,2}$-edge. Because the separation of 5 eV is significantly larger than the core hole lifetime broadening of the Si near-edge features, the Si spectrum, free of oxide features, can be studied without removing the surface oxide so long as the oxide thickness does not exceed
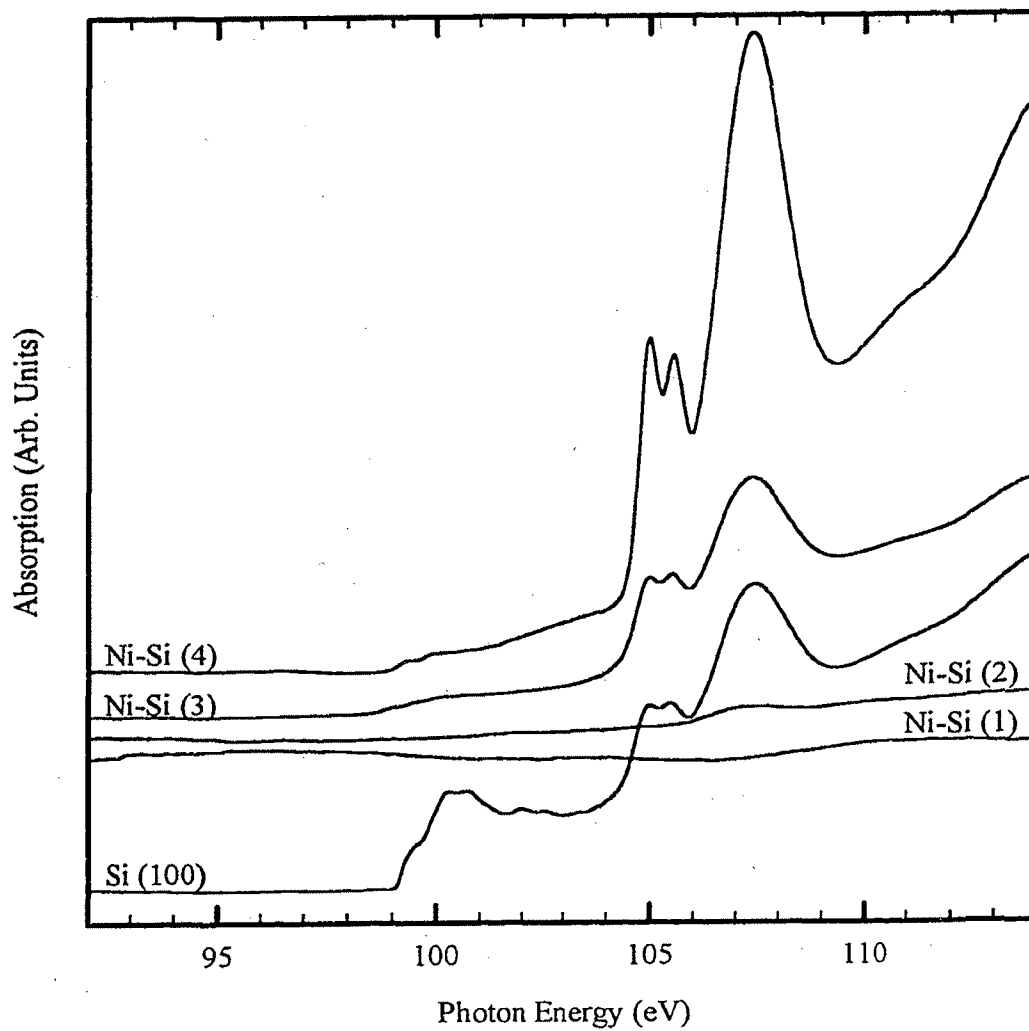
Figure 5.3. Si $L_{3,2}$-edge spectra XANES spectra of the Ni-Si films and Si(100) taken in TEY mode.

the sampling depth. This convenient feature allows us to study the Si $L_{3,2}$-edge XANES of the Ni-Si films without removing the native oxide.

The TEY spectra of the Ni-Si films at first glance appear uninteresting, showing almost no signal in the silicide region. A slight signal can be seen in the silicide region for the high temperature annealed films ((3) and (4)). The lack of a signal in this area for the as-deposited and lightly annealed films is hardly surprising as the sampling depth is insufficient to penetrate the 50 nm Ni overlayer present in these samples.

For the high temperature annealed films there is some signal present in the silicide region of the spectra. This indicates that the silicon and nickel have reacted to form some silicide throughout the thickness of the film so that some Si atoms are now visible within the TEY sampling depth. The oxide features indicate the presence of surface SiO_2 on these films.

The fluorescence yield (FLY) spectra are shown in Figure 5.4. The dramatic change in the sampling depths (now between 25 and 70 nm, Table 2.1) between TEY and FLY is immediately apparent in the high temperature annealed films ((3) and (4)). The unannealed and lightly annealed films still show flat lines in the silicide region, indicating that silicon atoms do not interact enough to penetrate the Ni film far enough to be seen by FLY. The spectrum of Ni-Si (3) now shows features arising from NiSi. The spectrum of Ni-Si (4) film shows a unique spectrum arising from the $NiSi_2$ formed during the annealing process. Quite clearly the spectral features for both films are distinct. The assignment of the spectra of the films to NiSi and $NiSi_2$ is based on the expected outcome of the preparation conditions for the films [14].

It is interesting to compare the spectra of $NiSi_2$ with that of $CoSi_2$ (Figure 4.8). Both spectra have distinct sharp features which relate to the localized density of unoccupied Si s and d-states. The similarity of the spectra and thus the DOS of $NiSi_2$ and $CoSi_2$ is understandable as both compounds have the same crystal structure.

It is also clear from the FLY spectra in Figure 5.4 that there is a shift in the threshold energy (E_0) between the silicides and Si(100). The largest shift is exhibited by NiSi which shifts to lower photon energy by 0.50 ± 0.05 eV. The threshold energy in
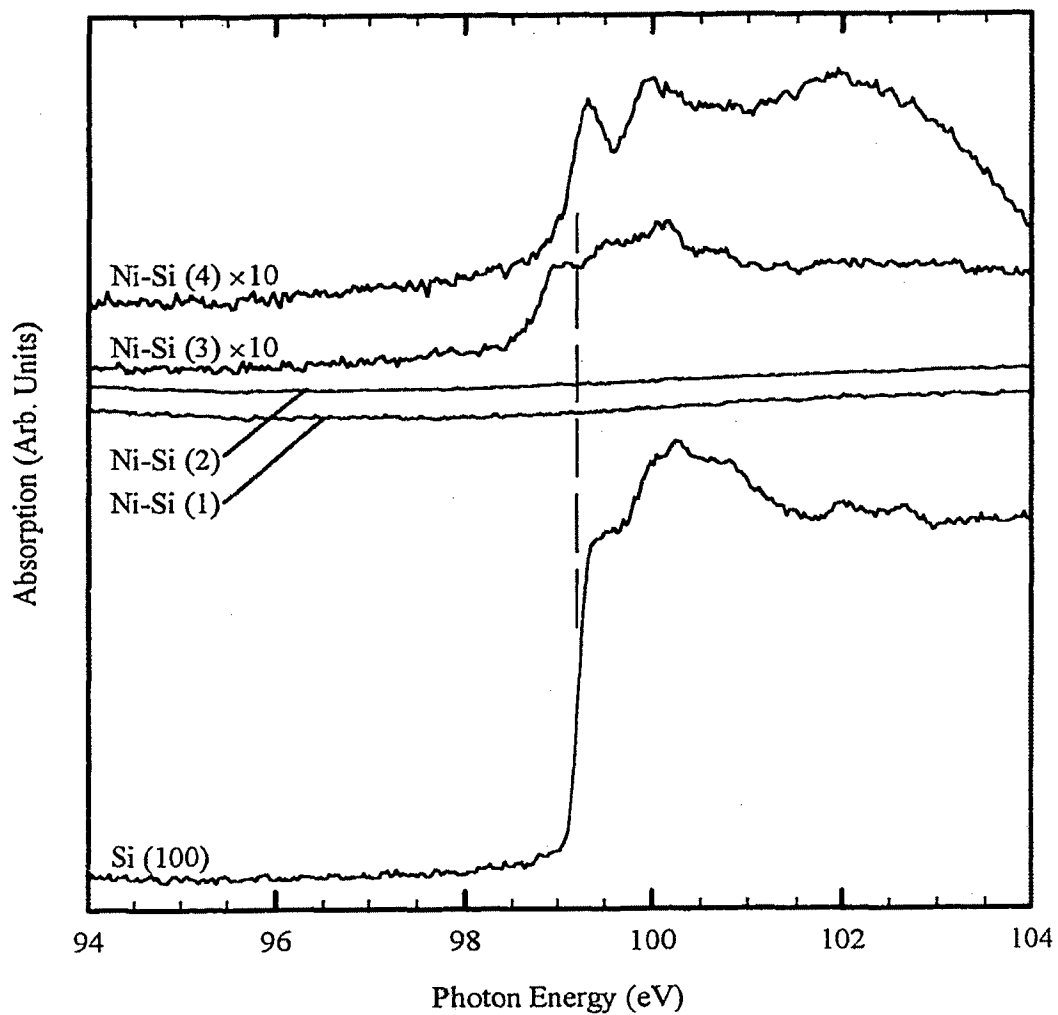
Figure 5.4. Si $L_{3,2}$-edge spectra of the Ni-Si films and Si(100) taken in FLY mode. The vertical line indicates the Si L-edge threshold position.

$NiSi_2$ is observed to shift in the same direction but by only 0.10 ± 0.05 eV. To a first approximation a threshold energy shift in this direction, equivalent to a decrease in the binding energy of the Si 2p core level, indicates that Si is gaining charge in the silicides.

5.4.2 Ni $L_{3,2}$-edge spectra

In order to increase the bulk sensitivity and examine the structure of the films below their covering oxide layers, the Ni $L_{3,2}$-edge was studied. There are no Si core levels present in the energy range of the Ni L-edges, thus the spectra obtained represent the electronic structure relative to the Ni site. Using TEY detection the sampling depth at the Ni L-edges was estimated at a few tens of nm (minimum ~16 nm). The TEY XANES spectra of the Ni-Si films, and a Ni foil sample, after a linear pre-edge background are shown in Figure 5.5.

The XANES for the as-deposited and low temperature annealed films, Ni-Si (1) and Ni-Si (2) respectively, appear essentially the same as that of pure Ni metal. This clearly indicates that the dominant phase in these two films, in the surface and near surface regions, is indeed Ni metal as suggested by the Si L-edge XANES. The XANES of the other two films are distinctly different and exhibit threshold shifts to higher energies, corresponding to higher binding energy for the Ni 2p core levels. The NiSi (Ni-Si (3)) threshold shifts by 1.6 ± 0.1 eV while the $NiSi_2$ (Ni-Si (4)) shifts by 2.3 ± 0.1 eV. These threshold energy shifts initially indicate that Ni loses charge in forming the silicides.

The face value indication that Si gains charge while Ni loses charge is interesting in connection with electronegativity considerations. According to Pauling's scale Ni and Si have identical electronegativities suggesting little or no net charge transfer should occur. It should also be noted that the silicides are metallic in nature and should thus also obey electroneutrality considerations. Thus the apparent charge transfer should be viewed in terms of a charge redistribution. In the case of Ni and Si, the Ni d-d interaction is reduced on the dilution of Ni by Si (Ni has mainly Si nearest neighbours in the silicide crystal structures) which should favour a d→s rehybridization at the Ni site. Si favours a p→s
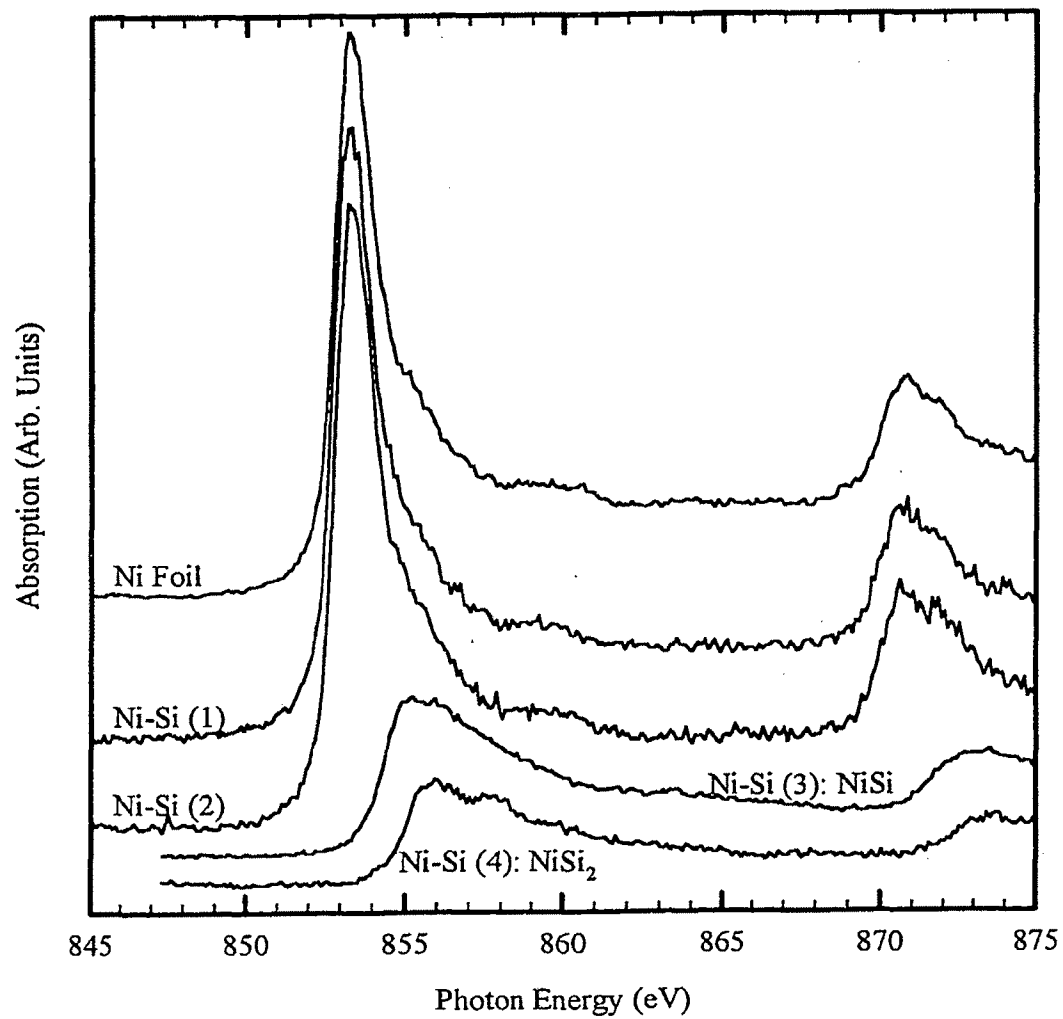
Figure 5.5. Ni $L_{3,2}$-edge spectra of the Ni-Si films and Ni foil taken in TEY mode.

rehybridization on silicide formation as the Si sp^3 hybridization is broken by interaction with the metal (Si has mainly Ni nearest neighbours).

In a charge redistribution situation, the observed threshold shifts are a product of not only the net charge transferred, off or on a site, but also of the type of charge (s, p or d) [29][30]. Hence, a reduction in the 3d charge count at the Ni site will increase the binding energy (threshold energy) of all the core levels even if the depletion is fully compensated for by a gain in s-charge. The reduction in d-charge dominates the binding energy shift because the d-charge is more compact and screens the nucleus better than the $4s$ charge (or in other words, the Coulomb interaction F(2p, 3d) is larger than F(2p, 4s)). At the Si site any change in hybridization will increase the s-character, relative to Si in bulk silicon, and hence the screening, leading to a negative binding energy shift.

The depletion of d-charge at the Ni site can be confirmed by examining the whiteline of the Ni L_3-edge XANES. The absorption at the L-edges involves the transition from the 2p core level to unoccupied densities of states of predominantly d-character [22]. A larger number of d-holes will lead to an increase in the whiteline area of the L-edge spectrum (Fermi's Golden rule [31]). Looking briefly at the silicide spectra in Figure 5.5 we see that the whiteline in the silicides is less intense but broader than the whiteline of pure Ni metal.

The whiteline areas of the silicides can be compared directly to that of Ni metal by normalizing the spectra to a unity edge-jump, aligning the spectra to the threshold energy and subtracting the Ni metal spectra from the spectra of the silicide. A negative peak in the resulting difference spectra indicates that the Ni metal spectra was more intense within that range of energies. A positive peak in the difference spectrum indicates that the silicide spectrum was more intense. If the total sum of the peak areas in the difference spectrum is positive, then the silicide whiteline is larger and the number of d-holes has increased in the silicide relative to the pure metal. The results of this procedure are shown in Figure 5.6 for both NiSi (Ni-Si (3)) and $NiSi_2$ (Ni-Si (4)). The area of the peaks in the difference spectra are indicated in the figure. Clearly in both cases the silicide whiteline area has increased over that of pure Ni metal, thus in both silicides the Ni site loses
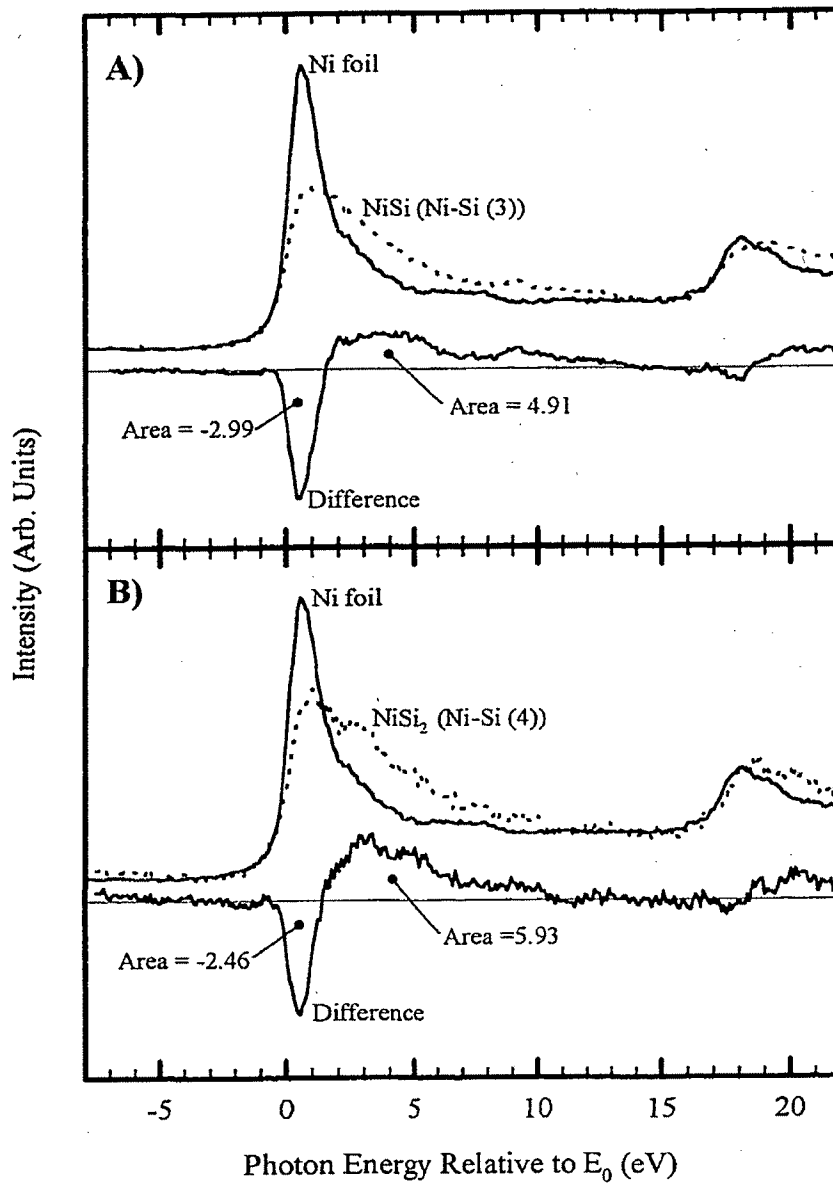
Figure 5.6. Ni L-edge whiteline difference curves between Ni foil and the nickel silicides. A) NiSi and B) NiSi$_2$

d-charge upon formation of the silicide.

The Ni $L_{3,2}$-edge XANES spectra of the Ni-Si thin films and a Ni foil, taken in FLY mode, are shown in Figure 5.7. All spectra have had a linear background removed. The sampling depth of FLY detection at this edge is estimated to be similar to the thickness of the silicide films (~200 nm). Notice that except for the Ni-Si (2) spectrum and the Ni foil, the XANES are apparently the same as for TEY. The similarity between the TEY and FLY spectra indicates that the chemical identity of the films is essentially the same throughout the film as it is in the near surface region.

The spectrum of the low temperature annealed film shows a noticeable drop in the intensity of the whiteline characteristic of Ni metal, accompanied by a broadening of the whiteline and a shift of the threshold energy to higher photon energy. The changes in the spectrum indicate that the low temperature anneal has induced some intermixing at the Ni-Si interface. The result of this intermixing may be the formation of a Ni-rich silicide possibly Ni_2Si [3].

The FLY spectrum of the Ni foil exhibits a reduced whiteline intensity compared to that in TEY. The intensity reduction is attributed to self-absorption effects, a feature which is typical of thick samples in FLY XANES measurements [32][33]. For thin films (see Ni-Si (1)) the thickness effect is not important.

5.4.3   Si *K*-edge spectra

At photon energies around the Si *K*-edge the incident X-rays penetrate well beyond the film thickness, thus the presence of signal originating from the substrate complicates the analysis of the XANES spectra.

Total electron yield detection is inherently surface sensitive. At the Si *K*-edge the TEY sampling depth is only about 40-70 nm (Table 2.1) which is similar to the thickness of the unannealed Ni film. Thus, TEY effectively minimizes the effect of the underlying Si substrate in the spectra. It should be noted that the substrate signal is only diminished for the high temperature annealed films (Ni-Si (3) and Ni-Si (4)) as the unannealed and low
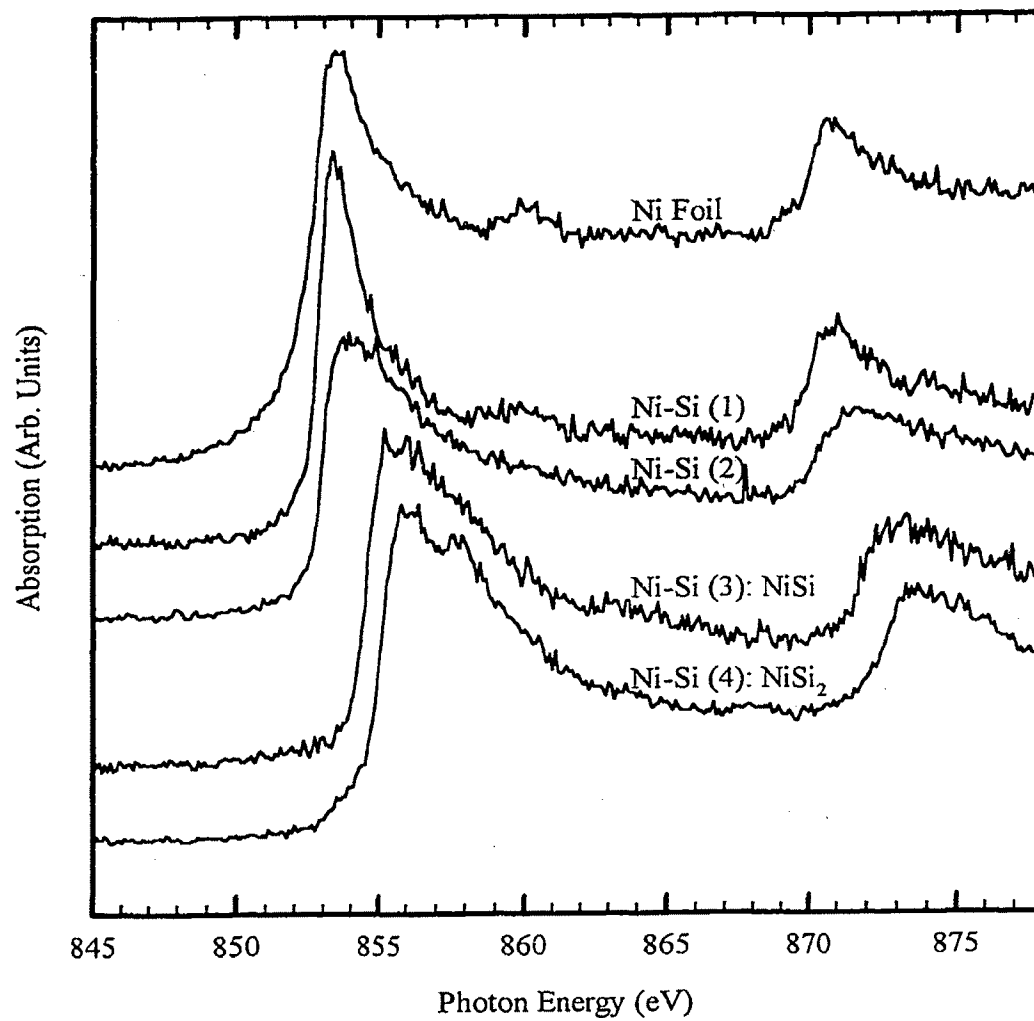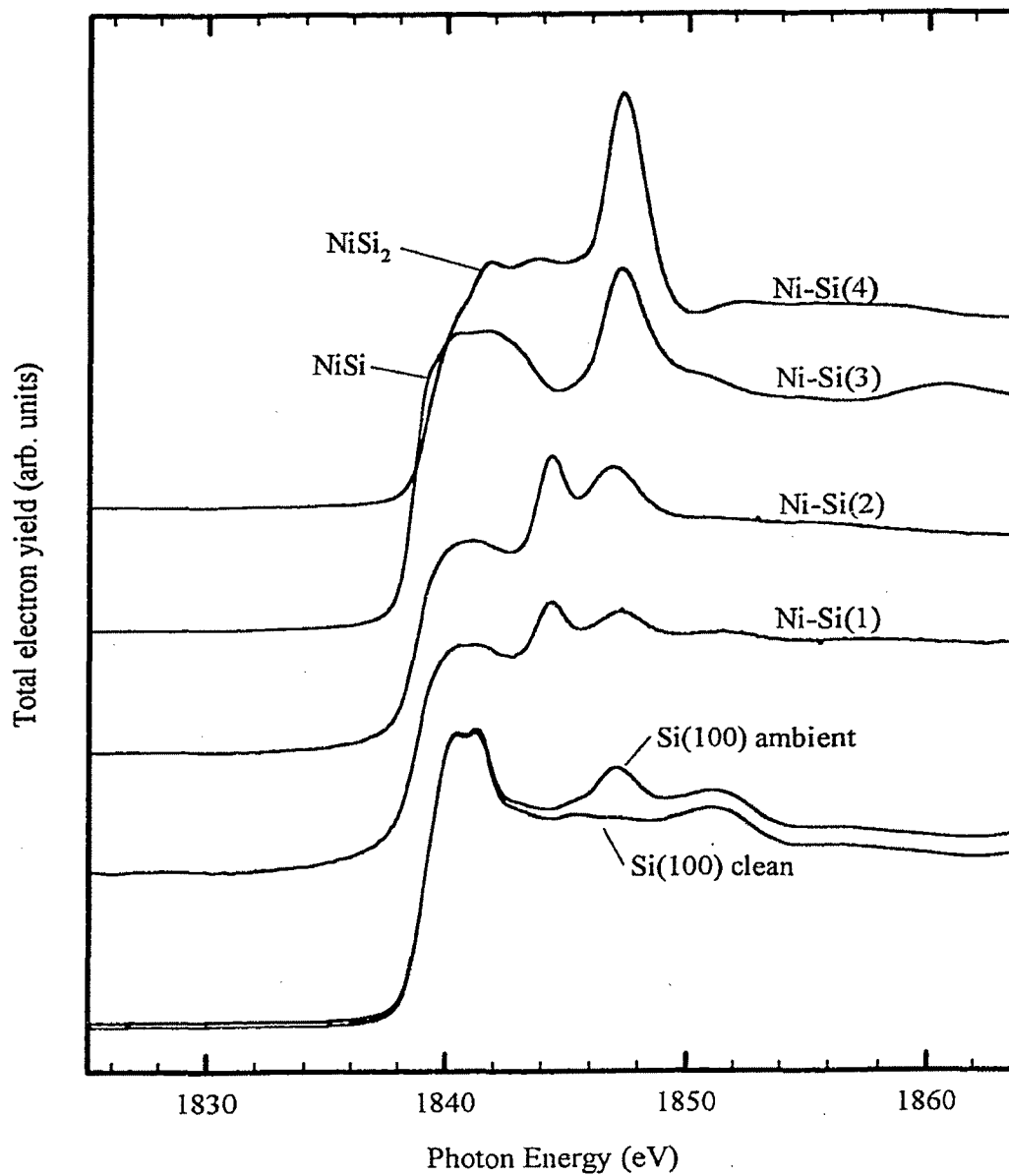
Figure 5.7. Ni $L_{3,2}$-edge spectra of the Ni-Si films and Ni foil taken in FLY mode.

Figure 5.8. Si *K*-edge spectra of the Ni-Si films, Ni foil, and both clean and ambient Si(100) taken in TEY mode.

temperature annealed films will still only have approximately 50 nm of Ni on Si(100) allowing TEY to sample the underlying substrate. Figure 5.8 shows the Si K-edge spectra taken in TEY mode for the Ni-Si films, ambient Si(100) and clean Si(100). All spectra have been normalized to an edge jump of unity after pre-edge background removal.

The Si K-edge XANES of the as-deposited film (Ni-Si (1)) and the film annealed to 300 °C (Ni-Si (2)) exhibit features significantly different from those of clean Si(100). There is a visible broadening of the characteristic whiteline doublet for crystalline silicon and two resonances at ~1844 eV and 1847 eV. A small shift in the threshold energy of ~0.4 eV, defined as the point of inflection of the rising edge, is also seen. The widening of the whiteline and blurring of the doublet indicate the presence of a new phase, probably a Ni-rich silicide, in which the long range Si-Si interaction which results in the whiteline doublet is disrupted as the result of Ni-Si interactions [34]. The new resonances (~1844 and ~1847 eV) must also originate from this Ni-rich phase which exists at the Ni-Si interface. As the Ni $L_{3,2}$-edge XANES already identified the bulk component of both films to be Ni this Ni-rich phase must be localized around the interface.

Since the films were prepared in an ultrahigh vacuum chamber and the surface was covered with 50 nm of Ni, the Si surfaces are well protected from oxidation. It is thus unlikely that the two resonances are of an oxide origin in the lightly annealed films Ni-Si (1) and Ni-Si (2). Besides which, SiO_2 exhibits a characteristic resonance at ~ 1847 eV and not at 1844 eV.

The intensities of both resonances increase on initial annealing, Ni-Si (2), without any other change in the spectral pattern and threshold energies. The intensity increases, thus indicate that further intermixing occurs without a phase change. This interfacial phase is likely to be a Ni-rich silicide (Ni_2Si) phase [17], but there is not enough information to determine the identity of the phase exactly.

As mentioned in Chapter 4 (pg. 103) the peak seen at ~1847 eV in the Si K-edge spectra arises mostly from SiO_2. The SiO_2 origin of this peak is clear from comparing the spectra of clean and ambient Si(100). The ambient Si(100) has a layer of SiO_2 formed on its surface by reaction with the ambient atmosphere. The difference between the two

Si(100) spectra is the peak at ~1847 eV. The oxide peak is also clear in the spectra of NiSi and NiSi$_2$. There is also a silicide peak which occurs at almost the same energy (~1847 eV) in the spectra of the unannealed and slightly annealed films (Ni-Si (1) and Ni-Si (2)), as discussed above. The slight shift in energy of the peaks located around 1847 eV indicates that there is in fact a difference between the peak at ~1847 eV in films (1) and (2) and the similar peak in films (3) and (4).

Annealing the films to higher temperatures induces significant changes in the spectra. For Ni-Si (3) the Si K-edge XANES exhibits a much wider whiteline and the pattern of the characteristic Ni-rich phase and crystalline silicon are no longer seen. A comparison of this spectrum with Si K-edge spectra for nickel silicides from the literature [19] (Figure 5.9A) shows that the film has been converted to NiSi with a covering of SiO$_2$, as expected from the formation conditions. The NiSi film spectrum exhibits a threshold shift of -0.6 ± 0.1 eV which is consistent with that observed at the Si L-edge.

For Ni-Si (4) the spectral features again change and comparison with literature spectrum [19] (Figure 5.9B) shows that the film has been converted to the final NiSi$_2$ phase with a covering of SiO$_2$, as expected. This phase exhibits no noticeable threshold shift at the Si K-edge.

5.4.4   Ni K-edge spectra

The Ni K-edge, corresponding to absorption of photons by the 1s electron of Ni, has a threshold energy of 8333 eV in pure Ni metal. At these energies the sampling depth for TEY and FLY are estimated to be ~300 nm and ~10 μm, respectively. With these estimates it is easy to see that in the case of the Ni K-edge, the sampling depth far exceeds the expected thickness of the final films. However, the actual sampling depth in this case is limited to the distribution of Ni in the sample since the X-ray absorption is site selective. The absorption of photons at the Ni K-edge by Si atoms only contributes to a smooth background.

The Ni K-edge spectra taken in TEY mode are shown in Figure 5.10. The spectra
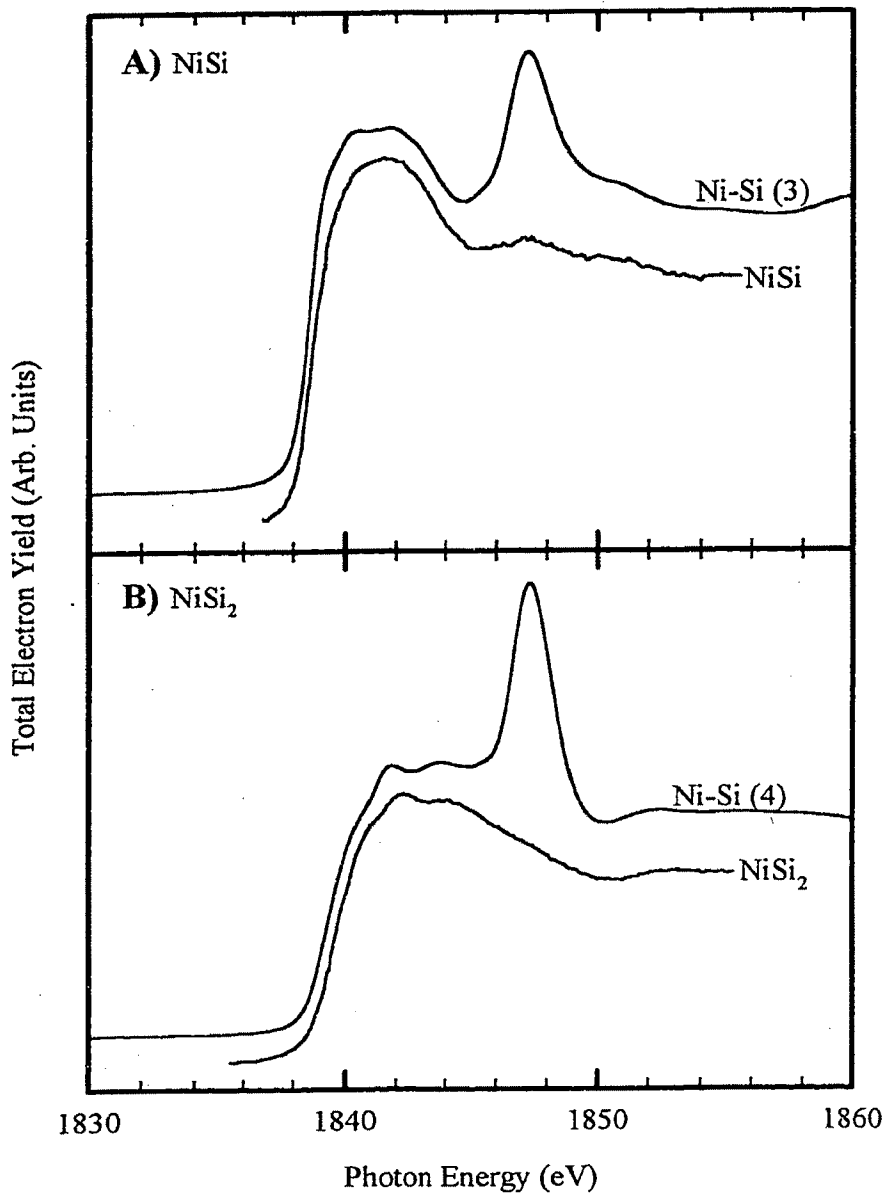
Figure 5.9. Si *K*-edge TEY spectra for nickel silicide film A) Ni-Si (3) and B) Ni-Si (4) and comparison with NiSi and NiSi$_2$ spectra taken from P. J. W. Weijs *et al.* [20].
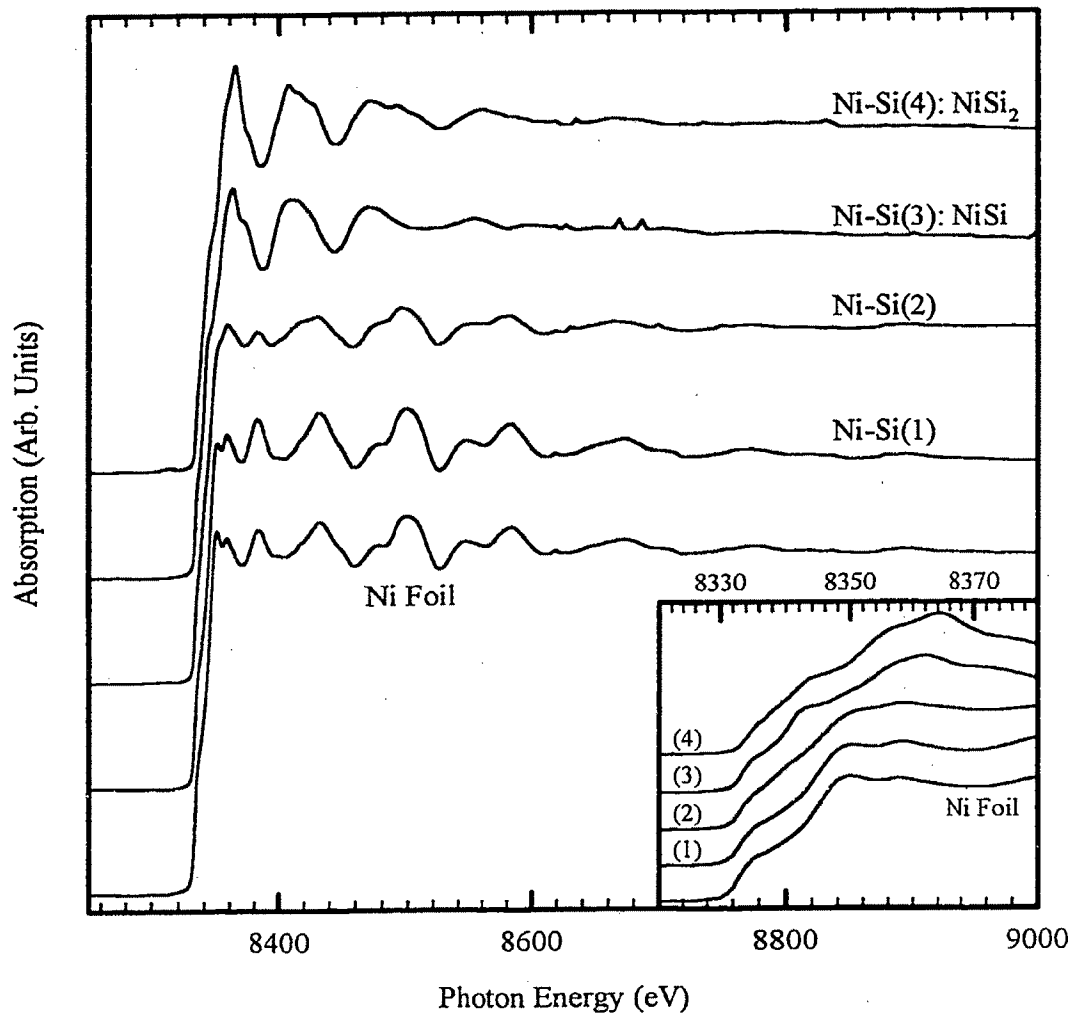
Figure 5.10. Ni *K*-edge spectra of the Ni-Si films and Ni foil taken in TEY mode. The inset shows the detail of the XANES region of the spectra.

have had a linear pre-edge background removed and then have been normalized to an edge jump of unity (edge jump is calculated from the pre-edge background to the atomic EXAFS background level).

The as-deposited spectra clearly exhibit X-ray absorption fine structures indistinguishable from that of Ni foil. This is hardly surprising as the spectrum of the Ni-rich phase seen at the other edges will be overpowered by the spectrum of the Ni over layers which have not reacted. The Ni K-edge spectrum for the modestly annealed film, Ni-Si (2), shows a noticeable reduction in amplitude and broadening of the spectrum. This indicates that the thickness of the intermixing region has increased as seen in the Si K and Ni L-edge results. A rough estimate based on the various sampling depths yields an upper bound to the thickness of the unreacted Ni layer of 30 nm.

Again annealing at higher temperatures causes significant changes in the XANES spectra. The NiSi film exhibits a threshold shift of 1.3 ± 0.2 eV to higher energies (higher binding energies) while the $NiSi_2$ spectra has a shift of 1.9 ± 0.2 eV to higher energies. The threshold shifts seen at the various edges studied are listed in Table 5.3, below.

Table 5.3. Measured X-ray absorption threshold shifts of NiSi and $NiSi_2$.

Silicide	X-ray Absorption Edge Threshold Shift (eV)			
	Si $L_{3,2}$-edge	Ni $L_{3,2}$-edge	Si K-edge	Ni K-edge
NiSi	-0.50 ± 0.05	1.6 ± 0.1	-0.6 ± 0.1	1.3 ± 0.2
$NiSi_2$	-0.10 ± 0.05	2.3 ± 0.1	0	1.9 ± 0.2

Clearly both silicon edges shift by the same amount within experimental error. The Ni K-edge however shifts to a lesser amount than the Ni L-edge in both silicides. Since neither the Ni 1s or 2p electrons are directly involved in bonding in the silicides the differences must arise from differences in the screening of these electrons by the 3d electrons. Since the decrease in the d-charge at the Ni site leads to a larger positive shift in the binding energy at the Ni L-edges than the Ni K-edges, the 3d electrons must screen

the 2p core levels better than the 1s core levels.

5.4.5   Conclusions

This study set out to investigate the structure of Ni-Si films, formed by standard thermal annealing processes used in industry using multi-core multi-detection XANES spectroscopy.

The samples obtained were made under slightly different preparation conditions but were expected to yield Ni-Si films of various compositions. It was found that the films followed the expected sequence of phase formation upon heating and that well formed films of NiSi and $NiSi_2$ were produced after appropriate annealing to 500 °C and 850°C, respectively (Figure 5.11).

For the unannealed film it was found that a reaction occurred at the Ni-Si interface even without annealing. This reaction developed further on light annealing to 300 °C so that a Ni-rich silicide phase, probably Ni_2Si, was seen to develop from the Ni-Si interface towards the surface of the film under a layer of unreacted Ni (Figure 5.11).
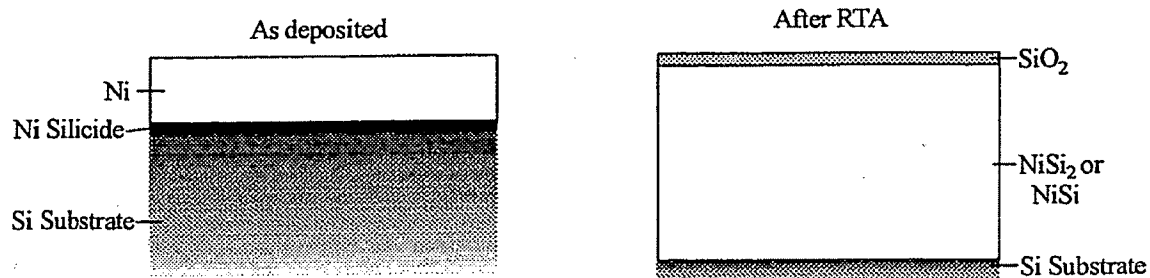
Figure 5.11. Schematic of the structure of the studied Ni-Si films.

For the high temperature annealed films we found:

1) The films were capped with SiO_2 layers, less than 5 nm thick due to selective oxidation of the films in the ambient atmosphere.

2) The bulk of the film annealed to 500 °C was indeed NiSi.

3) The bulk of the film annealed to 850 °C was the expected $NiSi_2$ phase.

Overall it was found that multi-core multi-detection XANES is well suited to the study of thin films and buried interfaces, particularly in the soft X-ray range. The study of the thin films also provides us with fingerprint spectra for NiSi and $NiSi_2$ at the Ni K, Ni L, Si K, and Si L-edges. This allows us to study more complicated structures of nickel silicides using XANES.

5.5   NICKEL SILICIDE LINES

5.5.1   Introduction

Metal silicide sub-micron lines have recently become an important subject for research. This is primarily due to the fact that as the dimensions of semiconductor devices shrink, components must scale down accordingly without losing their desired mechanical and electrical properties. Since it has been reported that for the commonly used silicide, $TiSi_2$, the resistance increases significantly as the lateral dimensions of the line shrink [11][12][13][14], the question of whether or not metal silicides with desirable properties can be prepared in sub-half-micron line widths must be addressed [12][15].

Reports that NiSi maintains its electrical integrity even for line widths down to 0.1 μm [12] have fuelled new scrutiny of the Ni-Si system for use in integrated circuit manufacture. As a continuation of the studies on Ni-Si blanket films two Ni-Si sub-half-micron line samples were obtained and studied using the Ni $L_{3,2}$-edge XANES.

5.5.2   Experiment

Nickel silicide sub-half-micron lines were prepared on n-type Si(100) substrate by D.-X. Xu and coworkers at the National Research Council (NRC), Ottawa, Canada. The lines were written with a focused ion beam and were equally spaced about 6 μm apart, covering an area of ~ 1 cm^2. The lines in the two samples studied had nominal line widths

of 0.15 μm and 0.2 μm. The initial metal thickness deposited was 15 nm. Sequential annealing (300°C/30 sec., 350 °C/30 sec., 400 °C/30 min.) was carried out in nitrogen ambient with the aim of forming NiSi lines. The lines have been studied with TEM and their electrical properties measured [15]. The TEM results show that under the preparation conditions used NiSi was formed. A schematic of the lines is shown in Figure 5.12.
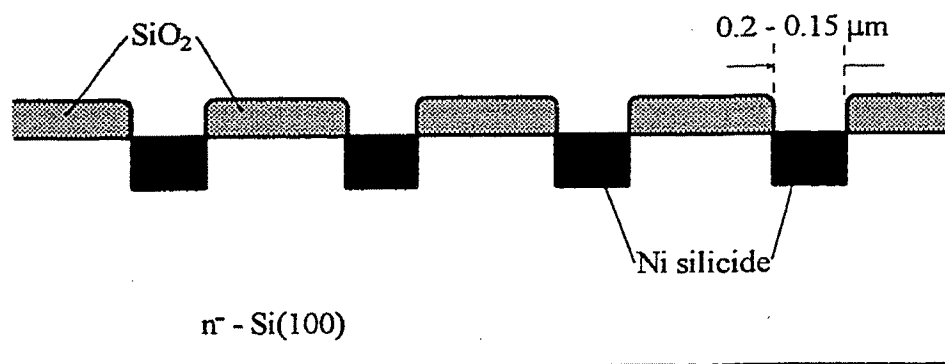
Figure 5.12 Schematic diagram of the silicide lines on Si(100).

The X-ray absorption measurements at the Ni $L_{3,2}$-edge were carried out at the high resolution monochromator beamline (HERMON) at the Synchrotron Radiation Center, University of Wisconsin-Madison. A vacuum chamber with a 4-axis manipulator was used. The sample current was used to record the Total Electron Yield (TEY) spectra while the Fluorescence Yield (FLY) spectra were recorded using a channel plate detector. The experiments used the same experimental set up already described previously (Chapter 4, Figure 4.5).

5.5.3   Results and Discussion

Figure 5.13 shows the Ni $L_{3,2}$-edge XANES recorded in TEY for the Ni-Si lines, the four blanket films and Ni foil. As mentioned above, the XANES for the as-deposited and low temperature annealed films appear essentially the same as the XANES of Ni foil.
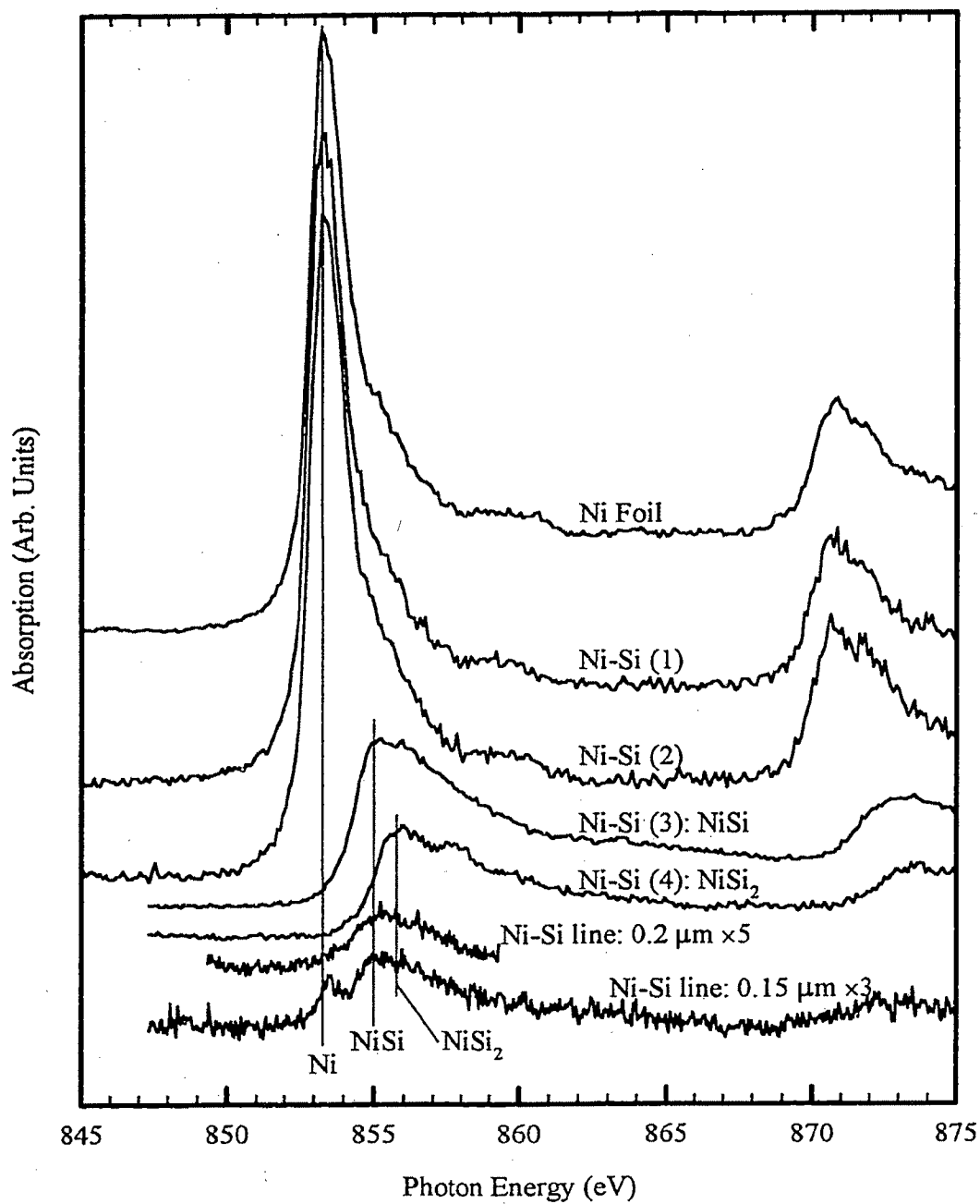
Figure 5.13. Ni $L_{3,2}$-edge spectra of the Ni-Si films, Ni lines and Ni foil taken in TEY mode. The vertical lines indicate the positions of the Ni, NiSi and NiSi$_2$ peaks.

The other two films exhibit distinct features and threshold shifts and are associated with NiSi and $NiSi_2$ for the well characterized Ni-Si (3) and Ni-Si (4) films, respectively.

Now comparing the XANES spectra for the films to those for the lines we see that the XANES for the lines is similar to that of NiSi. There is an additional sharp shoulder at the low photon energy side of the XANES in the lines which is more noticeable for the 0.15 micron line. The vertical lines in Figure 5.13 mark the energy positions of the first resonance in Ni metal, NiSi and $NiSi_2$. It is not difficult from these markers and the general spectroscopic features to conclude that the lines are essentially NiSi as desired. The shoulder at lower photon energy has the characteristics of Ni metal and can be attributed to either a small amount of Ni or Ni-rich silicide present.

The fluorescence yield Ni $L_{3,2}$-edge XANES spectra for the same series of samples is shown in Figure 5.14. The XANES of the lines suffer from poor statistics due to low count rates. They appear the same as their TEY counterparts except for a noticeable reduction in the relative intensity of the sharp low energy shoulder. Since FLY has a greater sampling depth over TEY this decrease in intensity of the shoulder indicates that the Ni or Ni-rich silicide is located near the surface region of the lines.

A more detailed comparison of the lines with the standard NiSi film is given in Figure 5.15. It is interesting to note that the Ni peak is only clearly visible in the TEY XANES of the 0.15 μm line sample and is considerably weaker in the 0.2 μm line sample. This is a clear indication that under the same experimental conditions, the silicidation process still forms NiSi but more Ni remains at the surface as the line becomes thinner (from blanket film to 0.2 to 0.15 μm). It is not entirely clear why this is the case as Ni is always the limiting reagent in the reaction. One plausible explanation may be that there is a change in the diffusion behaviour as the line gets thinner. More work is needed to clarify the reasons behind this behaviour. It is conceivable, however, that a change in annealing conditions may allow complete NiSi formation.
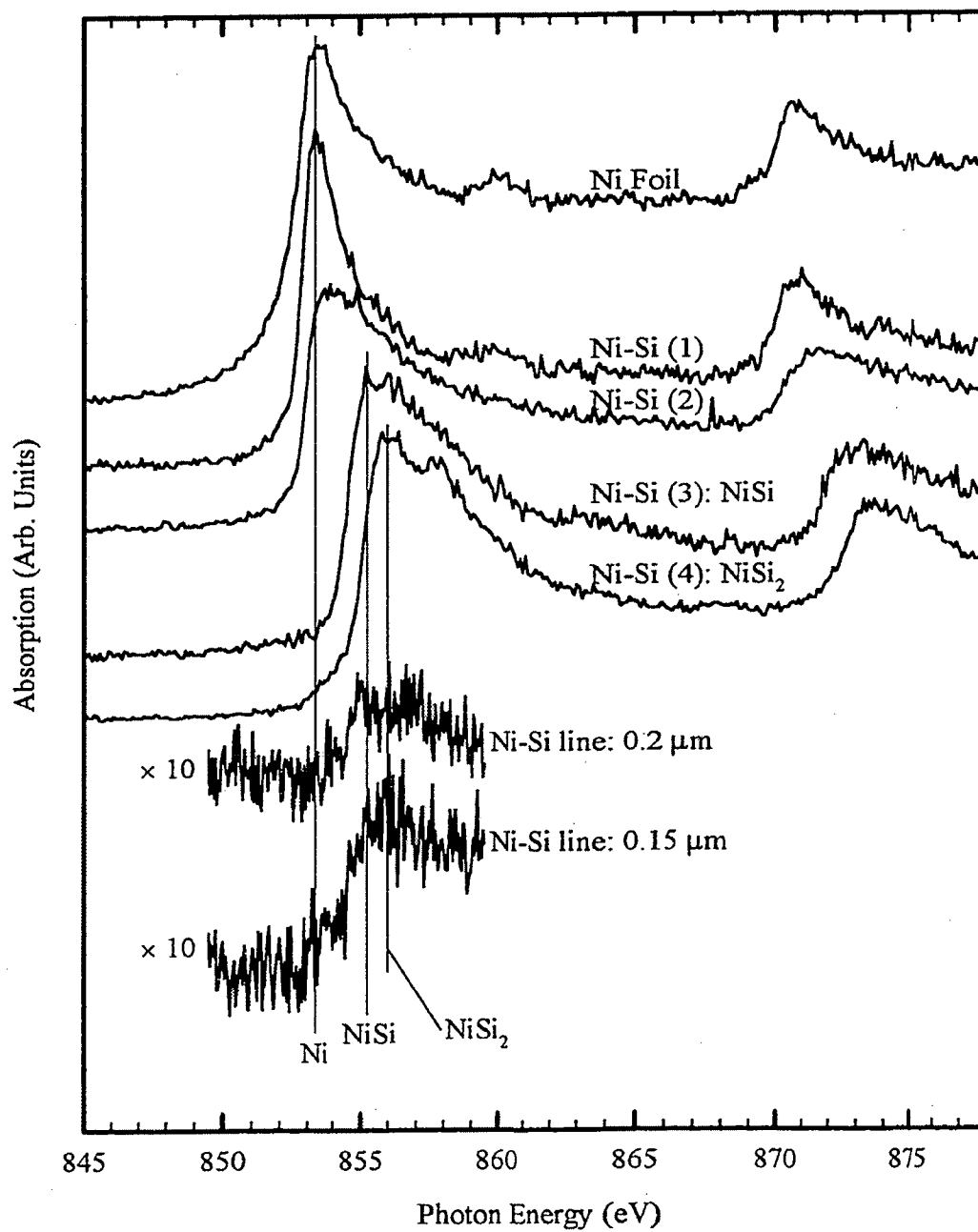
Figure 5.14. Ni $L_{3,2}$-edge spectra of the Ni-Si films, Ni lines and Ni foil taken in FLY mode. The vertical lines indicate the position of the Ni, NiSi and NiSi$_2$ peaks.
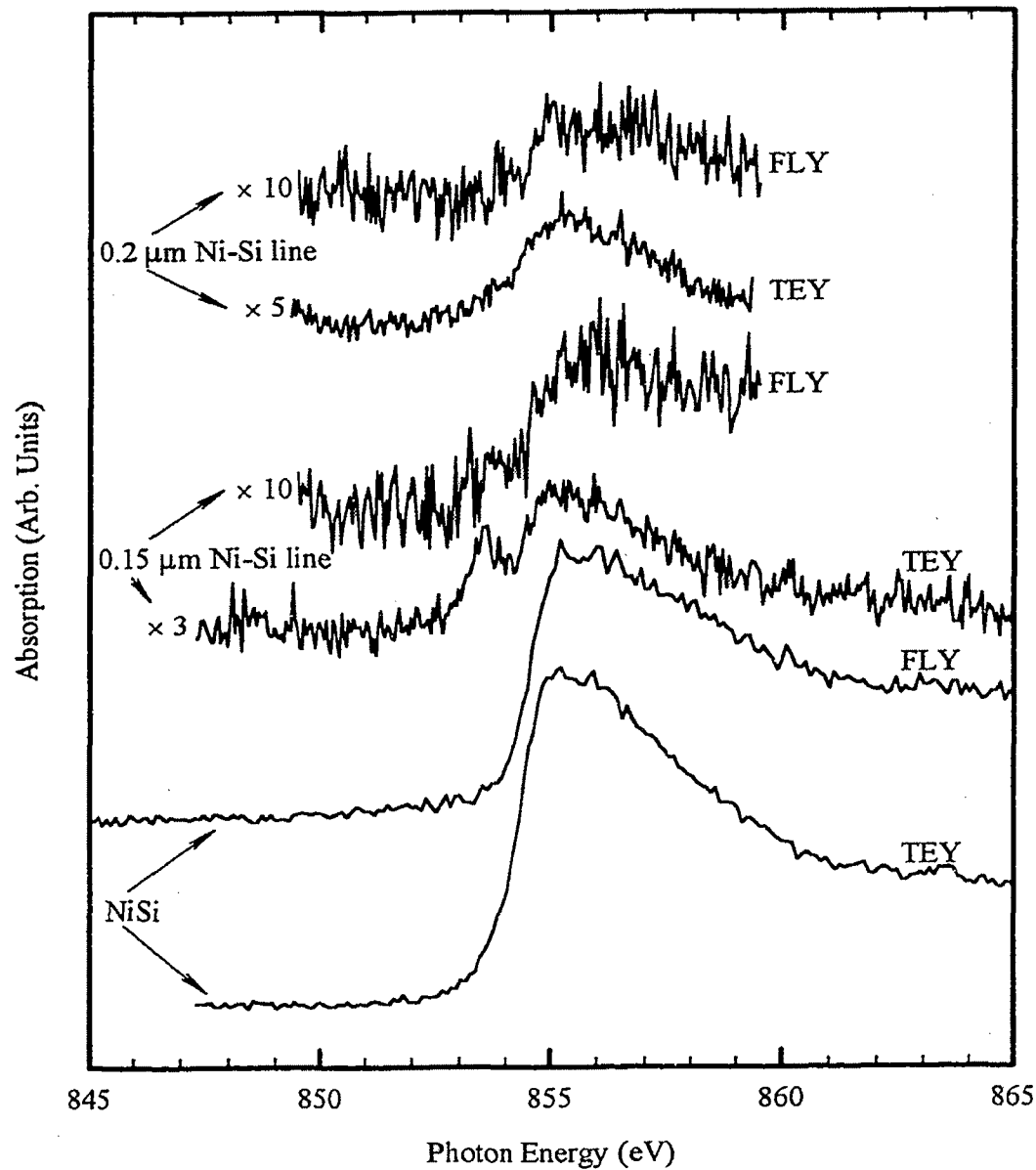
Figure 5.15. Ni L_3-edge XANES spectra of the Ni-Si lines compared to the spectra for NiSi in both TEY and FLY.

5.5.4   Conclusions

The short sampling depths of photons at the Ni $L_{3,2}$-edge allows for the sampling of the surface and bulk of the samples from the Ni perspective. This feature of X-ray absorption has proven valuable in the study of thin film and patterned structures. Comparison of the XANES for the Ni-Si lines and blanket films shows that although the desired NiSi was made in the lines under the reported experimental conditions, the conversion of Ni/Si system to a pure NiSi phase is affected by the line thickness with the conversion becoming less complete as the line becomes narrower.

The conclusion that "the conversion of Ni to NiSi is affected by the linewidth" is based only on two samples and is considered preliminary. A much larger series of samples is required to establish the general validity of this statement.

5.6   CALCULATIONS OF NICKEL SILICIDES

Many of the spectra discussed in the preceding section have distinctive structures like the Si L-edge which has not been theoretically investigated. Some distinctive spectral features were also found that may relate to compounds for which no standard was available. To investigate the origins of the spectral features and possibly help identify compounds, calculations of X-ray absorption spectra were carried out using the LAPW package WIEN97 [35].

The resulting DOS for $NiSi_2$, NiSi, and Ni_2Si are shown in Figure 5.16. The DOS shown are very similar to those calculated for the Co-Si system, this is expected as both sets of compounds have the same crystal structures and only differ by the addition of one more electron to the Co-Si systems. These results for $NiSi_2$ compare favourably with similar calculations found in the literature [19][22][23][36][37].

Using these DOS the X-ray absorption spectra were calculated for both the K and L edges of both Si and Ni. After the X-ray absorption spectra have been calculated from the DOS and the appropriate matrix elements, they are broadened by convolution with a
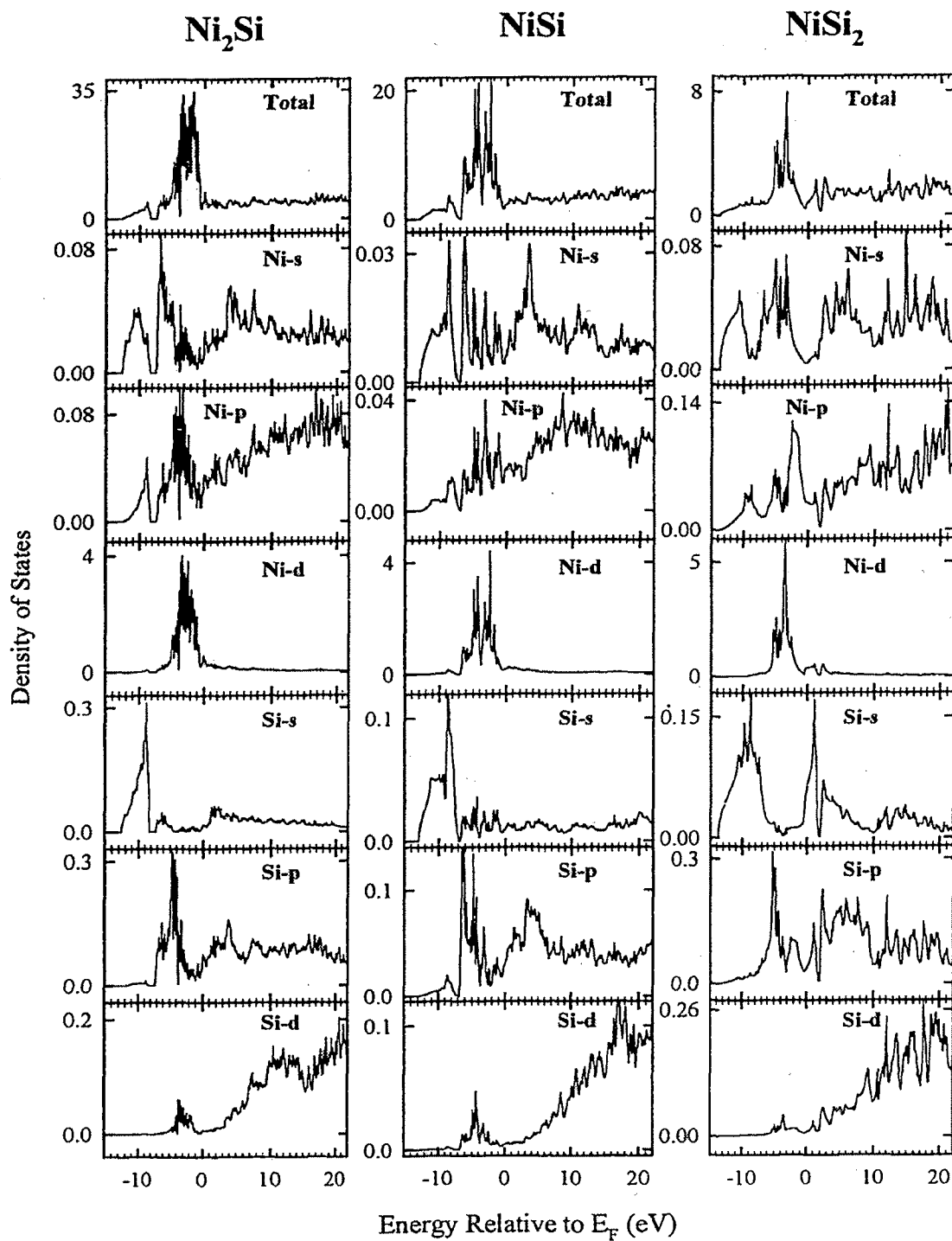
Figure 5.16. Calculated total and partial densities of states for Ni_2Si, $NiSi$ and $NiSi_2$.

Gaussian which represents the instrumental resolution. The width of this Gaussian was estimated (from approximate total spectral resolutions seen in the absorption data) as 0.15 eV, 0.8 eV, 0.6 eV and 1.67 eV for the Si L, Ni L, Si K and Ni K-edges respectively.

The results of the calculations for $NiSi_2$ are shown in Figure 5.17 along with the spectra from the films, which have been aligned to the point of inflection of the edge, and the unbroadened spectra. The calculations reproduce well those of previous workers [19][22][23][37]. The comparison with the experimental spectra show that the calculations reproduce the features of the spectra near the edge, although the intensity of the resonances is somewhat off, with increasing error farther from the edge. Some of these discrepancies were accounted for by Lerch *et al.* [23] by including the relaxation of the core hole in their calculations. Perhaps the most interesting edge is the Si $L_{3,2}$-edge which had intense sharp features. The agreement between the calculated spectra and the experiment is not as good as was seen for $CoSi_2$. The localized features of the unoccupied Si d- and s-DOS can still be clearly seen in the $NiSi_2$ calculated spectra. This is in contrast to the calculated and experimental Si L-edge spectra of NiSi (Figure 5.18) which lacks any intense peaks.

The results of the calculations are very good for the Ni L-edge where the splitting of the edge is clearly reproduced in the simulated spectrum of $NiSi_2$ but is absent in NiSi.
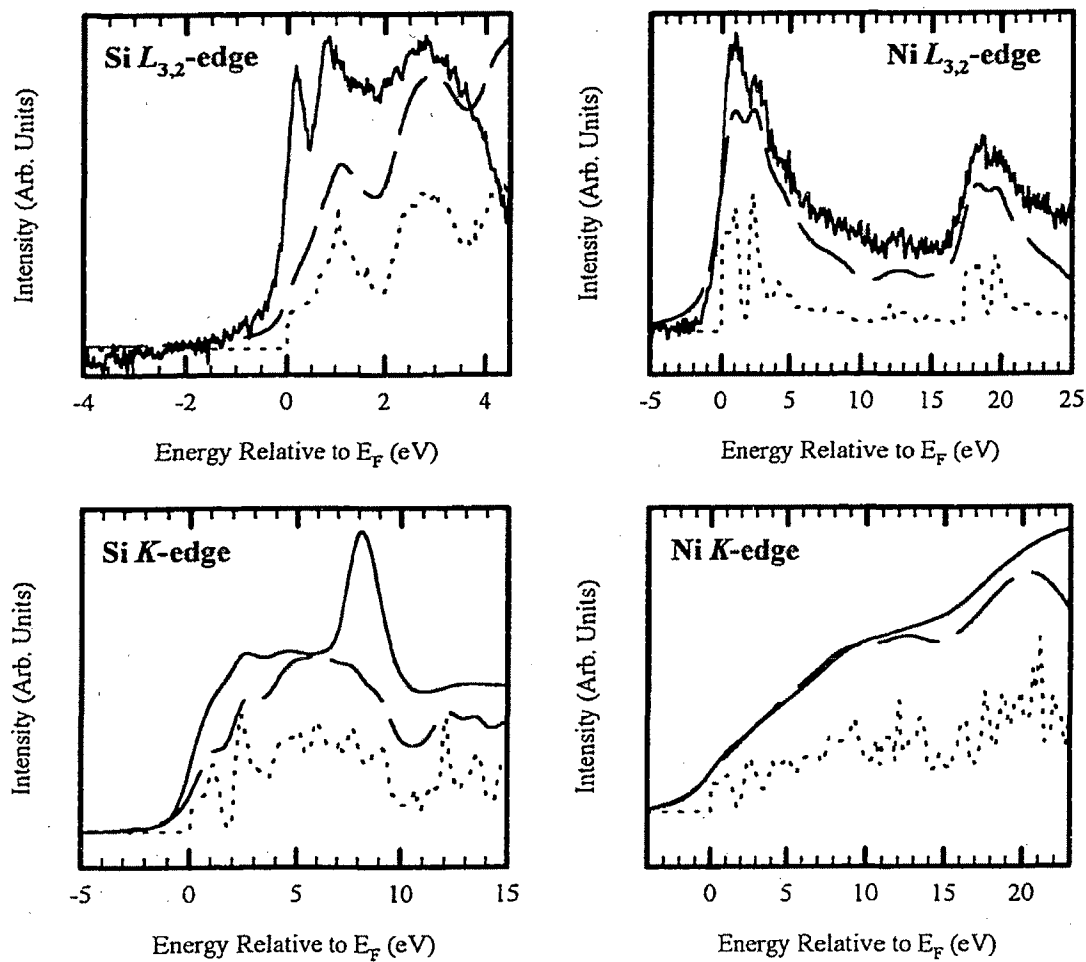
Figure 5.17. Comparisons of NiSi₂ data and calculations. (————) Data, (——— -) Calculated spectra and (- - - -) Unbroadened spectra.
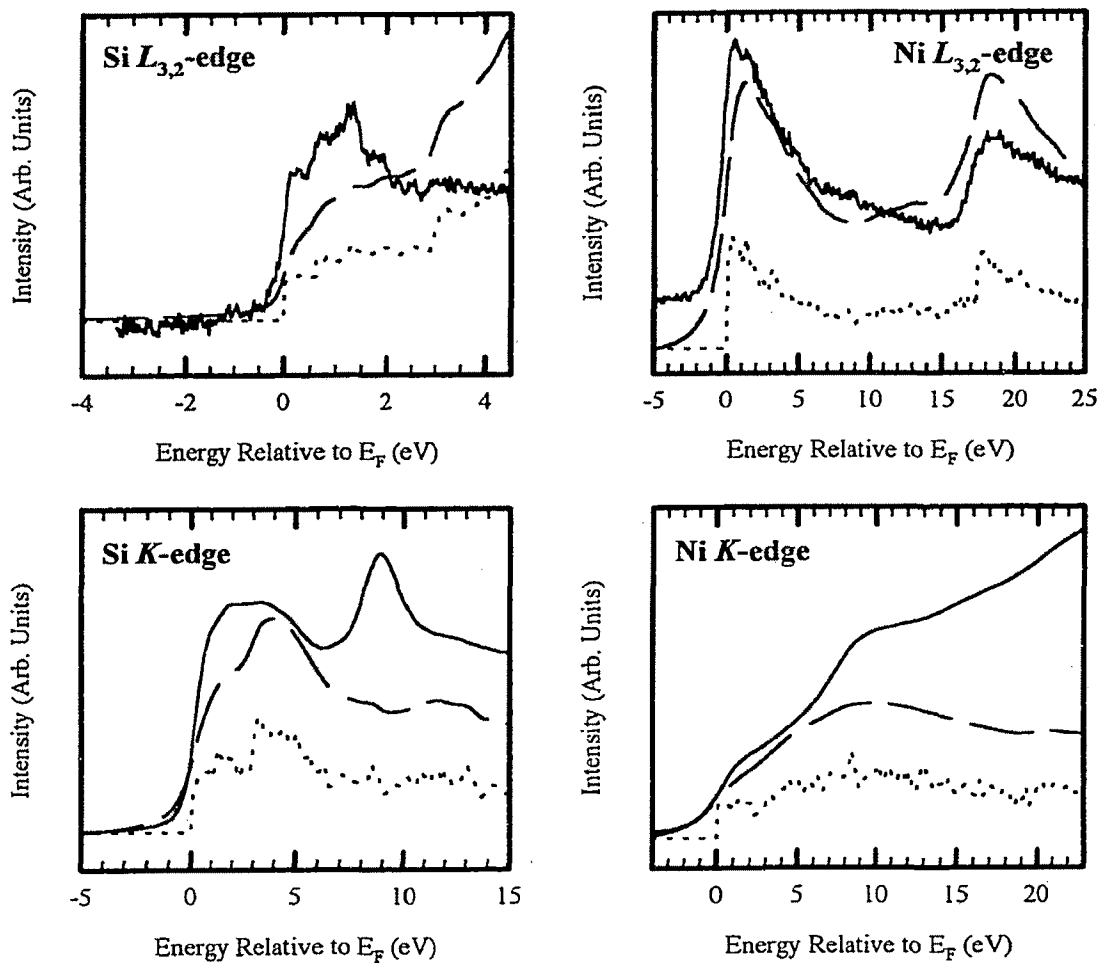
Figure 5.18. Comparisons of NiSi data and calculations. (———) Data, (——— -) Calculated spectra and (_ _ _ _) Unbroadened spectra.

5.7   REFERENCES

[1]   S. P .Murarka, *Silicides for VLSI Applications* (Academic Press, New York, 1983).

[2]   G. Ottaviani, J. Vac. Sci. Tech. **16**, 1112 (1979).

[3]   H. von Känel, Mater. Sci. Rep. **8**, 193 (1992).

[4]   S. Mantl, Mater. Sci. Rep. **8**, 1 (1992).

[5]   V. E. Burisenko and P. J. Hesketh, *Rapid Thermal Processing of Semiconductors* (Plenum Press, New York, 1997), Ch. 5.

[6]   J. Chen, J.-P. Colinge, D. Flandre, R. Gillon, J. P. Raskin and D. Vanhoenacker, J. Electrochem. Soc. **144**, 2437 (1997).

[7]   J. P. Gambino and E. G. Colgan, Mater. Chem. and Phys. **52**, 99 (1998).

[8]   E. G. Colgan, J. P. Gambino and Q. Z. Hong, Mater. Sci. Eng. **R16**, 43 (1996).

[9]   C. M. Osburn, Q. F. Wang, M. Kellam, C. Canovai, P. L. Smith, G. E. McGuire, Z. G. Xiao and G. A. Rozgonyi, Appl. Surf. Sci. **53**, 291 (1991).

[10]   K. Maex, Mater. Sci. Eng. **R11**, 53 (1993).

[11]   T. Ohguro, S. Nakamura, M. Koike, T. Morimoto, A. Nishiyama, Y. Ushiku, T. Yoshitomi, M. Ono, M. Saito and H. Iwai, IEEE Trans. Elec. Dev. **41**, 2305 (1994).

[12]   F. Deng, R. A. Johnson, P. M. Asbeck, S. S. Lau, W. B. Dubbelday, T. Hsiao and J. Woo, J. Appl. Phys. **81**, 8047 (1997).

[13]   D.-X. Xu, S. R. Das, L. Erickson and A. Naem, MRS Symp. Proc. **391**, 233 (1995).

[14]   S. R. Das, D.-X. Xu, J. Phillips, J. McCaffrey, L. LeBrum and A. Naem, MRS Symp. Proc. **318**, 129 (1994).

[15]   D.-X. Xu, S. R. Das, C. J. Peters and L. E. Erickson, Thin Solid Films **326**, 143 (1998).

[16]   *Binary Alloy Phase Diagrams*, eds. T. B. Massalski, J. L. Murray, L. H. Bennett and H. Baker (American Society for Metals, Metals Park, 1986), pg. 1756.

[17]   N. Cho and Y. Choi, J. Korean Phys. Soc. (Proc. Suppl.) **30**, S288 (1997).

[18]   U. Gottlieb, F. Nava, M. Affronte, O. Laborde and R. Madar, in *Properties of Metal Silicides*, eds. K. Maex and M. Van Rossum (Inspec, London, 1995), p. 189.

[19]   P. J. W. Weijs, M. T. Czyżyk, J. F. van Acker, W. Speier, J. B. Goedkoop, H. van Leuken, H. J. M. Hendrix, R. A. de Groot, G. van der Laan, K. H. J. Buschow, G. Wiech and J. C. Fuggle, Phys. Rev. B **41**, 11899 (1990).

[20]   U. del Pennino, C. Mariani, S. Valeri, G. Ottaviani, M. G. Betti, S. Nannarone and M. De Crescenzi, Phys. Rev. B **34**, 2875 (1986).

[21]   M. G. Betti, U. del Pennino, C. Mariani, A. M. Fiorello, M. Pedio, S. Perugini, S. Nannarone and M. De Grescenzi, Physica Scripta **36**, 153 (1987).

[22]   M. Sancrotti, L. Duo, R. Cosso, S. D'Addato, S. Iacobucci, G. Panaccione, A. Ruocco, S. Nannarone, M. Surman, P. Unsworth and P. Weightman, Solid State Commun. **78**, 641 (1991).

[23]   P. Lerch, T. Jarlborg, V. Codazzi, G. Loupias and A. M. Flank, Phys. Rev. B **45**, 11481 (1992).

[24]   P. Villars and L. D. Calvert, eds., *Pearson's Handbook of Crystallographic Data for Intermetallic Phases*, 2nd ed. (ASM International, Materials Park, OH, 1991).

[25]   W. T. Elam, J. P. Kirkland, R. A. Neiser and P. D. Wolf, Phys. Rev. B **38**, 26 (1988).

[26]   For a general review of photon detectors see: J. A. R. Samson, *Techniques of Vacuum Ultraviolet Spectroscopy* (Wiley, New York, 1967).

[27]   R. A. Rosenberg, J. K. Simons, S. P. Frigo, K. Tan and J. M. Chen, Rev. Sci. Instrum. **63**, 2193 (1992).

[28]   M. Kasrai, Z. Yin, G. M. Bancroft and K. H. Tan, J. Vac. Sci. Tech. A **11**, 2694 (1993).

[29]   R. E. Watson, J. Hudis and M. L. Perlman, Phys. Rev. B **4**, 4139 (1971).

[30]   A. Bzowski and T. K. Sham, J. Vac. Sci. Tech. A **11**, 2153 (1993).

[31]   P. W. Atkins, *Molecular Quantum Mechanics*, 2nd ed. (Oxford University Press, Oxford, 1983), p. 198.

[32] S. Eisebitt, T. Böske, J.-E. Rubensson and W. Eberhardt, Phys. Rev. B **47**, 14103 (1993).

[33] D. M. Pease, D. L. Brewe, Z. Tan, J. I. Budnick and C. C. Law, Phys. Lett. A **138**, 230 (1989).

[34] T. K. Sham, X.-H. Feng, D. T. Jiang, B. X. Yang, J. Z. Xiong, A. Bzowski, D. C. Houghton, B. Bryskiewicz and E. Wang, Can. J. Phys. **70**, 813 (1992).

[35] P. Blaha, K. Schwarz and J. Luitz, **WIEN97**, Vienna University of Technology 1997. (Improved and updated Unix version of the original copyrighted WEIN-code, which was published by P. Blaha, K. Schwarz, P. Sorantin and S. B. Trickey, Comput. Phys. Commun. **59**, 399 (1990)).

[36] O. Bisi and C. Calandra, J. Phys. C: Solid State Phys. **14**, 5479 (1981).

[37] A. Gheorghiu, C. Sénémaud, E. Belin-Ferré, Z. Dankhàzi, L. Magaud-Martinage and D. A. Papaconstantopoulos, J. Phys.: Condens. Matter **8**, 719 (1996).

CHAPTER 6: SUMMARY

Research into the properties of metal silicides is motivated mainly by the requirements of the semiconductor devices industry. The overriding drive of the industry continues to be the miniaturisation of devices. As device size continues to decrease, new demands are placed on the materials involved. As a result of the new demands, the focus of research has shifted from the macroscopic electrical and metallurgical properties of thick silicide films to the understanding of the microscopic behaviour of the interfaces present in structures formed with restricted dimensions. Current research into technically relevant metal silicides not only contributes to the technological advance in the semiconductor industry but also provides insight into fundamental challenges in the study of interface formation. In the future, the ability to control interfacial reactions and hence the macroscopic properties of interfaces will be a necessity to construct nanoscale devices.

This thesis presented three short investigations of the interactions of the transition metals with Si(100) substrates with the emphasis on characterizing the electronic and physical structure of the interfaces.

The first project utilized the bottom-up approach, to investigate the initial stages of the interaction of Au with Si(100) at room temperature. High resolution core-level photoemission spectroscopy, at the Si 2p and Au 4f core-levels, using synchrotron radiation was used to probe the surface layers of the interface as successively larger amounts of Au were deposited on the surface.

It was found that the Au/Si interaction is immediate, with a decrease in clean Si surface state intensity and an accompanying increase in intensity of a Au-Si phase (Au-Si A). As the Au coverage increases, the binding energy of the Au-Si phase photoemission

was found to shift relative to that of the bulk Si. This represents a (Au-Si A) → (Au-Si B) phase transition. At the same time, the Si bulk state is shifted towards the Fermi level by band bending effects. The second silicide formed persists as the Au coverage increases up to very thick gold layers. Analysis of the Au 4f photoemission spectra as a function of Au coverage indicates that a Au layer forms between the top silicide and the interface.

The picture of the interface formation described above is similar to that seen previously for the Si(111) and Si(100) surfaces; however, the immediate reaction and presence of a low coverage Au-Si peak with a different chemical shift from the final Au-Si peak has not been reported before. The chemical shifts of the Au 4f and Si 2p core levels for the high coverage silicide (Au-Si B) indicate that the charge transfer in the silicide follows the charge compensation model for Au bimetallics, in which a gain of sp-type charge on the Au site is compensated for by a loss of d-charge such that a only small net charge flow onto the Au site occurs, consistent with electronegativity and electroneutrality considerations.

There are several questions which remain about the formation of the Au/Si(100) interface, namely:

1) Whether the development of the band bending is abrupt or gradual. Along with this is the question of when the surface changes from semiconducting to metallic and the progress of the development of the Schottky barrier.

2) Whether "Au-Si A" and "Au-Si B" are alloys or stoichiometric compounds.

3) Whether the first Au silicide remains at the Au-Si interface, the second Au silicide remains at the interface or if the interface becomes atomically abrupt as the Au layer forms between it and the top silicide.

4) The exact positions of the atoms at the interface and composition of the first Au silicide formed up to a few ML.

5) Whether the discrepancies with previous Au/Si(100) core-level data is due to differences in surface preparation, Au dosing rates or other factors.

These questions can only be resolved by following the reaction with many more steps than were used. Applying complementary techniques, such as XANES, that can

examine the buried interface when the thickness of deposited gold exceeds the sampling depth of photoemission could help answer the structure of the Au/Si interface.

In the second project we undertook the first X-ray absorption study of thin film silicides prepared under various conditions utilizing the inherent sampling depths at each edge to elucidate the structure of the formed interface. Together with other investigations (Ni-Si, Pt-Si, Al-TiN) this study was aimed at assessing the feasibility of using soft X-ray XANES to characterize thin films industrially, either in a research setting or as a quality control tool.

We obtained (X-ray absorption near-edge structures) XANES from thin films of Co-Si at the Si $L_{3,2}$-edge, Si K-edge, Co $L_{3,2}$-edge and Co K-edge using both Total Electron Yield (TEY) detection and Fluorescence Yield (FLY) detection. The range of edges and sampling techniques provided a range of sampling depths form ~ 5nm to > 10 μm.

The samples obtained were made under slightly different preparation conditions but were expected to give a basic $CoSi_2$ film. For the unannealed film it was found that the surface of the deposited Co film was oxidized in the ambient and that some reaction occurred at the Co-Si interface even without annealing.

For the annealed films of $CoSi_2$ we found:

1) The films were capped with SiO_2 layers, less than 5 nm thick but the thickness varied with the preparation conditions.

2) Under the oxide cap, or interspersed at the surface, there were deposits of Co metal. The thickness again varied with the preparation conditions. The exact origin of the metallic Co could not be determined from this study but is thought to be related to the oxidative decomposition of the surface silicide to give Co and SiO_2.

The exact morphology of the surface oxide/ metallic cobalt layers could not be determined from the XANES data, however future photoemission results could resolve this question.

We have proven the utility of X-ray absorption spectroscopy for the study of thin films especially in the soft X-ray region. Having established the technique, a more detailed

study of the formation of metal films and lines dealing with formation times, temperatures, initial thicknesses and chemical sensitivity would be useful to generate a complete picture of the development of the silicides. Coupling the top-down approach (XANES) and bottom-up approaches (PES) will solve some of the remaining questions and represents an important future direction for the project.

One of the main motivations of the project was to investigate the effects of decreasing dimensions on the formation of silicide thin films. In order to investigate this we moved next to study the Ni-Si system. We again looked at blanket films prepared under different conditions with X-ray absorption spectroscopy for the first time. The Si $L_{3,2}$-edge, Si K-edge, Ni $L_{3,2}$-edge and the Ni K-edge were again examined with both TEY and FLY detection modes.

The samples obtained were made under slightly different preparation conditions but were expected to yield Ni-Si films of various compositions. It was found that the films followed the expected sequence of phase formation upon heating and that well formed films of NiSi and $NiSi_2$ were formed after appropriate annealing to 500 °C and 850°C, respectively.

For the unannealed film it was found that a reaction occurred at the Ni-Si interface even without annealing. This reaction developed further on light annealing to 300 °C so that a Ni-rich silicide phase, probably Ni_2Si was seen to develop from the Ni-Si interface towards the surface of the film under a layer of unreacted Ni.

For the high temperature annealed films we found:

1) The films were capped with SiO_2 layers, less than 5 nm thick due to selective oxidation of the films in the ambient atmosphere.

2) The bulk of the film annealed to 500 °C was indeed NiSi.

3) The bulk of the film annealed to 850 °C was the expected $NiSi_2$ phase.

This study of the thin films provided us with fingerprint spectra for NiSi and $NiSi_2$ at the Ni K, Ni L, Si K, and Si L-edges. Using the catalogue of spectra obtained we moved on to the study of patterned Ni lines at the Ni L-edge.

The short sampling depths of photons at the Ni $L_{3,2}$-edge allows for the sampling

of the surface and bulk of the samples from the Ni perspective. This feature of X-ray absorption has proven valuable in the study of thin film and patterned structures. Comparison of the XANES for the Ni-Si lines studied and the blanket films shows that although the desired NiSi was made in the lines under the reported experimental conditions, the conversion of Ni/Si system to a pure NiSi phase appeared to be affected by the line thickness with the conversion becoming less complete as the silicide line width narrows.

In the future it would be interesting to compare the results of these studies with similar results from studies of the Ti silicides, the other commonly used transition metal silicide in the semiconductor industry. Multi-core multi-detection XANES has proven to be a useful tool for the study of thin films and buried interfaces, coupled with other techniques, such as PES, it can provide valuable information on the fundamental challenges of interfacial structure development, not only in the transition metal silicides but also in any thin film or buried layer structure such as TiN diffusion barriers, magnetic multi-layers etc..

APPENDIX: COPYRIGHT PERMISSIONS

DISCLAIMER

TO WHOM IT MAY CONCERN:

The **Transfer of Copyright** agreements of The International Union of Crystallography

[publisher of S. J. Naftel and T. K. Sham, J. Synchrotron Rad. 6, 526 (1999)]

and The American Physical Society

[publisher of S. J. Naftel, I. Coulthard, T. K. Sham, S. R. Das and D.-X. Xu, Phys. Rev. B 57, 9179 (1998)]

both contain the statement; "....the authors reserve the .... right to use all or part of this article in future works prepared by or on the behalf of the author" (or similar statement). As a result it was not necessary to seek permission from these publishers to use portions of the above mentioned works in this thesis.

AMERICAN
INSTITUTE
OFPHYSICS

Suite 1N01
2 Huntington Quadrangle
Melville, NY 11747-4502

Tel. 516-576-2268
Fax 516-576-2327

E-mail: rights@aip.org
http://www.aip.org

Rights and Permissions Office

161

VIA FAX: 519-661-3022

14 September 1999

Dr. Steven J. Naftel
Department of Chemistry
The University of Western Ontario
London, Ontario
CANADA N6A 5B7

Dear Dr. Naftel,

This is further to your request for permission to use material from American Institute of Physics publications.

Permission is hereby granted for one time reproduction -- as per the requirements indicated below-- of the following article:
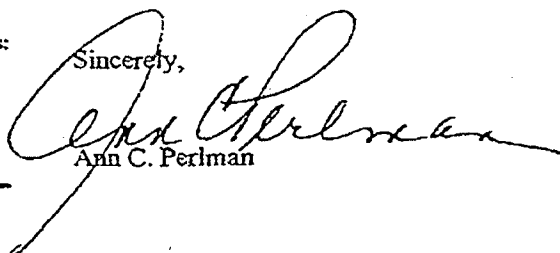
> Naftel et al, "Electronic structure of nickel silicide in subhalf-micron lines and blanket films: An x-ray absorption fine structures study at the Ni and Si $L_{3,2}$ edge", *Applied Physics Letters*, 74(19), May 10, 1999, pp 2893-2895

to be reproduced in your Ph.D. Thesis to be published by The University of Western Ontario. It is understood that the thesis will be microfilmed and single copies supplied upon demand.

[X] 1. The following credit line must appear in all copies (please fill in the information indicated by CAPITAL LETTERS): Reprinted with permission from FULL CITATION. Copyright YEAR, American Institute of Physics.

[X] 2. NOTE: This permission does not apply to figures, tables or other materials credited to sources other than the copyright holder.

[X] 3. Obtain the Author's permission to use the material. The author's address can be obtained from the article.

[ ] 4. An invoice for permissions fee (net 30 days) of $0 will follow. Please make check payable to American Institute of Physics. Please note: Permission is not valid until payment is received.

Thank you for requesting permission to use materials copyrighted by American Institute of Physics. Please do not hesitate to contact us should you have any further questions.

Sincerely,

Ann C. Perlman

7 September, 1999

Mr. Steven Naftel
Univ. of Western Ontario
Dept. of Chemistry

FAX#: 519/661-3022

Dear Mr. Naftel:

ASM International grants you non-exclusive world rights to reprint the following phase diagram figures for use in your PhD thesis, "Interactions of Transition Metals with Silicon (100): The Ni-Si, Co-Si and Au-Si (100) Systems :

Au-Si	Massalski, et al.	Vol 1, pg 313
Co-Si	"	Vol 1, pg 801
Ni-Si	"	Vol 2, pg 1756

Please be sure to credit ASM International.

Sincerely,

Cathy M. Neill

Cathy McNeill
Journals Administrative Assistant
cmcneill@po.asm-intl.org

6 September 1999

Steven Naftel
Dept of chemistry
University of Western Ontario
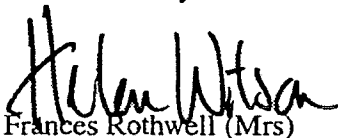London, Ontario N6A 5B7
Canada

Dear Dr Naftel

THIN SOLID FILMS, Vol 308-309, 1997, pp 580, Naftel: "Synchrotron Radiation Characterization..."

As per your email dated 19 August 1999, we hereby grant you permission to reprint the aforementioned material **in your thesis** at no charge subject to the following conditions:

1. If any part of the material to be used (for example, figures) has appeared in our publication with credit or acknowledgement to another source, permission must also be sought from that source. If such permission is not obtained then that material may not be included in your publication/copies.

2. Suitable acknowledgment to the source must be made as follows:

    "Reprinted from Journal title, Volume number, Author(s), Title of article, Pages No., Copyright (Year), with permission from Elsevier Science".

3. Reproduction of this material is confined to the purpose for which permission is hereby given.

4. This permission is granted for non-exclusive world **English** rights only. For other languages please reapply separately for each one required. Permission excludes use in an electronic form. Should you have a specific electronic project in mind please reapply for permission.

5. This includes permission for the National Library of Canada to supply single copies, on demand, of the complete thesis. Should your thesis be published commercially please reapply for permission.

Yours sincerely

Frances Rothwell (Mrs)
Subsidiary Rights Manager

The processing of permission requests for all Elsevier Science (including Pergamon imprint) journals has been centralised in Oxford, UK. Your future requests will be handled more quickly if you write directly to: Subsidiary Rights Department, Elsevier Science, PO Box 800, Oxford OX5 1DX, UK. Fax: 44-1865 853333; e-mail: permissions@elsevier.co.uk
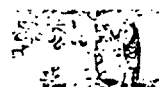
MRS Materials Research Society

PERMISSION REQUEST FORM

Date: AUG 19 / 99

Return to: STEVEN NAFTEL
(name)

UNIVERSITY OF WESTERN ONTARIO
(institution)

DEPARTMENT OF CHEMISTRY
(address)

LONDON, ONTARIO
CANADA   N6A 5B7

Phone #: (519) 679-2111 ext. 6297

Fax #: (519) 661-3022

Email: SNAFTEL@JULIAN.WO.CA

Source of Material:
CANADA   N6A 5B7

Source of Material:

(BOOK Title) APPLICATION OF SYNCHROTRON RADIATION TECHNIQUES TO MATERIALS SCIENCE IV

Material Requested for Use: ARTICLE " X-RAY ABSORPTION FINE STRUCTURE (XAFS)
(description of material, figure/table number, page numbers)
STUDIES OF COBALT SILICIDE THIN FILMS"   PAGE 273 - 277

(Authors) S.J. NAFTEL, I. COULTHARD, Y. HU, T.K. SHAM, M. ZINKE-ALLMANG.

Details for use: MATERIAL WILL BE INCLUDED AS PART OF PhD THESIS
(Will material be presented at a conference or published in a proceedings, text, or journal?)

" INTERACTIONS OF TRANSITION METALS WITH SILICON (100): THE Ni-Si, Co-Si,
AND Mn/Si (100) SYSTEMS" BY S.J. NAFTEL, SPECIFICALLY CHAPTER 4.

Distribution:
Is there a charge for the publication in which this material will be used? NO.
Is the publication being distributed free of charge? YES

Additional Comments:

Permission is granted provided you cite
the source and contact the author directly
Margie Pusateri   8-20-99.
Good Luck Steven!

VITA

NAME:	Steven James Naftel
PLACE OF BIRTH:	DesMoins, Iowa, USA
DATE OF BIRTH:	November 18, 1967
POST-SECONDARY EDUCATION AND DEGREES:	University of Western Ontario London, Ontario 1986-1991 Honours B.Sc. Chemistry
	University of Western Ontario London, Ontario 1991-1999 Ph.D.
HONOURS AND AWARDS:	Best Graduate Student Talk presented in the division of Physics and Theoretical Chemistry at CSC '97 June 1997
	Ontario Graduate Scholarship 1995-1996
	NSERC Postgraduate Award 1993-1995
	NSERC Undergraduate Student Research Awards 1989, 1990
	U. W. O. Entrance Scholarship 1986-1988
RELATED WORK EXPERIENCE:	Laboratory Demonstrator and Teaching Assistant University of Western Ontario 1991-1998

PUBLICATIONS

1. Z. Yuan, D. T. Jiang, S. J. Naftel, T. K. Sham and R. J. Puddephatt, "Dimethylpalladium(II) complexes as precursors for chemical vapor deposition of palladium.", Chem. Mater. **6**, 2151 (1994).

2. T. K. Sham, S. J. Naftel and I. Coulthard, "$M_{3,2}$-edge x-ray absorption near-edge structure spectroscopy: An alternative probe to the $L_{3,2}$-edge near-edge structure for the unoccupied densities of d states of $5d$ metals.", Journal of Applied Physics **79**, 7134 (1996).

3. T. K. Sham, S. J. Naftel, A. Bzowski, S. R. Das, D.-X. Xu, S. M. Heald, D. Brewe and M. Kuhn, "Synchrotron radiation studies of platinum silicide thin films.", Materials Research Society Symposium Proceedings **402**, 587 (1996).

4. S. J. Naftel, I. Coulthard, T. K. Sham, D.-X. Xu and S. R. Das, "Synchrotron radiation characterization of metal silicide thin films: Some observations.", Thin Solid Films **308-309**, 580 (1997).

5. S. J. Naftel, T. K. Sham, S. R. Das and D.-X. Xu, "Silicon $L_{2,3}$-edge XANES study of platinum silicide thin films.", Materials Research Society Symposium Proceedings **441**, 175 (1997).

6. T. K. Sham, I. Coulthard and S. J. Naftel, "$M_{3,2}$-edge X-ray absorption near-edge structure of 5d metals.", Journal De Physique IV France 7, C2-477 (1997).

7. S. J. Naftel, A. Bzowski, T. K. Sham, D.-X. Xu and S. R. Das, "XAFS studies of self-aligned platinum silicide thin films at the Pt $M_{3,2}$ edge and the Si K-edge.", Journal De Physique IV France 7, C2-1131 (1997).

8. S. J. Naftel, T. K. Sham, V. I. Smelyansky, J. S. Tse and J. D. Garrett, "Angular dependent XAFS studies of a $MoSi_2$ single crystal.", Journal De Physique IV France 7, C2-495 (1997).

9. S. J. Naftel, I. Coulthard, T. K. Sham, S. R. Das and D.-X. Xu, "Structural and electronic property evolution of nickel and nickel silicide thin films on Si(100) from multi-core X-ray absorption fine structures studies.", Physical Review B **57**, 9179 (1998).

10. H. H. Hsieh, Y. K. Chang, W. F. Pong, J. Y. Pieh, P. K. Tseng, T. K. Sham, I. Coulthard, S. J. Naftel, J. F. Lee, S. C. Chung and K. L. Tsang, "Electronic structure of Ni-Cu alloys: The d-electron charge distribution.", Physical Review B **57**, 15204 (1998).

11. I. Coulthard, S. J. Naftel and T. K. Sham, "Synchrotron X-ray absorption spectroscopy studies of Pt/Si systems.", Materials Research Society Symposium Proceedings **524**, 291 (1998).

12. S. J. Naftel, I. Coulthard, Y. Hu, T. K. Sham and M. Zinke-Allmang, "X-Ray absorption fine structure (XAFS) studies of cobalt silicide thin films.", Materials Research Society Symposium Proceedings **524**, 273 (1998).

13. S. J. Naftel, A. Bzowski and T. K. Sham, "A study of the electronic structure of Au-V bimetallics using X-ray photoelectron spectroscopy (XPS) and X-ray absorption near-edge structure (XANES).", Journal of Alloys and Compounds **283**, 5 (1999).

14. S. J. Naftel, I. Coulthard, T. K. Sham, D.-X. Xu, L. Erickson and S. R. Das, "Electronic structure of nickel silicide in sub-half-micron lines and blanket films: An X-ray absorption fine structures study at the Ni and Si $L_{3,2}$-edge.", Applied Physics Letters **74**, 2893 (1999).

15. S. J. Naftel and T. K. Sham, "Co $L_{3,2}$-edge and multi-detection channel XAFS studies of Co-Si interactions.", Journal of Synchrotron Radiation **6**, 526 (1999).